Nonlinear pseudospin dynamics of exciton-polaritons in a semiconductor microcavity

seit 1558

vorgelegt dem Rat der

Physikalisch-Astronomischen Fakultät
der Friedrich-Schiller-Universität Jena

von Dipl.-Phys. Friedemann Albrecht Werner

geboren am 02.06.1985 in Pirna

Gutachter

1. *Prof. Dr. Falk Lederer*
   Institut für Festkörpertheorie und theoretische Optik
   Friedrich-Schiller-Universität Jena

2. *Prof. Dr. Kęstutis Staliūnas*
   ICREA Research Professor
   Universitat Politècnica de Catalunya (UPC)

3. *Prof. Dr. Thorsten Ackemann*
   Department of Physics
   University of Strathclyde

Tag der Disputation: 24.02.2016

Contents

Contents

1. Introduction

The effects of light-matter interaction have been a topic of vigorous scientific interest at least since the observation of the absorption lines in the solar spectrum by Fraunhofer [1]. Since those days there has been tremendous progress in both optical technology and the growing techniques for the matter part of the interaction. Amongst other solid state optical systems, semiconductor microcavities occupy a prominent place. A semiconductor microcavity is realized by confining a solid state structure in an optical resonator. This setup is similar to the well-known vertical-cavity surface-emitting laser (VCSEL) [2]. The actual dynamics of these cavities depends crucially on the ratio between losses and the strength of the light-matter interaction. A semiconductor microcavity exhibits losses both from the photonic and the electronic component. The photonic losses originate from the imperfection and finite Q factor of the cavity. Besides the photonic loss channels, further losses arise due to the interaction of excitons with phonons and other imperfections of the semiconductor. As long as the light-matter interaction is overpowered by irreversible processes originating from the loss mechanisms, the light-matter coupling is incoherent. The corresponding regime is called *weak-coupling regime*, cf. Ref. [3] for an introduction. An important function of the cavity is the enhancement of the photonic field. If the cavity mode can be shifted spectrally by more than the cavity linewidth, the coexistence of two stable states at the same intensity can be reached. This effect is called bistability [4]. Other typical effects studied for weakly coupled microcavities include dissipative solitons [5, 6] and spatially extended periodic patterns [7–11].

Advanced fabrication technologies allowed the improvement of both the purity of the semiconductor crystal and the Q factor of the microcavity. These improvements enabled the observation of the *strong-coupling regime* in semiconductor microcavities by Weisbuch *et al.* in 1992 [12]. Strong coupling was observed before between atoms and cavity photons, cf. Ref. [13] and citations therein. It is generally reached when the coupling strength between two oscillators exceeds the mean of their loss rates. In this case, the coupled quantum system develops two eigenstates. This splitting of the spectrum is called vacuum Rabi splitting. The main difference to the weak-coupling regime is given by the coherent light-matter interaction. Excitons and cavity photons form a new inseparable half-light, half-matter state which is called *exciton-polariton*. Its dispersion relation consists of two branches arising from the anticrossing of the respective dispersion relations. This unique shape yields the specific properties of these quasiparticles. Polaritons are not only of

theoretical interest, but also offer the possibility for various applications. Due to its photonic component, an exciton-polariton is 10^4 to 10^5 times lighter than an exciton. This makes exciton-polaritons promising candidates for the observation of Bose-Einstein condensation at high temperature [14–22] and superfluidity [23–30]. Effects such as pattern formation, solitons, and their polarization dynamics have also been of vigorous interest in the framework of polariton condensates [31–38]. Like in the weak-coupling regime, the nonlinearity allows for the formation of bistable homogeneous solutions [29, 39–43] and parametric effects [24, 43–47]. However, since the nonlinearity in the strong-coupling regime originates from the coherent exciton-exciton interaction, it is both stronger and faster than the nonlinearities typically achieved in the weak-coupling regime. Hence, a major advantage of the strong-coupling regime with regard to possible applications lies in the significant reduction of the pump intensity that is required to observe these effects. In Ref. [40], the threshold of the pump intensity for bistability is observed to be 100 W/cm^2, which is about two orders of magnitude smaller than the 10 kW/cm^2 required for semiconductor microcavities driven in the weak-coupling regime [48]. The typical time scales lie in the picosecond range compared to the nanosecond range of the weak-coupling regime.

1.1. Aim of this thesis

The strong and fast nonlinearity makes the exciton-polaritons a promising candidate for applications as all-optical information storage and processing devices [49–56] and paves the way to applications such as polaritonic lasing [57–60]. In order to reach this goal, one needs to establish a mechanism to address and manipulate the field configuration at certain sites in the transverse plane of the semiconductor microcavity. These locally nonuniform field configurations can then be interpreted as optical bits. More generally, a comprehensive understanding of the dynamics of the different spatially nonuniform solutions and their mutual relations is required. The most natural transition from spatially uniform solutions to nonuniform ones is given by the spontaneous formation of spatially periodic patterns due to modulation instability [7]. This way of pattern formation is a well-studied topic of nonlinear optics, e.g., in the case of nonlinear media with counter-propagating waves [61–64] or other passive and active nonlinear optical systems [65–71], especially cavities filled with a nonlinear medium [72–84]. Reviews on pattern formation in dynamic systems can be found in Refs. [7–11]. However, the strong correlation between different sites of an extended pattern makes them unsuitable for information processing purposes, since any local alteration of the field imprinted in order to encode information would either be damped out or influence the entire pattern. Nevertheless, studying spatially periodic

patterns paves the way to a better understanding of *spatial cavity solitons*, spatially localized solutions that do not interfere with each other and are therefore individually addressable. Cavity solitons have been described before in the weak-coupling regime [48, 55, 56, 85–99]. The concepts presented there can easily be transferred to polariton solitons, for a review cf. Ref. [100]. Due to their spatial confinement many solitons can be written and erased on the transverse plane of the microcavity by shining localized address pulses at the respective sites. The resulting change of the polariton density persists, since its diffractive spreading is compensated by nonlinear effects [85–87, 99]. Dissipation due to the losses is compensated by constantly pumping the system. This work includes a comprehensive study of various aspects of pattern formation. The properties of spatial solitons are primarily studied using the example of dark solitons.

Besides this practical goal, another scope of the current work is also extending the understanding of the polariton nature. For that purpose, further effects such as the formation of domain walls between different spatially homogeneous solutions shall be studied. By emphasizing the links between all studied effects and their universality, these findings can be transferred to other strongly coupled systems and systems with light-matter interaction in general, such as the strong coupling of single photons to a qubit [101] or the strong coupling of nanoantennas with atomic systems [102]. Furthermore, it is worthwhile to take into account the internal structure of the exciton-polariton mediated by the exciton spin and its interplay with the properties of the cavity, namely the splitting between longitudinal and transverse polarized cavity modes (TE-TM splitting). The hybrid half-light half-matter nature of exciton-polaritons reveals the necessity to treat them as real quantum systems: On the one hand, excitons are spatially confined in the quantum well. This property will emerge whenever the pump frequency is near the excitonic resonance. On the other hand, the wave function of the cavity photon is extended over the whole cavity.

Pumping mechanisms for the creation of exciton-polaritons include electrical pumping, incoherent optical pumping, and coherent optical pumping. Throughout this work, the latter mechanism will be used exclusively. The pump frequency is chosen such that its detuning from the excitonic resonance corresponds to the lower polariton branch. Special emphasis will be on effects arising from the exciton spin which is inseparably linked with the polarization state of the cavity photons. Pumping in the vicinity of the parabola-like bottom of the lower polariton branch leads to effects which have been described in the framework of Kerr cavities exhibiting a perfect parabolic dispersion relation. However, by choosing a frequency far from the bottom of the lower polariton branch, the dispersion relation can no longer be approximated by a parabola and thus exciton-polaritons show a much richer variety of effects. Furthermore, the combination of spin and polarization

effects as it is available for exciton-polaritons, has no analogon in the Kerr cavity and thus the related effects are also unique for the polaritonic cavity.

1.2. Structure of the thesis

This thesis is basically divided into two main parts. The first part is of introductory nature. It covers the derivation of the basic equations of motion and contains Chapts. 2 and 3. In Chapt. 2, the idea of exciton-polaritons arising from strong coupling of excitons and photons is introduced, whereas all effects arising from the exciton spin and the polarization of the cavity photons are outsourced to Chapt. 3. The respective equations of motion are derived via an elegant Hamiltonian approach using the language of quantum field theory.

Chapter 4 gives an overview over all solutions of the equations of motion and discusses the used analytical and numerical methods. The different solutions will then be discussed in the second part of the thesis which consists of Chapts. 5-8. This part comprises the results of our research.

Chapter 5 contains an analytical study of all spatially uniform solutions. A section is devoted to the linear polariton dispersion relation disregarding effects originating from the pump and the nonlinearity. These findings are extended in two ways: on the one hand by including the TE-TM splitting of the dispersion relation and on the other hand by finding an analytical expression which estimates its nonlinear blueshift. Subsequently the bistability conditions for solutions of the full spinless equations of motion will be discussed as well as the bifurcation of solutions originating from the exciton spin. An important prerequisite for the spontaneous formation of periodic patterns is realized by investigating the destabilization of the homogeneous solutions in favor of spatially periodic perturbations (modulation instability).

A comprehensive study of pattern formation is given in Chapt. 6. In the spinless case the influence of the detunings and the pump power on the shape of the arising patterns is studied. Effects arising from the exciton spin and the TE-TM splitting of the cavity modes comprise the spontaneous formation of elliptically polarized patterns and their spontaneous uniform movement, respectively.

One- and two-dimensional spatial solitons are covered in Chapt. 7. The emphasis is put on dark solitons nesting on the upper branch of the bistability loop. Pseudospin effects lead to the formation of vectorial solitons.

Chapter 8 is linked to the preceding chapter and covers another type of localized solutions, namely one-dimensional domain walls between different homogeneous solutions.

2. Strong Coupling

Ever since Einstein's description of the photoelectric effect [103], the physics of optical light sources has been intrinsically tied to atomic physics and later also to solid state physics. This alliance became even stronger with the advent of nonlinear optics [104, 105] after the invention of the laser [106, 107].

In the textbook examples for nonlinear optical systems [108, 109], the nonlinearity is usually introduced via a quantum mechanical derivation of the nonlinear susceptibilities. This treatment is appropriate for the description of the nonlinear properties of off-resonant systems, such as atomic vapors, since they consist of free atoms whose atomic parameters are known with high accuracy. A prototypical example for the equation of motion for such a system is the Nonlinear Schrödinger equation. It is suitable for the description of optical systems whose dynamics is dominated by a third-order nonlinearity, e.g., propagation of light in nonlinear optical fibers [109]. A natural generalization of this model was presented by Lugiato and Lefever [72] considering a coherently driven system with Kerr nonlinearity and losses. This Lugiato-Lefever model will be used as a starting point for the discussion of polariton pattern formation in Sec. 6.1.

However, these rather simple models are generally not suitable for the proper description of the resonant interaction between light and semiconductors excitations. In this case, the nonlinearity itself depends crucially on the properties of the irradiating photon field such as intensity, frequency, polarization state, and cavity parameters. Thus, it is necessary to find a self-consistent solution of the resulting coupled system of equations.

Semiconductor microcavities, as depicted in Fig. 2.1, display a realization of the aforementioned coupling between cavity photons and elementary excitations of a semiconductor, namely excitons. Depending on the ratio between the exciton-photon coupling and the influence of the loss channels, one can distinguish between two different coupling regimes between excitons and photons: weak coupling and strong coupling. Both interaction regimes are studied in Sec. 2.1. The successive section 2.2 is devoted to the derivation of the equations of motion of exciton-polaritons, new quasiparticles arising from the strong coupling of excitons and cavity photons in a coherently driven semiconductor microcavity. These equations will be the starting point for all subsequent investigations.

2.1. Optics in a semiconductor microcavity
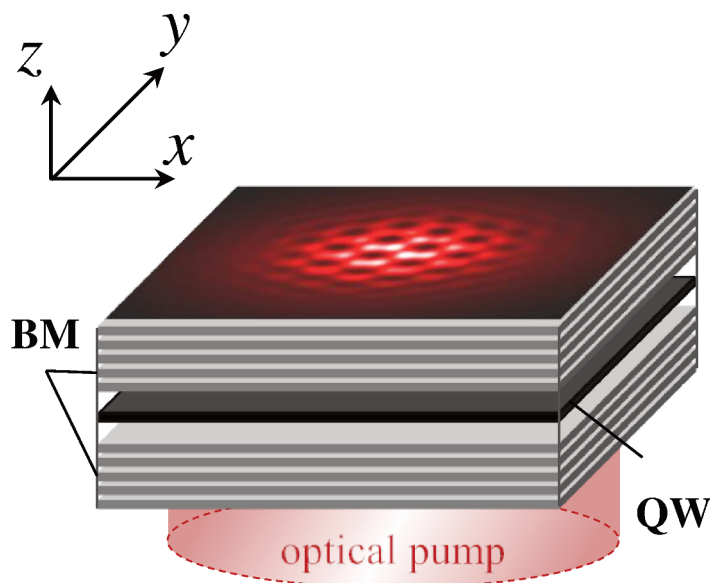
Figure 2.1: Schematic sketch of a semiconductor microcavity: a semiconductor quantum well (QW) is sandwiched between two Bragg mirrors (BMs); the configuration is pumped from below with a wide optical beam; the output field $E(x, y)$ can be observed in the transverse plane represented by the upper BM.

The interaction between photons and elementary excitations of a semiconductor can be enhanced by placing the semiconductor in a resonant cavity. This section contains an overview of both the optical properties of the microcavity and the formation of excitons in a quantum well. After having examined these two constituents separately, the different interaction regimes are studied, when the semiconductor quantum well is brought into the microcavity. The ratio between the losses and the strength of the exciton-photon interaction turns out to be crucial to distinguish between weak- and strong-coupling regime.

2.1.1. Fabry-Pérot microcavities

A microcavity is an optical resonator close to the dimension of the wavelength of light. It is used to confine light. Depending on the mechanism that is used to trap the photons, one can realize, e.g., planar microcavities, spherical mirror microcavities, whispering-gallery microcavities, photonic crystal microcavities, and plasmonic microcavities [3]. We will restrict ourselves to microcavities consisting of two planar multilayer Bragg mirrors (BMs), cf. Fig. 2.1. This setup is usually referred to as Fabry-Pérot resonator[a].

---

[a]Actually, from a purely mathematical point of view, the governing equations of motion of a ring cavity, a Fabry-Pérot cavity, and of a system consisting of two counterpropagating laser beams are identical, cf.

A Fabry-Pérot cavity can be characterized by the cavity length L_c and the reflection coefficient r of the dielectric BM. In contrast to conventional resonators, microcavities are characterized by a comparably small length L_c, typically $0.2 - 0.4\,\mu\mathrm{m}$. Therefore the spacing between the frequencies of the eigenmodes is so large that each stop-band usually contains exactly one cavity mode. Since the reflectivity is less than unity [110], the cavity transmits light with a characteristic spectrum. These transmission peaks are broadened because the light can tunnel through the Bragg mirrors even in their stop-bands representing the main loss channel of the resonator. A measure for this process to happen is given by the quality factor Q of the cavity. It can be defined by the ratio of the electromagnetic energy $U(t)$ stored in the cavity to the energy dissipated per cycle via tunneling of light through the mirrors [3, 13, 110–113]:

$$Q = \Re\widetilde{\omega}_c \frac{U}{dU/dt}. \tag{2.1}$$

Here, $\Re\widetilde{\omega}_c$ denotes frequency of the resonant cavity mode. Solving the differential equation (2.1) yields an exponential decay of $U(t)$ with lifetime

$$\tau = \frac{Q}{\Re\widetilde{\omega}_c}. \tag{2.2}$$

The respective transmission spectrum has a pole at the complex frequency $\omega = \Re\widetilde{\omega}_c + i\Re\widetilde{\omega}_c/2Q$. For $\omega = \widetilde{\omega}_c = \Re\widetilde{\omega}_c + i\Im\widetilde{\omega}_c$, the comparison of the imaginary parts yields a quality factor of

$$Q = \frac{\Re\widetilde{\omega}_c}{2\Im\widetilde{\omega}_c}. \tag{2.3}$$

Equations (2.2) and (2.3) yield a lifetime of

$$\tau = \frac{1}{2\Im\widetilde{\omega}_c}. \tag{2.4}$$

It is a measure for the average storage period of a photon inside the microcavity. The real part of $\widetilde{\omega}_c$ matches the conventional definition of the eigenfrequency of the cavity. Its natural denotation is ω_c. However, it shall be noted that its imaginary part

$$\gamma_c := \Im\widetilde{\omega}_c \tag{2.5}$$

defines a photon decay rate. The splitting between TE- and TM polarized cavity modes was omitted here and will be discussed later in Sec. 3.2.

---

the special issue of *Chaos, Solitons & Fractals* on transverse nonlinear optics introduced by Ref. [74].

2.1.2. Excitons in a semiconductor quantum well

The photoemission lines of excitons were first observed in the spectrum of cooled benzene in the 1920s by Kronenberger and Pringsheim [114]. The origin of these lines was interpreted by Frenkel as stemming from excitation waves in the crystal [115] which he later termed excitons [116]. An exciton is a bound state of an electron and a hole tied together by their mutual Coulomb force. One usually distinguishes between two main types: Frenkel excitons and Wannier-Mott excitons. Frenkel excitons arise from the strong Coulomb interaction between both constituents which usually exists in materials with a small dielectric constant such as organic molecular crystals. Thus, they are subjected to a distinct spatial confinement and their binding energy is typically in the range of $100 - 300$ meV. Wannier-Mott excitons [117, 118] are typical for semiconductors which naturally have a much higher dielectric constant. Their size can reach more than ten lattice constants and their binding energy is much smaller lying in the range of a few meV. There are also hybrid forms of Frenkel-Wannier-Mott excitons combining the huge binding energy with relatively large size. They can arise in mixed organic-anorganic structures [119].

However, since the excitons in the semiconductor considered here are of pure Wannier-Mott type, we will limit all following considerations to this case. The effective mass approximation allows to describe them as quasi-free particles with parabolic dispersion relation, where the influence of the periodic crystal potential is encoded in the effective mass. These effective masses are usually much smaller than the mass m_0 of the free electron in vacuum. In, e.g., GaAs, the effective electron mass amounts $m_e = 0.067m_0$ and the effective mass of the heavy hole is $m_{hh} = 0.45m_0$. Forming an exciton out of an electron and a heavy hole is energetically preferable compared to an exciton formed out of an electron and a light hole. The Coulomb interaction between electron and hole allows to treat the exciton like a hydrogen atom with reduced mass $\mu = m_e m_{hh}/(m_e + m_{hh})$ and renormalized charge $e^2 \to e^2/\epsilon$, where ϵ is the dielectric constant of the semiconductor [3, 120]. The binding energy is then approximately three orders of magnitude smaller than that of the hydrogen atom. In contrast to the hydrogen atom, the exciton has a finite lifetime in the nanosecond range [121]. However, as long as electron and hole are bound together, it is reasonable to treat them as a proper quasiparticle instead of regarding electron and hole separately. This approximation will be used in the following section to derive the equations of motion of the exciton.

It is well-known, that the density of states and the wave function of the excitons are influenced by the geometry and dimensionality of the semiconductor [3, 120, 122–124]. Due to their large size, especially Wannier-Mott excitons are subjected to confinement

effects. The binding energy of a perfect two-dimensional exciton in a quantum well is four times as strong as in the bulk material [122, 123]. The oscillator strength of the resonance is increased likewise. In a perfect one-dimensional system, solving the Schrödinger equation would even yield a ground state of infinite binding energy [124]. Since real structures are never purely one-dimensional, there are no such divergencies in a quantum wire. However, quantum well structures based on GaAs materials also exhibit strongly enhanced excitonic effects due to the dimensional reduction.

Unlike the hydrogen atom, the exciton has a finite lifetime. This displays a damping mechanism for the excitons. The time constant related to this population decay of the electron-hole pairs is called T_1. It is in the range of 1 ns. The other characteristic time scale T_2 is related to the damping due to dephasing processes of the exciton wave function. These dephasing processes occur due to growth inhomogeneities of the quantum well and also collisions of the exciton with phonons. Measurements of the exciton dephasing time [125, 126] yield a value of about 1 ps. The dephasing processes are thus about three orders of magnitude faster than the exciton lifetime. Analogously to the definition of the photon decay rate γ_c in Eq. (2.5), it is reasonable to define the exciton decay rate

$$\gamma_0 := \frac{1}{T_2}. \tag{2.6}$$

The existence of phonons is crucially depending on the temperature and the purity of the semiconductor. Phonons can be suppressed by cooling down the semiconductor and using suitable materials such as nitrides.

2.1.3. Semiclassical description of exciton-photon coupling

Excitons can most easily be created by optically exciting electrons and holes in a semiconductor. The response of the material to a weak external field is governed by the transition amplitude of an electron from the valence band to the conduction band. As stated before, the excitons that typically arise in a semiconductor are Wannier-Mott excitons. Thus, the linear optical properties of the semiconductor are governed by Coulomb interaction effects. The nonlinear optical properties of the semiconductor are influenced by the density of the excitons. As long as the exciton-photon interaction is overpowered by the dephasing, the absorption of photons and the subsequent formation of excitons merely causes the bleaching of the semiconductor. This eventually leads to a dependence of the nonlinear refraction coefficient on the exciton density. Thus the exciton-light coupling is incoherent and therefore the absorption of a photon is an irreversible process. The corresponding

interaction regime is referred to as weak-coupling regime. The typical time constant is imprinted by the exciton lifetime T_1.
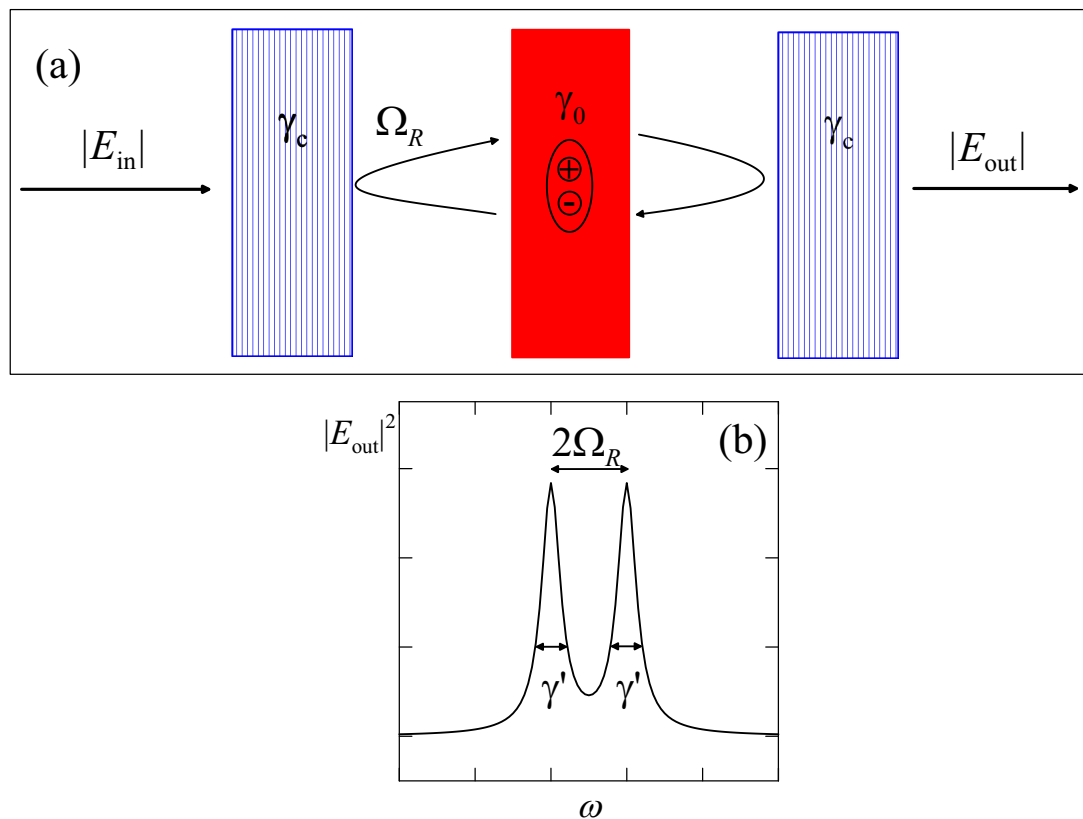
Figure 2.2: Rabi splitting and strong coupling: (a) schematic set-up of a semiconductor microcavity with losses γ_c due to the Fabry-Pérot mirrors and excitonic losses γ_0; the strength of the exciton-photon coupling is proportional to the Rabi frequency Ω_R; (b) schematic emission spectrum of the strongly coupled system with Rabi oscillations in arbitrary units; the linewidths are given by the mean loss constant $\gamma' := (\gamma_0 + \gamma_c)/2$.

However, this conventional picture is only appropriate in the weak-coupling regime. Reducing the excitonic and photonic losses as well as the dephasing leads to other effects arising from the coherent interaction of excitons and cavity photons that require a different description. In this picture, it is sensible to interpret both excitons and photons as interacting quantum mechanical oscillators, cf. Fig. 2.2(a). If we furthermore assume a vanishing detuning between them, we have two same-energy oscillators with respective decay rates. If their coupling strength exceeds the mean value $\gamma' := (\gamma_0 + \gamma_c)/2$ of the decay rates, the coupled system will enter the strong-coupling regime. The strong-coupling regime is characterized by the splitting of the spectrum into two eigenenergies. This effect is known as Rabi splitting [12, 127], cf. Fig. 2.2(b). The numerical value of the Rabi splitting is equal to twice the product of the transition dipole moments and the energy stored in the vacuum field. The expression Rabi splitting was coined in the framework of single atoms. Actually, this denotation can also be applied in case of many-atom systems such as semiconductor quantum wells. The exciton-photon interaction constant

is proportional to the Rabi splitting Ω_R, cf. Fig. 2.2. In contrast to the weak-coupling regime, the coherent interaction of excitons and photons in the strong-coupling regime is a reversible process [127–133]. The typical time constant is the dephasing time T_2. Due to the high Q mirrors, the photons have such a high lifetime in the cavity, that they can interact with the excitons multiple times, cf. Fig. 2.2(a). Hence, excitons and photons have to be described by a joint wave function. However, the saturation of the strong-coupling regime due to electron-hole pair screening of the quantum-well exciton also has to be taken into account [134]. In the case of an InGaAs quantum well, it leads to saturation densities of $4.3 \cdot 10^{10}$ cm^{-2} which is in good agreement with the theoretical prediction from Ref. [135].

The dispersion relation of the exciton-polariton arises from the anticrossing of the two dispersion relations and is substantially different from both of them. It consists of two branches which are separated by the Rabi splitting. The dispersion relation will be discussed in Sec. 5.1. The genuinely new shape of the dispersion relation reflects the fact, that exciton-polaritons represent the non-perturbative coupling between the electromagnetic field and the optically induced polarization of the matter.

2.1.4. Quantum description of exciton-photon coupling

However, the semiclassical treatment of light-matter coupling as it was discussed in the previous paragraph can be insufficient in some cases. A full quantum description is needed, when single-photon processes play a role [136]. The shape of the emission spectrum is an indicator showing how far the system is from the true quantum regime. According to Ref. [137], pump-probe experiments yield a photon density of about 90 photons per μm^2 for the saturation of normal-mode coupling. This value for the photon density can be reduced drastically by decreasing the diameter of the probe beam or alternatively by decreasing the size of the active semiconductor material. Actually, in order to enter the true quantum regime, it turns out that the use of quantum dots is essential [131, 138]. Then, single-photon processes can be observed in semiconductor microcavities such as in the case of single-atom vacuum Rabi splitting in a cavity [139].

Since this work solely deals with quantum wells, it suffices to treat the exciton-photon interaction semiclassically.

2.2. Equations of motion of exciton-polaritons

2.2.1. Exciton-polariton Hamiltonian

The Hamiltonian $\hat{H}$ for the semiclassical treatment of the formation and dynamics of exciton-polaritons reads [47, 140]

$$\hat{H} = \hat{H}_{\mathrm{cav}} + \hat{H}_{\mathrm{exc}} + \hat{H}_{\mathrm{lm}}. \tag{2.7}$$

$\hat{H}_{\mathrm{cav}}$ describes the dynamics of the cavity photons, $\hat{H}_{\mathrm{exc}}$ contains all excitonic contributions and $\hat{H}_{\mathrm{lm}}$ describes the mutual interaction between both types of quasiparticles (light-matter interaction). With $\hat{a}_{\mathbf{k}}^{\dagger}$ and $\hat{a}_{\mathbf{k}}$ being the creation and annihilation operator for a cavity photon with wave vector $\mathbf{k}$, respectively, and $\hat{b}_{\mathbf{k}}^{\dagger}$ and $\hat{b}_{\mathbf{k}}$ being the respective operators for excitons, the contributions to the total Hamiltonian read

$$\hat{H}_{\mathrm{cav}} = \sum_{\mathbf{k}} \omega_{\mathrm{cav}}(\mathbf{k})\hat{a}_{\mathbf{k}}^{\dagger}\hat{a}_{\mathbf{k}}, \ \hat{H}_{\mathrm{exc}} = \sum_{\mathbf{k}} \omega_{\mathrm{exc}}(\mathbf{k})\hat{b}_{\mathbf{k}}^{\dagger}\hat{b}_{\mathbf{k}} + \hat{H}_{\mathrm{XX}}, \ \mathrm{and} \ \hat{H}_{\mathrm{lm}} = \frac{\Omega_R}{2}\sum_{\mathbf{k}} \left(\hat{a}_{\mathbf{k}}^{\dagger}\hat{b}_{\mathbf{k}} + \hat{b}_{\mathbf{k}}^{\dagger}\hat{a}_{\mathbf{k}} \right). \tag{2.8}$$

Here, $\omega_{\mathrm{cav}}(\mathbf{k})$ is the dispersion relation of the photonic state with wave vector $\mathbf{k}$. The sum runs over all allowed $\mathbf{k}$ states. Analogously, $\omega_{\mathrm{exc}}(\mathbf{k})$ is the dispersion relation of the excitonic state with wave vector $\mathbf{k}$. Since we only consider resonant experiments with excitons formed by an electron in the valence band and a heavy hole[b] in the conduction band, the $\mathbf{k}$ sum runs over all possible excitonic states obeying this dispersion relation. This two-band description is typical for direct semiconductors such as GaAs. The Coulomb interaction between two excitons shall be denoted by $\hat{H}_{\mathrm{XX}}$. This term bears the nonlinearity since it contains both two creation and two annihilation operators. A theoretical model of the exciton-exciton scattering was provided in Ref. [141]. Reference [142] contains a detailed theoretical and experimental study of the biexciton.

In order to discuss the linear polariton dynamics first, we introduce the linearized Hamiltonian $\hat{H}_0$ via

$$\hat{H} = \hat{H}_0 + \hat{H}_{\mathrm{XX}}. \tag{2.9}$$

Then $\hat{H}_0$ is the Hamiltonian of two coupled harmonic oscillators and therefore bilinear in the ladder operators [c]. Therefore it can be diagonalized by means of a Bogoliubov

---

[b]The energy of the heavy hole is lower than that of the light hole. Therefore it is needed for the formation of a ground state exciton. This fact will play an important role in Sec. 3.1 when we additionally take into account the spin of the excitons. Heavy holes have spin $\pm 3/2$ compared to $\pm 1/2$ of light holes.

[c]$\hat{H}_0$ looks similar to the Jaynes-Cummings Hamiltonian (JCH) modelling the interaction between a two-level system and cavity photons. The crucial difference lies in the treatment of the matter contribution: whereas $\hat{H}_0$ solely contains bosons, the JCH contains a fermion-boson coupling incorporated by the respective fermionic operators. In Appendix A we discuss why excitons can be treated as bosons and

transformation [40, 140, 143]. The coefficients of this unitary transformation are called *Hopfield coefficients* [143]. They will be introduced properly in Sec. 5.1 in the framework of the linear polariton dispersion relation. At this point, however, the equations of motion shall be developed in the basis of excitons and cavity photons.

The nonlinear contribution $\hat{H}_{\text{XX}}$ to the Hamiltonian comes from the Coulomb interaction between two excitons. A feasible expression for it can be deduced from the Hartree-Fock approximation of the respective Hamiltonian in second quantization. $\hat{H}_{\text{XX}}$ then reads

$$\hat{H}_{\text{XX}} = \frac{1}{2} \sum_{\mathbf{k}, \mathbf{k}', \mathbf{q}} V_{\text{XX}}(\mathbf{q}) \, \hat{b}^{\dagger}_{\mathbf{k}+\mathbf{q}} \hat{b}^{\dagger}_{\mathbf{k}'-\mathbf{q}} \hat{b}_{\mathbf{k}} \hat{b}_{\mathbf{k}'}. \tag{2.10}$$

As stated before, the effective interaction potential $V_{\text{XX}}(\mathbf{q})$ is determined by the Coulomb interaction between two excitons. $\mathbf{q}$ denotes the momentum transfer in the course of an elastic exciton-exciton scattering. Since resonantly excited excitons have very small wave vectors, $V_{\text{XX}}(\mathbf{q})$ can be approximated by its zero wave vector value $V_{\text{XX}}(\mathbf{0}) = \frac{6e^2\lambda_{\text{exc}}}{A\epsilon}$. Here, λ_{exc} is the exciton radius and A denotes the macroscopic quantization area. The static dielectric constant ϵ of the quantum well is introduced heuristically in order to take into account the electrostatic screening of the interaction originating from the carriers of the crystal [120].

2.2.2. Heisenberg equations of motion

The equations of motion for an operator $\hat{c}_{\mathbf{k}}$ can be determined via the Heisenberg equation $i\partial_t \hat{c}_{\mathbf{k}} = \left[\hat{H}, \hat{c}_{\mathbf{k}} \right]$. For the annihilation operators they read

$$\partial_t \hat{a}_{\mathbf{k}} = i\omega_{\text{cav}}(\mathbf{k})\hat{a}_{\mathbf{k}} + \frac{i\Omega_R}{2}\hat{b}_{\mathbf{k}}, \tag{2.11}$$

$$\partial_t \hat{b}_{\mathbf{k}} = i\omega_{\text{exc}}(\mathbf{k})\hat{b}_{\mathbf{k}} + \frac{i\Omega_R}{2}\hat{a}_{\mathbf{k}} + 2\,i\,V_{\text{XX}}(\mathbf{0}) \left(\hat{b}^{\dagger} \star \hat{b} \star \hat{b} \right)_{\mathbf{k}}. \tag{2.12}$$

We exploited the fact that $V(\mathbf{q})$ can be approximated by $V(\mathbf{0})$. The $\star$ symbol denotes the convolution of the fields. The commutation rules for bosonic ladder operators and the computation of the Coulomb term can be found in App. A.

An averaging procedure leads to macroscopic fields $E_{\mathbf{k}} = \langle \hat{a}_{\mathbf{k}} \rangle$ and $\Psi_{\mathbf{k}} = \langle \hat{b}_{\mathbf{k}} \rangle$. A Fourier transformation then yields the equations of motion in position space. It is useful to specify the dispersion relations at this point. The dispersion relation of cavity photons reads $\hbar\omega_{\text{cav}}(\mathbf{k}) = \hbar^2\mathbf{k}^2/2m_{\text{ph}}$. Upon Fourier transformation this transforms to the negative transverse Laplacian $\mathbf{k}^2 \rightarrow -\nabla^2_{\perp} = -\partial^2_x - \partial^2_y$.

---

enlist their operator algebra.

Since the effective mass of the of the cavity photons is much smaller than that of the excitons, they can be assumed to be nearly dispersionless[d]. Two further contributions have not been taken into account yet and will be added heuristically to the final equations of motion[e]: The first of them is linked with the losses discussed in Sec. 2.1. They are called γ_c and γ_0 denoting the photonic and excitonic damping constant, respectively. These losses can be compensated by a coherent external optical pump $E_p e^{-i\omega_p t}$ with amplitude E_p and frequency ω_p.

After having collected all these parts, we can write down the full dimensionless equations of motion in position space

$$\partial_t E = -\left(\gamma_c - i\Delta_c\right) E + i\nabla_\perp^2 E + i\Psi + E_p, \tag{2.13}$$

$$\partial_t \Psi = -(\gamma_0 - i\Delta_0)\Psi - i|\Psi|^2\Psi + iE. \tag{2.14}$$

The scaled photonic field is denoted with E, the excitonic field with Ψ. The first order time derivative characterizes mean-field models. A rigourous derivation of the wave equation for the electric field from Maxwell's equations would have led to second order time derivatives. For the sake of better readability, the dependence of the fields on the transverse coordinates is not mentioned explicitly. Time is measured in units of $1/\Omega_R$. The parameters $\Delta_{c,0} = (\omega_p - \omega_{c,0})/\Omega_R$ describe the detuning of the pump frequency ω_p from the resonance frequencies of the cavity (ω_c) and of the excitons (ω_0), respectively. The transverse coordinates x and y are normalized to $x_0 = \sqrt{c/(2n\hat{k}\Omega_R)}$, where n is the refractive index and $\hat{k} = n\omega/c$ the wave number. The pump is normalized such that the incident pump intensity is $I_{\text{inc}} = \hbar\omega\Omega_R^2|E_p|^2/g\gamma_c$ [24, 40, 148]. The loss rates will be set $\gamma_0 = \gamma_c = 0.1$ in all numerical simulations. This implies that a time of $t = 10$ corresponds to a photon lifetime.

2.3. Chapter summary and concluding remarks

In this chapter, the equations of motion for exciton-polaritons in a coherently driven semiconductor microcavity were derived. Starting point for this derivation was the Hamiltonian for the interaction between excitons and cavity photons in second quantization. An averaging process then leads to the equations of motion for the photon field E and the

---

[d]This approximation is justified, as long as one regards processes which are sufficiently far away from the excitonic resonance. For processes near the excitonic resonance, the excitonic dispersion has to be taken into account [144–146].

[e]These contributions could also be introduced at the level of the Hamiltonian by coupling the system to an external reservoir, cf., e.g., Ref. [140] or Ref. [147] using a Lindblad formalism. We refrained from this approach thus keeping an undisturbed focus on the basic interaction processes.

polariton field Ψ. If the coupling strength between excitons and photons is larger than the losses, they enter the strong-coupling regime. The strong coupling manifests itself in Rabi oscillations between the two quantum fields. The Coulomb interaction between two excitons leads to a third order nonlinearity in the exciton equation. It should be noted that this chapter solely presents the scalar equations whereas vectorial effects originating from the exciton spin and the TE-TM splitting between the cavity modes are transferred to Chapt. 3.

3. Spin and polarization effects

After having introduced excitons, we also have to deal with their internal properties, namely their spin degree of freedom. In the course of its optical creation, an exciton-polariton inherits spin and dipole moment from the exciton. In Sec. 3.1 the nonlinear interaction between excitons with different spins is added to the scalar polariton Hamiltonian (2.7). Due to the hybrid nature of exciton-polaritons, this spin is intrinsically tied to the polarization properties of the photonic part, which is reflected in TE-TM splitting of the respective modes. It acts as an effective magnetic field on the polaritons. The linear pseudospin precession associated with this field will be dealt with in Sec. 3.2. Both effects lead to an augmentation of the scalar equations of motion (2.13)-(2.14).

3.1. Spin effects

3.1.1. Exciton spin

An exciton is a bound state of an electron in the conduction band and a hole in the valence band. Since both constituents are fermions, the projection of their respective spins on the structure growth axis is always half-integer. It is reasonable to identify this axis with the z axis. In the following, all projections have to be understood with respect to this z axis. Whereas for electrons, the projection of the total angular momentum equals that of the spin ($J_z^e = S_z^e = \pm\frac{1}{2}$), the projection of the hole's total angular momentum[a] is the sum of that of the spin and that of the mechanical angular momentum ($J_z^h = S_z^h + M_z^h = \pm\frac{1}{2}, \pm\frac{3}{2}$). Light holes are characterized by antiparallel S_z^h and M_z^h netting $J_z^h = \pm\frac{1}{2}$. One the other hand, heavy holes have $J_z^h = \pm\frac{3}{2}$ due to the parallelity of S_z^h and M_z^h. In quantum wells, the energy levels of the heavy holes are lower than those of light-holes [3, 111, 149–151]. Therefore, the ground state exciton is usually formed by an electron and a heavy hole. The total exciton spin J can thus take the values ± 1 and ± 2. In order to guarantee spin conservation in the framework of single-photon processes, only excitons with spin ± 1 can be excited. The states with $J = \pm 2$ are called dark states, since they are not optically excitable. The optically excitable bright states, however, can be regarded as a bosonic two-level system. This is an extraordinary feature, since two-level systems are usually

---

[a]It is common in the field of polariton physics to call J spin. We will adopt this denotation in the current work.

formed by fermions. The possible use of semiconductor microcavities as spin-dependent optoelectronic devices is discussed in Ref. [53].

Excitons are subjected to various spin-relaxation mechanism [3, 111, 152–154]. These mechanisms are responsible for the finite exciton lifetime discussed in Sec. 2.1. The predominant relaxation mechanism for excitons confined in a quantum well involves mutual spin-flip exchange interactions of electrons and holes [155, 156]. The Coulomb interaction consists of a short-range part leading to the coupling between heavy-hole and light-hole excitons and a long-range part leading to transitions between the optically excitable heavy-hole excitons. The short-range interaction allows the alteration of the optical response via the interaction between dark-state excitons [157]. However, it is suppressed for quantum well excitons since the degeneracy between light and heavy holes is lifted [155].

3.1.2. Exciton-exciton interaction Hamiltonian

Without taking into account the exciton spin, the Coulomb interaction between two excitons could be described with $\hat{H}_{\mathrm{XX}}$, cf. Eq. (2.10). This term will be preserved in the spin-dependent model derived in this section, namely it will represent the nonlinear interaction between two excitons with equal spin:

$$\hat{H}_{\mathrm{XX,sym}} = \frac{1}{2} \sum_\sigma \sum_{\mathbf{k},\mathbf{k}',\mathbf{q}} V_{\mathrm{XX,sym}}(\mathbf{q})\, \hat{b}^\dagger_{\mathbf{k}+\mathbf{q},\sigma} \hat{b}^\dagger_{\mathbf{k}'-\mathbf{q},\sigma} \hat{b}_{\mathbf{k},\sigma} \hat{b}_{\mathbf{k}',\sigma}. \tag{3.1}$$

The σ sum runs over the integer values $\sigma = +1$ and $\sigma = -1$. $V_{\mathrm{XX,sym}}(\mathbf{q})$ denotes the matrix element of the exciton-exciton scattering in triplet configuration (parallel spins) with momentum transfer $\mathbf{q}$. The contribution of the singlet configuration (antiparallel spins) reads

$$\hat{H}_{\mathrm{XX,asym}} = \frac{1}{4} \sum_\sigma \sum_{\mathbf{k},\mathbf{k}',\mathbf{q}} V_{\mathrm{XX,asym}}(\mathbf{q})\, \hat{b}^\dagger_{\mathbf{k}+\mathbf{q},\sigma} \hat{b}^\dagger_{\mathbf{k}'-\mathbf{q},-\sigma} \hat{b}_{\mathbf{k},\sigma} \hat{b}_{\mathbf{k}',-\sigma} \tag{3.2}$$

with $V_{\mathrm{XX,asym}}(\mathbf{q})$ being the respective matrix element [151].

All other contributions to the polariton Hamiltonian do not contain contributions mixing the two exciton spins. Thus, the scalar equations of motion (2.13)-(2.14) are reproduced in the vectorial equations of motion. Additionally, there is a contribution to the excitonic equations of motion originating from the spin-mixing Hamiltonian $\hat{H}_{\mathrm{XX,asym}}$. The contribution of $\hat{H}_{\mathrm{XX,asym}}$ to the final equations of motion can be brought to the form

$$\partial_t \Psi^\sigma \propto \alpha \left| \Psi^{-\sigma} \right|^2 \Psi^\sigma \tag{3.3}$$

where the factor α comes from the Fourier transform of $V_{\mathrm{XX,asym}}(\mathbf{0})$. The full equations of motion thus read

$$
\begin{aligned}
\partial_t E^\pm &= -\left(\gamma_c - i\Delta_c\right) E^\pm + i\nabla_\perp^2 E^\pm + i\Psi^\pm + E_p^\pm, && (3.4)\\
\partial_t \Psi^\pm &= -(\gamma_0 - i\Delta_0)\Psi^\pm - i\left(|\Psi^\pm|^2 + \alpha|\Psi^\mp|^2\right)\Psi^\pm + iE^\pm. && (3.5)
\end{aligned}
$$

From now on, the superscript $\pm$ replaces the notation with $\sigma = \pm 1$.

3.1.3. Numerical value of the cross-phase modulation parameter α

The parameter α in Eq. (3.5) describes the cross-phase modulation between polaritons with pseudospin $+1$ and -1. This is the only term in Eqs. (3.4)-(3.5) that mixes the two fields. The determination of the numerical value of α and even of its sign is discussed controversially. In the following, a brief overview of this discussion will be presented.

A theoretical model of the exciton-exciton scattering in a semiconductor quantum well including the inter-exciton exchange of carriers and the spin degrees of freedom was presented in Ref. [141]. The influence of the cavity on the electron-hole spin flip of polaritons was investigated in Ref. [158]. The spin flip rate was found to be suppressed by four orders of magnitude compared to the bare quantum well case and therefore unmeasurable. This suppression comes from the Rabi splitting between the optically excitable and optically forbidden transitions lifting their former degeneracy.

The assumption of α being negative and small compared to 1 is state of the art [149]. The authors of Ref. [149] additionally found a strong dependence of α on the relative detuning between the excitonic and the photonic resonance which would allow values for α ranging from 0 to less than -1.

However, there is evidence that under certain circumstances α can also be positive [159]. This repulsive interaction in the singlet configuration is explained by its proximity to the biexciton resonance and by effects originating from the onset of exciton saturation for sufficiently high exciton densities. The experimental findings discussed in the supplementary material of Ref. [159] even indicate the possibility of $\alpha > 1$.

The sign of α plays a crucial role in all our calculations in the following chapters since only for $\alpha < 0$ there is a spontaneous symmetry breaking between the two polarizations. This will be predicted analytically in terms of plane-wave solutions of Eqs. (3.4)-(3.5) and verified for various nonuniform solutions.

3.2. TE-TM splitting

In the previous section it was shown that the exciton spin is intrinsically tied to the polarization state of the cavity photons. In this section, the contribution of the TE-TM splitting between the cavity modes to the equations of motion will be derived. The linear pseudospin precession associated with this effect can be traced back to an effective magnetic field acting on the polaritons. Since it is a linear effect, its pure occurrence can be accessed experimentally in the linear regime, e. g., a pump range where the intensity of the optical excitation is small enough such that the effects of nonlinear polariton-polariton interaction do not play a crucial role and can therefore be neglected.
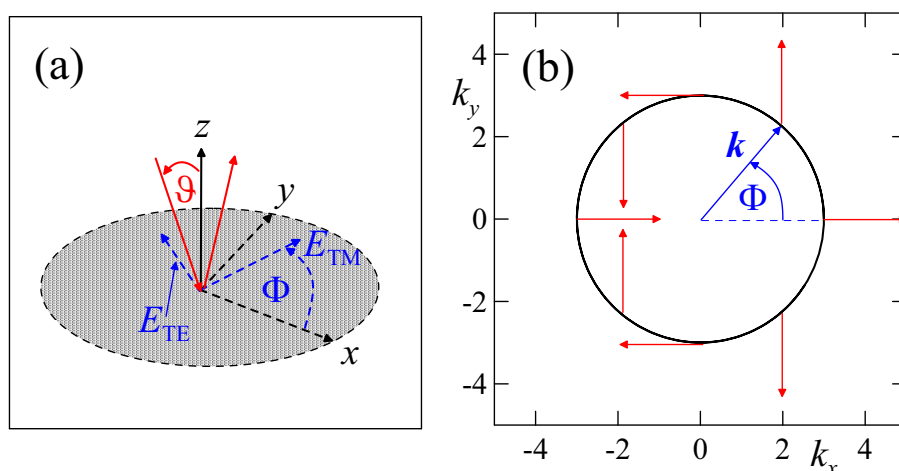

Figure 3.1: (a) Geometry of TE-TM splitting: The wave vector of the incoming electric field and the z axis span the plane of incidence, where ϑ denotes the tilt angle of the electric field; all vectors in this plane are displayed by solid lines; the quantum well is positioned in the x-y plane; all vectors in this plane are displayed by dashed lines; E_{TE} and E_{TM} denote the projection of the transverse electric and the transverse magnetic component of the electric field on the x-y plane, respectively; Φ denotes the azimuthal angle; (b) dependence of the direction of the effective magnetic field on the azimuthal angle Φ.

The TE-TM splitting of the polariton modes is mainly governed by the TE-TM splitting of the cavity modes. The transmissivity τ of a Fabry-Pérot cavity obeys the Airy formula

$$\tau = \frac{1}{1 + \mathcal{F}\sin^2\frac{\delta}{2}}. \tag{3.6}$$

Here, $\mathcal{F}$ denotes the finesse of the cavity. It is proportional to the Q factor. The resonances of the cavity can be derived by calculating the minima of the denominator. The total phase shift accumulated by the field in one round trip in the cavity is denoted with δ. It amounts

$$\delta = 2\left(k_z L_c + \phi\right), \tag{3.7}$$

where the phase jumps acquired from the reflection at the mirrors are contained in ϕ. The

value of ϕ is different for TE and TM polarized fields. Hence there is a difference between their respective resonance frequencies.

Following the analysis of Ref. [160], the dependence of the TE-TM splitting $\Delta_{\text{TE-TM}} := \omega_{\text{TM}}(\vartheta) - \omega_{\text{TE}}(\vartheta)$ on the angle ϑ according to Fig. 3.1(a) reads

$$\Delta_{\text{TE-TM}} \propto \frac{2\cos\vartheta_{\text{eff}}\sin^2\vartheta_{\text{eff}}}{1 - 2\sin^2\vartheta_{\text{eff}}}. \tag{3.8}$$

The effective angle ϑ_{eff} is linked with ϑ via $\omega_m(\vartheta) = \omega_m(0)/\cos\vartheta_{\text{eff}}$ where $\omega_m(\vartheta)$ denotes the cavity-mode frequency. This TE-TM splitting vanishes for normal incidence and increases basically with $\sin^2\vartheta_{\text{eff}}$. For sufficiently small angles ϑ, this translates to a quadratic dependence on the modulus k of the in-plane wave vector [111, 154]:

$$\Delta_{\text{TE-TM}} \approx \widetilde{\beta}\left(k_x^2 + k_y^2\right). \tag{3.9}$$

Here, $\widetilde{\beta}$ can be denoted TE-TM splitting parameter. Its numerical value can be deduced from Ref. [154], where a TE-TM splitting of about 1.25 meV/$\hbar$ at a wave vector of about 3 μm^{-1} is reported.

After having spotted the existence of the TE-TM splitting, it has to be incorporated into the Hamiltonian and finally into the equations of motion. For that, we express this splitting in coordinates representing the TE- and TM-polarized mode and transform it then via Cartesian coordinates to the necessary basis of left- and right-circularly polarized cavity photons [161]. In coordinates adapted to the TE and TM modes, the Hamiltonian equation of motion has the diagonal form

$$i\hbar\frac{\partial}{\partial t}\begin{pmatrix} E_{\text{TE}} \\ E_{\text{TM}} \end{pmatrix} = \hbar\begin{pmatrix} \frac{\Delta_{\text{TE-TM}}}{2} & 0 \\ 0 & -\frac{\Delta_{\text{TE-TM}}}{2} \end{pmatrix}\begin{pmatrix} E_{\text{TE}} \\ E_{\text{TM}} \end{pmatrix}. \tag{3.10}$$

The change-of-base matrix to Cartesian coordinates reads [162]

$$M_1 = \frac{1}{\sqrt{2}}\begin{pmatrix} 1 & i \\ 1 & -i \end{pmatrix}. \tag{3.11}$$

The coordinate transformation from Cartesian to circularly polarized coordinates is given by

$$M_2 = \begin{pmatrix} \cos\Phi & -\sin\Phi \\ \sin\Phi & \cos\Phi \end{pmatrix}, \tag{3.12}$$

where Φ is the polar angle in the plane spanned by E_x and E_y, cf. Ref. [161] and Fig. 3.1(a). In the circularly polarized coordinates $(E^+, E^-)^t = M_2 M_1 (E_{\text{TE}}, E_{\text{TM}})^t$ the

Hamiltonian equations of motion are transformed to

$$i\hbar \frac{\partial}{\partial t} \begin{pmatrix} E^+ \\ E^- \end{pmatrix} = \frac{\hbar \Delta_{\text{TE-TM}}}{2} \widetilde{H}_{\text{TE-TM}} \begin{pmatrix} E^+ \\ E^- \end{pmatrix}, \tag{3.13}$$

where the transformed Hamiltonian reads

$$\widetilde{H}_{\text{TE-TM}} = \begin{pmatrix} 0 & \cos 2\Phi + i \sin 2\Phi \\ \cos 2\Phi - i \sin 2\Phi & 0 \end{pmatrix} = \frac{1}{k^2} \begin{pmatrix} 0 & (k_x - ik_y)^2 \\ (k_x + ik_y)^2 & 0 \end{pmatrix}. \tag{3.14}$$

This dependence on 2Φ instead of just Φ is visualized in Fig. 3.1(b). The factor $1/k^2$ in Eq. (3.14) cancels with the factor k^2 from $\Delta_{\text{TE-TM}}$, cf. Eq. (3.9).

After backtransformation into real space, the final equations of motion for exciton-polaritons with spin and TE-TM splitting read

$$\partial_t E^\pm = -(\gamma_c - i\Delta_c) E^\pm + i\nabla_\perp^2 E^\pm + i\Psi^\pm - i\beta \left(\partial_x \mp i\partial_y\right)^2 E^\mp + E_p^\pm, \tag{3.15}$$

$$\partial_t \Psi^\pm = -(\gamma_0 - i\Delta_0)\Psi^\pm - i\left(|\Psi^\pm|^2 + \alpha|\Psi^\mp|^2\right)\Psi^\pm + iE^\pm. \tag{3.16}$$

Transforming $\widetilde{\beta}$ to its dimensionless counterpart yields $\beta = 0.05$, thus a value much smaller than unity. This value will be used in all simulations in Sec. 6.3.

3.3. Chapter summary and concluding remarks

Starting from the scalar case discussed in Chapt. 2, we derived the equations of motion for exciton-polaritons in a coherently driven semiconductor microcavity with the inclusion of terms originating from the exciton spin and the polarization states of the cavity photons linked with it. These terms can be embedded in the Hamiltonian formalism. The Coulomb interaction between two excitons then consists of two terms describing the effective interaction between excitons with equal and opposite spin, respectively. It should be noted that only optically excitable states are taken into account so that the influence of dark states is only represented indirectly in their contribution to the exciton-exciton interaction with different spin. Since the exciton spins $+1$ and -1 are coupled to the right- and left-circularly polarized photons, respectively, their contribution to the vectorial equations of motion originating from the energy splitting between TE- and TM-polarized cavity modes has to be taken into account, too. It manifests itself in a linear term which directly breaks the symmetry between the $+$ and $-$ fields and is often interpreted as an effective magnetic field due to this action.

4. Solutions of the equations of motion

In the preceding chapters, we derived the equations of motion of coherently pumped exciton-polaritons for three cases:

1. In the scalar case (cf. Sec. 2.2, Eqs. (2.13)-(2.14)) all effects arising from the exciton spin and the corresponding polarization of the photonic component are disregarded.

2. Taking into account the exciton spin and the nonlinear interaction between excitons with different spin leads to the vectorial equations (3.4)-(3.5), cf. Sec. 3.1.

3. These equations can be augmented further by additionally considering the linear coupling between the two polarization states due to the energy splitting between cavity modes with transverse electric and transverse magnetic polarization (TE-TM splitting), cf. Eqs. (3.15)-(3.16) in Sec. 3.2.

In the following chapters, we want to discuss several solutions of these partial differential equations (PDEs) starting with homogeneous solutions (HSs), i.e., solutions that have a constant amplitude both in time and the two transverse dimensions. Spatially extended and spatially localized structures nesting on a HS are discussed in Chapts. 6 and 7, respectively. Chapter 8 is devoted to the dynamics of one–dimensional walls between different HSs.

4.1. Typology of solutions

The fields E and Ψ in the equations of motion are not directly measurable, but the squares of their absolute values are proportional to the photon and exciton density per unit area, respectively, and can therefore be determined in an experiment. They can be interpreted as intensities and denoted with $I_E = |E|^2$ and $I_\Psi = |\Psi|^2$. In the spin-dependent case, it is reasonable to introduce the total intensity of the output field $I_E = |E^+|^2 + |E^-|^2$ and the respective quantity $I_\Psi = |\Psi^+|^2 + |\Psi^-|^2$ denoting the excitonic component of the total intensity. Another important quantity is the polarization degree $\rho_E = \left(|E^+|^2 - |E^-|^2\right)/I_E$ (or $\rho_\Psi = \left(|\Psi^+|^2 - |\Psi^-|^2\right)/I_\Psi$), which may vary between -1 and $+1$. Whereas linearly polarized solutions have a polarization degree of 0, the extreme cases $+1$ and -1 characterize left and right circularly polarized solutions, respectively. All intermediate values describe elliptically polarized output fields. The polarization

degree can be calculated at each site (x, y). For sufficiently complex structures, usually $\rho_E(x, y) \neq \rho_\Psi(x, y)$ holds. Linearly polarized solutions with $\rho_E(x, y) \equiv 0$ are called symmetric solutions since they can be reduced to the scalar equations by scaling all fields by $\sqrt{1 + \alpha}$. All other solutions are called asymmetric solutions. The latter can arise from symmetric solutions of Eqs. (3.4)-(3.5) (which are symmetric under the permutation of $+$ and $-$) via spontaneous symmetry breaking. On the other side, this symmetry is broken directly by the TE-TM splitting term. The polarization degree of the pump will be denoted with ρ_p. For a linearly polarized pump, which is always the case in the present work, it reads $\rho_\mathrm{p} = 0$.

4.2. Analytical and numerical techniques

In order to get a comprehensive understanding of the polariton dynamics, we use a combination of analytical and numerical techniques to solve the equations of motion. Since the direct numerical simulation is very time-consuming and does not allow for a complete understanding of the dynamics, it will be backed up with several analytical calculations and a powerful method which allows us to find stationary solutions in the vicinity of a known solution rather quickly.

4.2.1. Perturbation schemes for HSs

Methods of nonlinear dynamics and bifurcation theory providing an approximate description of the dynamics of the system in close vicinity of a bifurcation point are powerful tools helping to understand the physics behind the simulated results and the underlying principles. These analytical or semianalytical methods usually start from analytical solutions of the respective equations of motion and contain a perturbation expansion about these solutions. Therefore the results obtained by these methods are often only valid in a close vicinity of the expansion point. The only analytically accessible solutions are homogeneous solutions. Therefore they will be the starting points of all discussed perturbation schemes.

The fields E, Ψ and their complex conjugate fields $\overline{E}$, $\overline{\Psi}$ have to be treated independently in the perturbation scheme[a]. In the scalar case, a system of four equations arises from this ansatz whereas in the vectorial case one generally gets a system of eight equations.

---

[a]Alternatively, one could regard the respective real and imaginary parts of E and Ψ as independent quantities, which would lead to the same number of degrees of freedom.

After linearizing in the perturbations the arising system of linear equations can be written in matrix form.

The perturbation schemes can be adjusted to the symmetries of the expected solution. These adjustments include both requirements on the amplitude of the perturbations and on their dependence on the transverse coordinates. The stability of scalar HSs E_0 and Ψ_0 with respect to other HSs can be probed by setting $E = E_0 + \varepsilon_1 e^{\lambda t}$, $\Psi = \Psi_0 + \psi_1 e^{\lambda t}$ and analogously for their complex conjugate fields with independent perturbations ε_2 and ψ_2. As we will see in Sec. 5.2, $|\Psi_0|$ will be a reasonable choice for the order parameter. By varying it, one can distinguish between stable modes with $\Re\lambda(|\Psi_0|) < 0$ and unstable modes with $\Re\lambda(|\Psi_0|) > 0$. Together they form the characteristic S-shaped bistability curve. This scheme also works in the vectorial case with eight independent perturbations and two parameters $|\Psi_0^\pm|$ which have to fulfill the equations of motion (3.15)-(3.16). The set of these multistable HSs consists of symmetric and asymmetric HSs. The spontaneous destabilization of symmetric HSs in favor of asymmetric HSs can be analyzed via the antisymmetric perturbation scheme $E^\pm = E_0 \pm \varepsilon_1 e^{\lambda t}$, $\Psi^\pm = \Psi_0 \pm \psi_1 e^{\lambda t}$ and analogously for their complex conjugate fields containing only four independent perturbations.

So far, we solely considered spatially constant perturbation. Modulation instability of HSs, which leads to the formation of spatially periodic patterns, can be probed by a perturbation scheme including spatially periodic perturbations: $E^\pm = E_0 + \varepsilon_1^\pm e^{\lambda t} e^{i(k_x x + k_y y)}$ and analogously for $\Psi^\pm$ and their respective complex conjugate fields. Due to the symmetry of the vectorial equations of motion without TE-TM splitting, a decomposition into a symmetric and an asymmetric part is possible, cf. Subsec. 5.3.1. Adding the TE-TM splitting breaks this symmetry. Therefore, the full eight-dimensional perturbation scheme has to be solved, which is only possible semi-analytically, cf. Subsec. 5.3.4.

Whereas the aforementioned perturbation schemes are based on a Fourier decomposition and therefore particularly suitable for the prediction of periodic patterns, they fail to describes states without spatial periodicity such as solitons. Nevertheless, they can give an important hint even in this case, since the coexistence of HSs and periodic pattern arising from a subcritical bifurcation is a prerequisite for the existence of stable bright solitons.

4.2.2. Split-step Fourier method for the full PDEs

More complicated solutions than HSs cannot be calculated analytically. Therefore they have to be determined by numerically solving the equations of motion. A suitable tool for the time evolution of nonlinear PDEs like the full equations of motion for exciton-polaritons

is the given by the split-step Fourier method. In this pseudo-spectral method, the linear and the nonlinear contribution are regarded separately. Whereas the nonlinear part is solved in time domain using, e. g., a Runge-Kutta solver, the linear part containing the transverse Laplacian can favorably be solved in Fourier domain and then back-transformed. Eventually, both sub-steps are shifted by a half time step and therefore leapfrog each other. The numerical Fourier transform can be calculated relatively fast using the fast Fourier transform (FFT). Therefore, the split-step Fourier method can outperform typical finite-difference methods in terms of velocity and precision. Since we are interested in stationary solutions, we usually run the code until the solution reaches a steady state.

4.2.3. Newton iterative method for stationary solutions of the PDEs

Once a stationary solution is found with the help of the methods mentioned above, one can often find another solution nearby by slightly varying the pump power and then solving the system of linear equations arising from the spatial discretization with high precision using the Newton-Raphson method. This continuation technique relies on the fact that basically all solutions (HSs, patterns, solitons) can be regarded as points lying on a surface in the phase space spanned by the dynamical variables. Therefore they form branches with, e. g., the pump power as parameter. An important feature of this method is the possibility to produce solutions which would be unstable if one tries to simulate them directly with the split-step algorithm, which is in any case very time-consuming. Rotationally symmetric two-dimensional solutions such as stationary 2D solitons can be treated as quasi-one-dimensional solutions with this method by applying polar coordinates and transforming the transverse Laplacian to $\partial_x^2 + \partial_y^2 = \partial_r^2 + \frac{1}{r}\partial_r$. The stability of the solutions against perturbations lying in the same phase subspace can be determined from the eigenvalues of the Jacobian. In this manner, this method contributes to a more complete understanding of the system's dynamics. However, the size of the arising Jacobian matrix does not allow for generic two-dimensional solutions, but only for one-dimensional and rotationally symmetric two-dimensional ones. Therefore it will mainly be applied to one- and two-dimensional solitons and to domain walls, whereas for periodic patterns we have to rely on direct simulations.

4.3. Chapter summary and concluding remarks

This chapter links the previous with the subsequent chapters. Starting from the equations of motion we develop a typology of their solutions and their discrete symmetries. We

will distinguish between HSs, periodic patterns, cavity solitons and domain walls. In the vectorial case, symmetric and asymmetric solutions are possible and have equal rights, as long as the discrete symmetry between the two polarizations in the equations of motion is preserved. Since the TE-TM splitting breaks this symmetry, it enforces the formation of asymmetric solutions.

Then we presented several analytical and numerical solution techniques. In principle, the HSs can be calculated analytically both in the scalar and in the vectorial case. A perturbation scheme with spatially periodic perturbations then reveals the parameter range of modulation instability. The general equations of motion can be solved numerically by means of a split-step Fourier method. Stationary solutions can also be found via a Newton iterative solver. This method applies mainly to one-dimensional solutions and rotationally symmetric two-dimensional solutions. It allows the determination of branches depending on a parameter and generally consisting of both stable and unstable solutions.

5. Properties of homogeneous solutions

The easiest solutions of the partial differential equation describing the dynamics of uniformly pumped exciton-polaritons in the two-dimensional transverse plane are stationary plane waves. Since their modulus is independent on both the time and the transverse space coordinates, they are usually termed homogeneous solutions (HSs). This chapter gives an overview over various properties of HSs. The linear properties of HSs are reflected in the linear polariton dispersion relation presented in Sec. 5.1. The two-branch nature of this dispersion relation is rather extraordinary and gives rise to various characteristic effects. The TE-TM splitting of the cavity modes is also reflected in a splitting of the dispersion relation. A meaningful expression for the experimentally observed nonlinear blueshift of the linear dispersion relation will be calculated later in the framework of the perturbation analysis in Sec. 5.3. A typical property of cavities with Kerr nonlinearity is the bistable dependence of the fields on the input power. The additional consideration of the spin degree of freedom leads to an even richer variety of coexisting HSs which is termed multistability and dealt with in Sec. 5.2. By adding small perturbations to the HS, one can probe its stability with respect to solutions sharing the structure of these perturbations. This is an extremely powerful tool for the analytical prediction of bifurcations of the solutions and their dependence on the physical parameters, especially on α and β in Eqs. (3.15)-(3.16) which mix $+$ and $-$ polaritons.

HSs can give useful hints for the properties of spatially inhomogeneous solutions discussed in the following chapters. The existence range of the extended spatially periodic patterns discussed in Chapt. 6 can be predicted by analyzing the modulation instability (MI) of the HSs with respect to spatially periodic perturbations, cf. Sec. 5.3. The analysis presented in this section is taken from our publications [163, 164]. Also the solitons in Chapt. 7 always nest on a HS background and therefore inherit several properties of this background. Especially, the dependence of the solutions on the cross-phase modulation parameter α is predicted by means of a perturbation analysis of the HSs. These results were presented for the first time in our work [165]. The multistability of HSs presented in Sec. 5.2 leads to a competition between various HSs where they coexist. The dynamics of the arising one-dimensional domain walls between different HSs are discussed in Chapt. 8.

5.1. Dispersion relation

Since exciton-polaritons are composite quasiparticles formed by the strong coupling of excitons and cavity photons, one could expect their dispersion relation to inherit properties of both components. We will see, that the actual polariton dispersion relation arising from the anticrossing of these two dispersion relations shows an even richer behavior with both a photonic and an excitonic limiting case. Furthermore we will see that linear pseudospin properties such as TE-TM splitting will also be reflected in a further splitting of the linear dispersion relation.

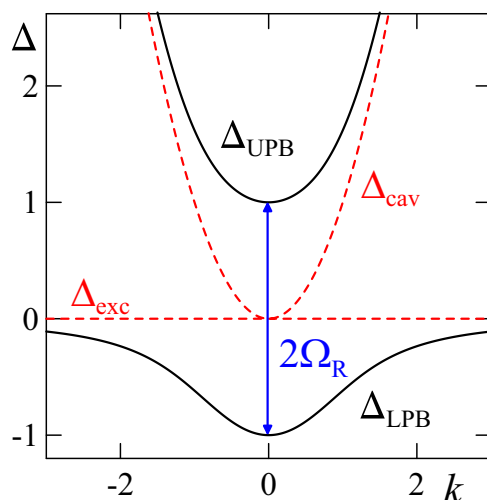### 5.1.1. Linear dispersion relation and Hopfield coefficients

Figure 5.1: Linear dispersion relation of scalar exciton polaritons: The upper polariton branch $\Delta_{\mathrm{UPB}}(k)$ and lower polariton branch $\Delta_{\mathrm{LPB}}(k)$ (bold black lines) arise from the anticrossing of the excitonic dispersion relation $\Delta_{\mathrm{exc}}(k)$ and the photonic dispersion relation $\Delta_{\mathrm{cav}}(k)$ (dashed red lines); their splitting at $k = 0$ amounts to twice the Rabi frequency Ω_R.

According to the derivation of the spinless equations of motion (2.13)-(2.14) the excitons have a plane dispersion relation , i. e., $\omega_{\mathrm{exc}}(k) = \mathrm{const}$ with $k^2 = k_x^2 + k_y^2$. This approximation uses the fact that the effective mass of the excitons is 10^4 to 10^5 times bigger than that of the cavity photons so that it can sufficiently well approximated by its value for $k = 0$. This approximation is valid as long as one stays sufficiently far away from the excitonic resonance. However, in order to describe processes like soliton formation above the excitonic resonance correctly, it would be necessary to include the parabolic exciton dispersion into the equations of motion [144–146]. In the following, the origin of the ordinate will be shifted into the excitonic resonance. Hence, all dispersion relations will not display the k dependence of the frequencies but rather that of the respective detunings. Furthermore, we switch to dimensionless quantities by scaling all frequencies with the Rabi

frequency Ω_R. This procedure is consistent with the scaling of the equations of motion (2.13)-(2.14). The excitonic dispersion relation can then be simplified to $\Delta_{\mathrm{exc}}(k) = 0$. The photonic dispersion relation, however, is parabolic , i. e., their frequency or rather their detuning[a] depends quadratically on the transverse wave vector: $\Delta_{\mathrm{cav}}(k) = k^2$ in suitably scaled coordinates. Both dispersion relations are shown by dashed red lines in Fig. 5.1.

In the previous chapter, the equations of motion were derived for excitons coupled to cavity photons. They are normal modes of the quantum well and the empty cavity, respectively. The normal modes of the coupled system, however, are exciton-polaritons. In the following, we want to derive their dispersion relation, i.e., the relation between the detuning $\Delta(k)$ and the transverse wave vector k. In the linear limit, it can be obtained by inserting $\{E, \Psi\} \propto \mathbf{p}(k) \exp\left(-\gamma t + i\left(\mathbf{kr} - \Delta(k)t\right)\right)$ into Eqs. (2.13)-(2.14) and dropping both the pump term and the nonlinearity. This leads to an eigenvalue problem with vector $\mathbf{p}(k) = \{e_k, \psi_k\}$ and eigenfrequency $\Delta(k)$. Solving the eigenvalue equation yields the two branches of the linear dispersion relation,

$$\Delta_{\mathrm{UPB,LPB}}(k) = \frac{k^2 \pm \sqrt{4 + k^4}}{2}, \tag{5.1}$$

where $\Delta_{\mathrm{UPB}}(k)$ and $\Delta_{\mathrm{LPB}}(k)$ refer to the upper and lower polariton branch, respectively, cf. the bold black lines in Fig. 5.1. The upper polariton branch $\Delta_{\mathrm{UPB}}(k)$ is photon-like. The lower polariton branch $\Delta_{\mathrm{LPB}}(k)$ is also photon-like around $k = 0$ and approaches the excitonic resonance for large values of k thus becoming exciton-like. In the intermediate range it experiences a change of its curvature leading to several effects characteristic for exciton-polaritons such as the formation of stable bright solitons [166–168]. At $k = 0$, the separation between the two branches amounts to $\delta\Delta = \Delta_{\mathrm{UPB}}(0) - \Delta_{\mathrm{LPB}}(0) = 2$. It is called Rabi splitting and always equals twice the Rabi frequency: $\delta\omega = 2\Omega_R$, cf. Fig. 5.1. The components of the vector $\mathbf{p}(k)$ denote the photonic component e_k and the excitonic component ψ_k of the respective branch. They can be calculated to

$$e_k^2 = \frac{1}{1 + (k^2 - \Delta_{\mathrm{UPB,LPB}}(k))^2} \qquad \text{and} \qquad \psi_k^2 = 1 - e_k^2. \tag{5.2}$$

They are also known as Hopfield coefficients [143]. The polariton dispersion curve can be determined experimentally via angle-resolved photoluminescence experiments, cf. Ref. [169]

---

[a]It should be noted that the detuning from the pump frequency may include a constant shift which is chosen zero in this case. This choice corresponds to $\Delta_c = \Delta_0$ in the equations of motion (2.13)-(2.14), which will actually be applied in most of the numerical simulations.

5.1.2. TE-TM splitting of the linear dispersion relation

Pseudospin effects linked with the parameter α in Sec. 3.1 solely appear in the nonlinear terms of the equations of motion. Hence they do not influence the linear dispersion relation discussed in this section. The TE-TM splitting of the cavity modes, however, is a linear effect and therefore has an impact on the linear dispersion relation. It causes a TE-TM splitting of both branches, which can be expressed by the substitution $k^2 \to \widetilde{k}^2 = k^2 \left(1 \pm \beta\right)$ in Eq. (5.1). The TE-TM split polariton branches then read

$$\Delta_{\text{UPB}}^{\pm}(k) = \frac{k^2 \left(1 \pm \beta\right) + \sqrt{4 + k^4 \left(1 \pm \beta\right)^2}}{2} \tag{5.3}$$

and

$$\Delta_{\text{LPB}}^{\pm}(k) = \frac{k^2 \left(1 \pm \beta\right) - \sqrt{4 + k^4 \left(1 \pm \beta\right)^2}}{2}. \tag{5.4}$$

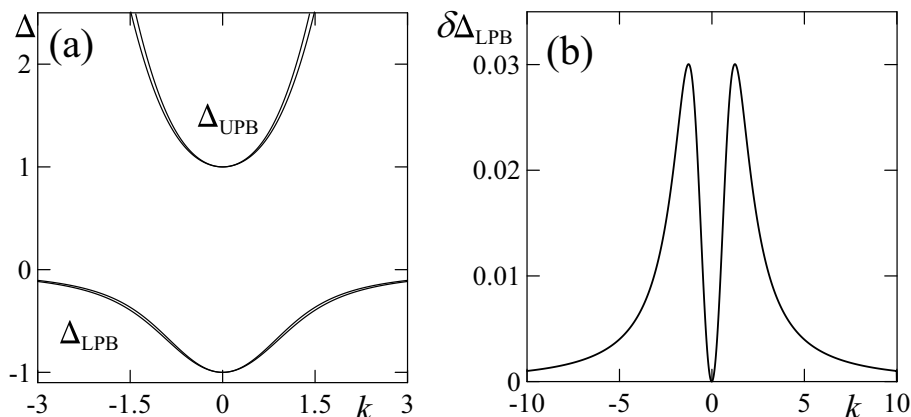They are shown in Fig. 5.2(a). It is remarkable that the dispersion relation remains

Figure 5.2: (a) TE-TM split upper branch $\Delta_{\text{UPB}}(k)$ and lower branch $\Delta_{\text{LPB}}(k)$ of the linear dispersion relation of exciton polaritons, (b) TE-TM splitting $\delta\Delta_{\text{LPB}}(k)$ of the lower polariton branch. The splitting parameter was chosen $\beta = 0.05$

isotropic in the $k_x - k_y$ plane, although the original equations of motion (3.15)-(3.16) do not exhibit this symmetry. A very good approximation[b] for the TE-TM splitting $\delta\Delta_{\text{UPB}} = \Delta_{\text{UPB}}^{+} - \Delta_{\text{UPB}}^{-}$ of the photon-like upper polariton branch is given by the formula

$$\delta\Delta_{\text{UPB}}(k) \approx \beta k^2 \left(1 + \frac{k^2}{\sqrt{4 + k^4}}\right). \tag{5.5}$$

It vanishes at $k = 0$, behaves like $\delta\Delta_{\text{UPB}} \propto \beta k^2$ for small k and $\delta\Delta_{\text{UPB}} \propto 2\beta k^2$ for large k. The TE-TM splitting $\delta\Delta_{\text{LPB}} = \Delta_{\text{LPB}}^{+} - \Delta_{\text{LPB}}^{-}$ of the lower polariton branch is

---

[b]The fact $\beta \ll 1$ is used in order to simplify the denominator.

approximately given by

$$\delta\Delta_{\mathrm{LPB}}(k) \approx \beta k^2 \left(1 - \frac{k^2}{\sqrt{4+k^4}}\right). \tag{5.6}$$

Its course is shown in 5.2(b). It vanishes for $k = 0$, since in this case there is no TE-TM splitting of the cavity modes. The TE-TM splitting of the lower polariton branch also vanishes for $k \to \infty$, since in that case, the excitonic effects dominate the photonic ones. It takes its maximum at about $k = \pm 1.25$.

5.2. Multistability

After having examined the linear properties of HSs in the previous section, we will include the pump and the repulsing instantaneous Kerr-type nonlinearity arising from the exciton-exciton interaction into our considerations. For the scalar case described by Eqs. (2.13)-(2.14), the output fields E, Ψ show a bistable dependence on the pump power, as long as $f(\Delta) > 0$ for [100, 170]

$$f(\Delta) = \Delta \left(\Delta^2 + \gamma_c^2 - 1\right) - \sqrt{3}\gamma_0 \left(\Delta^2 + \gamma_c^2 + \frac{\gamma_c}{\gamma_0}\right). \tag{5.7}$$

This means that the equations (2.13)-(2.14) exhibit bistable HSs for $-0.79516 < \Delta < -0.18994$ for $\gamma_0 = \gamma_c = 0.1$. The black lines in Fig. 5.3(a) and (b) show the square of the absolute value of the bistable symmetric HSs $|\Psi^{\pm}|$ of the vectorial equations (3.4)-(3.5) with $\Delta = -0.7$ for the cases $\alpha = 0.1$ and $\alpha = 0.2$, respectively. These symmetric HSs arise from the scalar HSs by scaling all fields and the pump with $\sqrt{1+\alpha}$. The solid lines always denote stable solutions whereas unstable solutions are marked with dashed lines. The stability of a HS with respect to other HSs can be probed by adding an arbitrary small perturbation with time dependence $\propto e^{\lambda t}$ to it and solving the eigenvalue problem arising from the respective equations of motion. If all eigenvalues have a negative real part, the HS is stable. If at least one eigenvalue has a positive real part the HS is unstable. This perturbation scheme works also for the asymmetric HSs discussed in the following.

Apart from these symmetric HSs, the spin degree of freedom gives rise to asymmetric HSs corresponding to an elliptically polarized photonic component. They bifurcate from the symmetric HSs when the latter become unstable with respect to antisymmetric perturbations. This destabilization can be examined by means of an adapted linear stability analysis about the symmetric HSs E_0 and Ψ_0. We plug the ansatz $E^{\pm} = E_0 \pm \varepsilon_1 e^{\lambda t}$, $\Psi^{\pm} = \Psi_0 \pm \psi_1 e^{\lambda t}$ and analogously for their complex conjugate fields $\overline{E}^{\pm} = \overline{E}_0 \pm \varepsilon_2 e^{\lambda t}$,
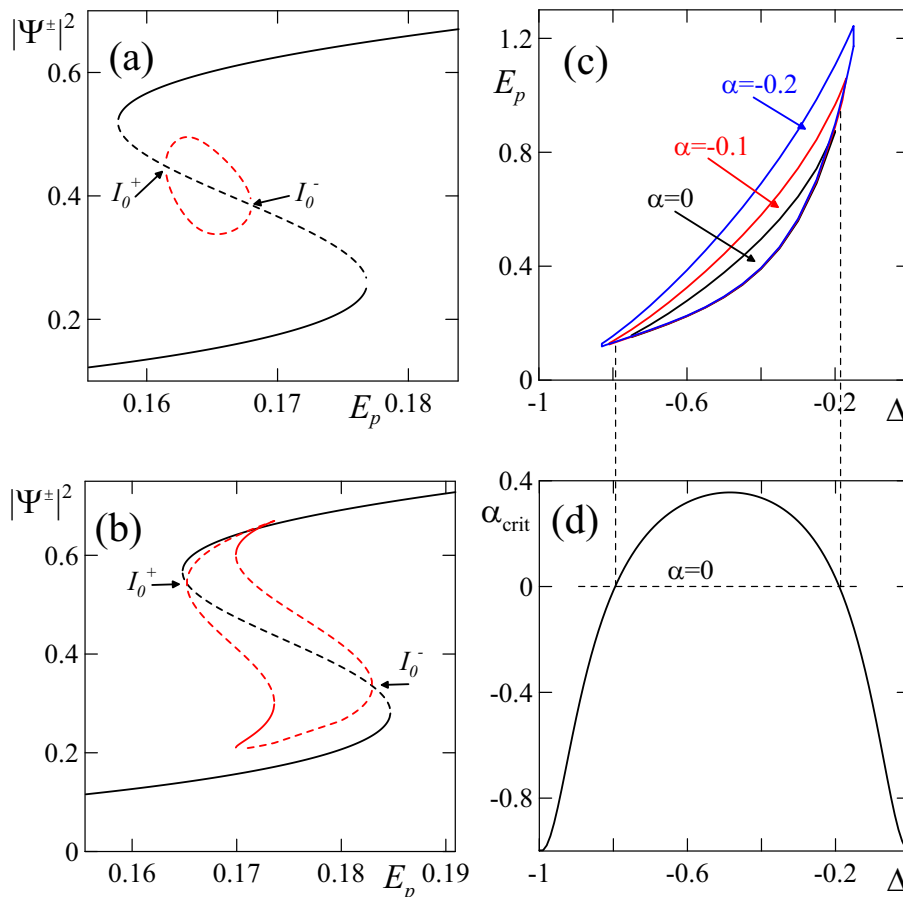
Figure 5.3: Left panel ((a) and (b)): Intensity of symmetric (black) and asymmetric (red) HSs vs. the external pump power E_p for (a) $\alpha = 0.2$ and (b) $\alpha = 0.1$ and a detuning of $\Delta = -0.7$, solid and dashed lines mark stable and unstable solutions, respectively; bifurcation points $I_0^{\pm}$ according to Eq. (5.9); (c) multistable pump range E_p vs. detuning Δ for various values of the nonlinear coupling parameter α; (d) critical α according to Eq. (5.10) where the asymmetric HS bifurcates from the symmetric one as a function of the detuning Δ.

$\overline{\Psi}^{\pm} = \overline{\Psi}_0 \pm \psi_2 e^{\lambda t}$ into the equations of motion (3.4)-(3.5). Note that the perturbations ε_1 and ε_2 have to be treated as independent quantities and are not necessarily the complex conjugate of each other. The same holds for ψ_1 and ψ_2. Furthermore, this ansatz solely takes into account the polarization symmetry breaking instability and disregards any other destabilization mechanisms known already for the one-component systems [24, 170] as, e.g., modulational instability. However, these mechanisms will be regarded extensively in Sec. 5.3 both for the scalar and the vectorial case. After linearizing all equations in the perturbations we get the eigenvalue equation

$$
\begin{pmatrix}
-\gamma_c + i\Delta_c & 0 & i & 0 \\
0 & -\gamma_c - i\Delta_c & 0 & -i \\
i & 0 & -\gamma_0 + i\Delta_0 - 2i\left|\Psi_0\right|^2 & -i\left(1 - \alpha\right)\Psi_0^2 \\
0 & -i & i\left(1 - \alpha\right)\overline{\Psi}_0^2 & -\gamma_0 - i\Delta_0 + 2i\left|\Psi_0\right|^2
\end{pmatrix}
\begin{pmatrix}
\varepsilon_1 \\
\varepsilon_2 \\
\psi_1 \\
\psi_2
\end{pmatrix}
= \lambda
\begin{pmatrix}
\varepsilon_1 \\
\varepsilon_2 \\
\psi_1 \\
\psi_2
\end{pmatrix}.
$$

(5.8)

The behavior of the perturbations is governed by the eigenvalue with the largest real part, which will be denoted with $\Re(\lambda)$. The perturbations are damped for $\Re(\lambda) < 0$ whereas they grow exponentially with time for $\Re(\lambda) > 0$. Therefore setting $\lambda = 0$ in the corresponding characteristic equations of the eigenvalue problem leads to an equation describing the bifurcation points where the symmetric HS destabilizes in favor of the asymmetric HSs (marked with I_0^+ and I_0^- in Fig. 5.3(a) and (b)). This approach is valid, since stationarity (or time-independence) of the asymmetric HS solution requires that the imaginary part of λ also vanishes close to the bifurcation point. The arising second-order equation for the HS intensity $I_0 = |\Psi_0|^2$ yields the solutions

$$I_0^\pm = \frac{-2\mathcal{B} \pm \sqrt{4\mathcal{B}^2 - (4 - (1 - \alpha)^2)(\mathcal{B}^2 + \mathcal{A}^2)}}{4 - (1 - \alpha)^2}, \tag{5.9}$$

where $\mathcal{A} = \gamma_0 + \gamma_c/(\gamma_c^2 + \Delta_c^2)$ and $\mathcal{B} = -\Delta_0 + \Delta_c/(\gamma_c^2 + \Delta_c^2)$. It can be seen from Figs. 5.3(a) and (b) that the existence range of asymmetric HSs gets smaller with increasing value of α. It finally vanishes completely above a critical value $\alpha = \alpha_{\text{crit}}$ where both bifurcation points coincide. This value is given by

$$\alpha_{\text{crit}} = 1 - \frac{2|\mathcal{A}|}{\sqrt{\mathcal{A}^2 + \mathcal{B}^2}}. \tag{5.10}$$

The value α_{crit} is shown in Fig. 5.3(d) as a function of the frequency detuning. The existence interval of the asymmetric HS becomes broader for decreasing value of α, which can be seen by comparing the red curves in Figs. 5.3(a) and (b). For $\alpha = 0$, it reaches the limiting points of the bistability curve. Note that for vanishing α the equations for the right and left polarization are uncoupled and, as a consequence, the polaritons with opposite spins can be switched on independently in the upper state of the bistable curve. In other words, each of the three polarizations, namely, the right-elliptical, the left-elliptical and the linear one, can be excited with a linearly polarized pump beam. This polarization multistability of HSs is also ubiquitous for the more realistic case of a negative nonlinear coupling parameter $\alpha < 0$. Moreover, the interval of polarization multistability exceeds the bistability domain of symmetric HS with the linearly polarized photonic component, as it is shown in Fig. 5.3 (c).

The dependence of the polarization degree of the output fields on the pump is studied in Refs. [171–173] for an elliptically polarized pump. Our approach is different, since we want to observe the transition from a symmetric state to a spontaneously broken asymmetric state applying a linearly polarized pump ($\rho_{\text{p}} = 0$). The multistability of polaritonic spin ensembles was also studied in Refs. [159, 174–176].

5.3. Modulation instability

In the preceding section, we investigated the properties of multistable HSs of the various equations of motion. We used two simple perturbation schemes to investigate the stability of HSs with respect to other HSs in general and especially we examined the destabilization of symmetric HSs in favor of asymmetric HSs using an adapted perturbation scheme. The HSs can furthermore be destabilized by the interplay between two competing processes: on the one hand there is the cross-talk mechanism between different sites mediated by the photon diffraction which tends to restore the spatial uniformity in the transverse plane and on the other hand the nonlinearity causes the amplification of spatial inhomogeneities. The interplay between these two processes generates an instability that is often termed Turing instability honoring the pioneering work of Turing [177]. Throughout this work, the synonymous denotation modulation instability (MI) will be used. In order to excite these instabilities, it is necessary that a control parameter, e. g., the pump power, exceeds a threshold value. This critical value is then also termed Turing destabilization point or MI point. A brief overview over the early history of MI is given in Ref. [7].

It is reasonable to regard the vectorial equations without TE-TM splitting and with TE-TM splitting separately. The former allow the deduction of various useful analytical formulae. Especially, they include the scalar problem as a symmetric special case. The latter, however, have to be treated partly numerically.

5.3.1. Perturbation scheme for the spin-dependent case without TE-TM splitting

We consider symmetric[c] HSs $E_0^+ = E_0^- =: E_0$ and $\Psi_0^+ = \Psi_0^- =: \Psi_0$ of the vectorial equations (3.4)-(3.5). The common scheme for spatially varying perturbations on top of the HSs and their complex conjugate fields $\overline{E}_0$ and $\overline{\Psi}_0$ reads as

$$
\begin{aligned}
E^\pm &= E_0 + \varepsilon_1^\pm e^{\lambda t} e^{i(k_x x + k_y y)}, \\
\overline{E^\pm} &= \overline{E}_0 + \varepsilon_2^\pm e^{\lambda t} e^{-i(k_x x + k_y y)}, \\
\Psi^\pm &= \Psi_0 + \psi_1^\pm e^{\lambda t} e^{i(k_x x + k_y y)}, \\
\overline{\Psi^\pm} &= \overline{\Psi}_0 + \psi_2^\pm e^{\lambda t} e^{-i(k_x x + k_y y)},
\end{aligned}
\tag{5.11}
$$

---

[c]Restricting the MI analysis to symmetric HSs is natural, since the solutions can be expected to inherit this property from the applied pump. It is also a prerequisite for the pattern formation discussed in Chapt. 6, where we will also solely cope with patterns driven by a linearly polarized pump and thus nesting on a linearly polarized HS. The extension to asymmetric HSs would be possible and straightforward.

where the perturbation amplitudes $\varepsilon_1, \varepsilon_2, \psi_1, \psi_2$ are independent in the ansatz (5.11). Since the equations of motion are isotropic in the x-y plane, all quantities depend only on the squared modulus $k^2 = k_x^2 + k_y^2$ of the transverse wave vector $\mathbf{k} = (k_x, k_y)^t$ rather than on its very components. The quantity $|\Psi_0|$ and the related excitonic intensity $I_0 = |\Psi_0|^2$ are suitable candidates for the system's control parameter rather than the pump power. Plugging the ansatz (5.11) into the equations of motion (3.4)-(3.5) and linearizing the occurring equations in the perturbations leads to a homogeneous system of eight algebraic equations, which can be formulated as an eigenvalue problem in λ. It decouples into a symmetric ($\varepsilon_i^- = \varepsilon_i^+$, $\psi_i^- = \psi_i^+$, for $i = 1, 2$) and an antisymmetric ($\varepsilon_i^- = -\varepsilon_i^+$, $\psi_i^- = -\psi_i^+$, for $i = 1, 2$) part. This decoupling was also reported for vectorial Kerr cavities [81]. It originates from the invariance of the equations of motion (3.4)-(3.5) under the permutation of $+$ and $-$ fields. This symmetry will be broken directly by the TE-TM splitting in Eqs. (3.15)-(3.16). Therefore the eigenvalue problem arising in that case will not decouple and is thus much harder to tackle.

The separation of symmetric and antisymmetric modes simplifies the further analytical considerations significantly, since the 8-by-8 eigenvalue matrix decouples into two 4-by-4 matrices for the symmetric and the antisymmetric part, respectively, which can be treated independently. The matrix of the symmetric eigenvalue problem reads

$$
\begin{pmatrix}
-\gamma_c + i\widetilde{\Delta}_c & 0 & i & 0 \\
0 & -\gamma_c - i\widetilde{\Delta}_c & 0 & -i \\
i & 0 & -\gamma_0 + i\Delta_0 - 2i(1+\alpha)|\Psi_0|^2 & -i(1+\alpha)\Psi_0^2 \\
0 & -i & i(1+\alpha)\overline{\Psi}_0^2 & -\gamma_0 - i\Delta_0 + 2i(1+\alpha)|\Psi_0|^2
\end{pmatrix},
$$
$$(5.12)$$

where $\widetilde{\Delta}_c = \Delta_c - k_x^2 - k_y^2$. The asymmetric eigenvalue problem can be obtained by substituting Δ_c with $\widetilde{\Delta}_c$ in Eq. (5.8). Note, that the matrices in Eq. (5.8) and Eq. (5.12) differ only in the lower right quadrant which describes the exciton-exciton interaction. The implications of this difference will be discussed in the following section.

5.3.2. Growth rates

Both eigenvalue problems can now be solved independently. As long as the real part of all four eigenvalues is negative, the HS is stable with respect to the regarded perturbations. When the control parameter exceeds its critical value, at least one of these eigenvalues exhibits a positive real part for a certain $k = |\mathbf{k}|$. This quantity is denoted as *growth rate*. Here one has to distinguish between the growth rate $\Re\lambda_s(k, |\Psi_0|)$ for symmetric modes and $\Re\lambda_{as}(k, |\Psi_0|)$ for asymmetric ones. The maximum of these two growth rates
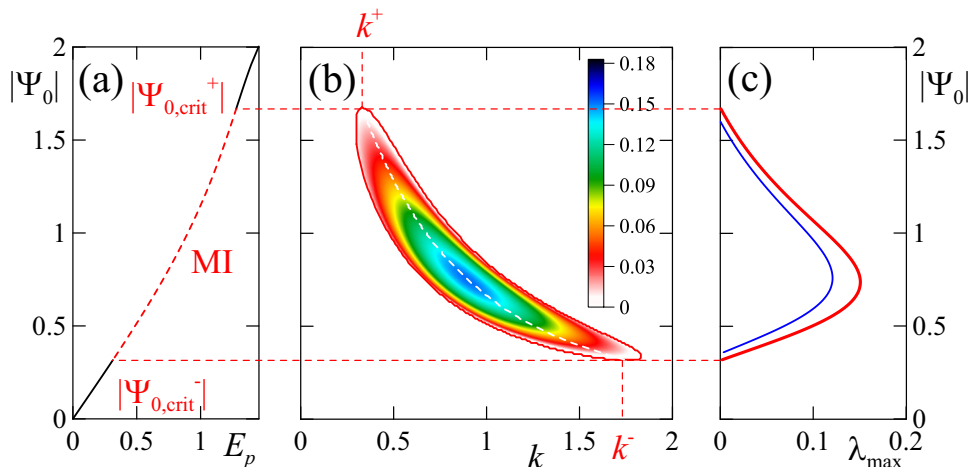
Figure 5.4: Modulation instability of the vectorial equations of motion (3.4)-(3.5) for $\alpha = 0.1$ and $\Delta = -0.1$: (a) HS branches $|\Psi^\pm|$ over the pump power E_p: stable symmetric HSs (bold black lines) and MI range (red dashed line); (b) growth rate $\Re\lambda(k, |\Psi_0|)$, boundary of instability range $\Re\lambda(k, |\Psi_0|) = 0$ (red line) and stable domain $\Re\lambda(k, |\Psi_0|) < 0$ (white area); (c) maximal growth rates $\Re\lambda_s(k, |\Psi_0|)$ and $\Re\lambda_{as}(k, |\Psi_0|)$ for a given order parameter $|\Psi_0|$ of symmetric (thin red) and antisymmetric (bold blue) perturbations, respectively; the dashed white line in (b) shows the position of $\Re\lambda_{max}(k, |\Psi_0|)$ in the k-$|\Psi_0|$ plane. Horizontal dashed lines denote the onset and the cessation of the modulational instability; $|\Psi_{0,crit}^\pm|$ and $k^\pm$ are calculated in Eqs. (5.14) and (5.16), respectively.

can be denoted as (global) growth rate $\Re\lambda(k, |\Psi_0|)$. Periodic solutions of Eqs. (3.4)-(3.5) are amplified, if their wave vector obeys the condition $\Re\lambda(k, |\Psi_0|) > 0$. This leads to the spontaneous formation of spatial patterns growing from a modulationally unstable HS.

For $\alpha > 0$, the growth rate of the symmetric modes always exceeds that of the asymmetric modes: $\Re\lambda_s(k, |\Psi_0|) > \Re\lambda_{as}(k, |\Psi_0|)$. This scenario is shown exemplarily for $\alpha = 0.1$ and $\Delta = -0.1$ in Fig. 5.4. For this detuning, the symmetric HSs are monostable, cf. Fig. 5.4(a). The growth rate $\Re\lambda(k, |\Psi_0|) = \Re\lambda_s(k, |\Psi_0|)$ is shown in Fig. 5.4(b). The branch of modulationally unstable HSs is denoted with a red dashed line in Fig. 5.4(a). For each value of the control parameter $|\Psi_0|$, there is a value of the wave vector k, where the growth rate takes its maximum $\Re\lambda_{max}$. The k value at $\Re\lambda_{max}$ determines the typical period of the arising pattern. We can see from Fig. 5.4(c), that the maxima of $\Re\lambda_s(k, |\Psi_0|)$ are larger than the maxima of $\Re\lambda_{as}(k, |\Psi_0|)$ for all values of $|\Psi_0|$. Therefore all arising patterns are expected to be governed by the dynamics arising from the symmetric modes. The spontaneous formation of patterns for this choice of parameters is studied in Subsec. 6.2.1.

Symmetric solutions emerge from the scalar solution by scaling all fields with $\sqrt{1 + \alpha}$. Thus, the growth rates for $\alpha = 0$ display the general form of a symmetric growth rate. After having already studied the case $\Delta = -0.1$, we want to highlight two special cases arising from different choices of the detunings.

Choosing $\Delta = -0.45$ leads to bistable symmetric HSs, cf. Fig. 5.5(a)-(b). In this case,
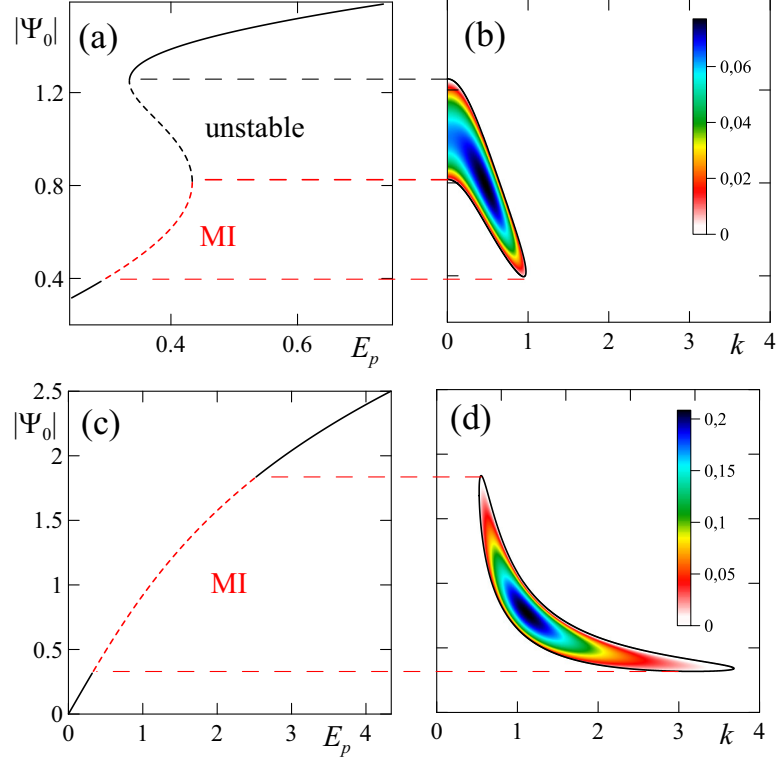
Figure 5.5: Modulation instability of the scalar equations of motion (2.13)-(2.14). Left column: HS branches for various detunings: stable HSs (solid black), unstable HSs (dashed black), MI range (red dashed); right column: instability growth rates $\mathrm{Re}\lambda(k, |\Psi|)$: boundary of instability - $\mathrm{Re}\lambda(k, |\Psi|) = 0$ (black lines); stable domains - $\mathrm{Re}\lambda(k, |\Psi|) < 0$ (white areas); 1st row:$\Delta = -0.45$; (a) the modulationally unstable pump range exceeds the bistability area, (b) at the critical intensity, only patterns within a small k range can be excited; 2nd row: $\Delta = 0.1$, (c) no bistability, wide MI pump range, (d) large excitable k range at critical intensity can lead to beating of various patterns.

there is an additional $|\Psi_0|$ - range where the HS destabilizes against perturbations with $k = 0$. It is widely believed that this does not lead to the formation of transverse patterns but rather to a spontaneous switching to the stable upper branch of the bistability loop and is therefore termed bistable frustration [79]. This range is indicated by a dashed black line in Fig. 5.5(a). Scalar pattern formation at these parameters is studied in Subsec. 6.1.1.

By choosing a detuning slightly above the excitonic resonance, e.g., $\Delta = 0.1$ as in Fig. 5.5(c)-(d) there is a wide range of excitable modes slightly above the onset of MI. Thus there will be a competition between different patterns. This case is shown in Fig. 6.8.

For $\alpha < 0$, the growth rate of the asymmetric modes always exceeds that of the symmetric modes: $\Re\lambda_{\mathrm{as}}(k, |\Psi_0|) > \Re\lambda_{\mathrm{s}}(k, |\Psi_0|)$. This scenario is shown exemplarily for $\alpha = -0.1$ with detunings $\Delta = -0.45$ in Fig. 5.6(a)-(c) and $\Delta = -0.1$ in Fig. 5.6(d)-(f). At first, the case $\Delta = -0.1$ will be studied, where the symmetric HSs are monostable. Figure 5.6(e) displays the growth rate $\Re\lambda(k, |\Psi_0|) = \Re\lambda_{\mathrm{as}}(k, |\Psi_0|)$. The branch of modulationally unstable HSs is shown by a blue dashed line in Fig. 5.6(d). For each value of the control
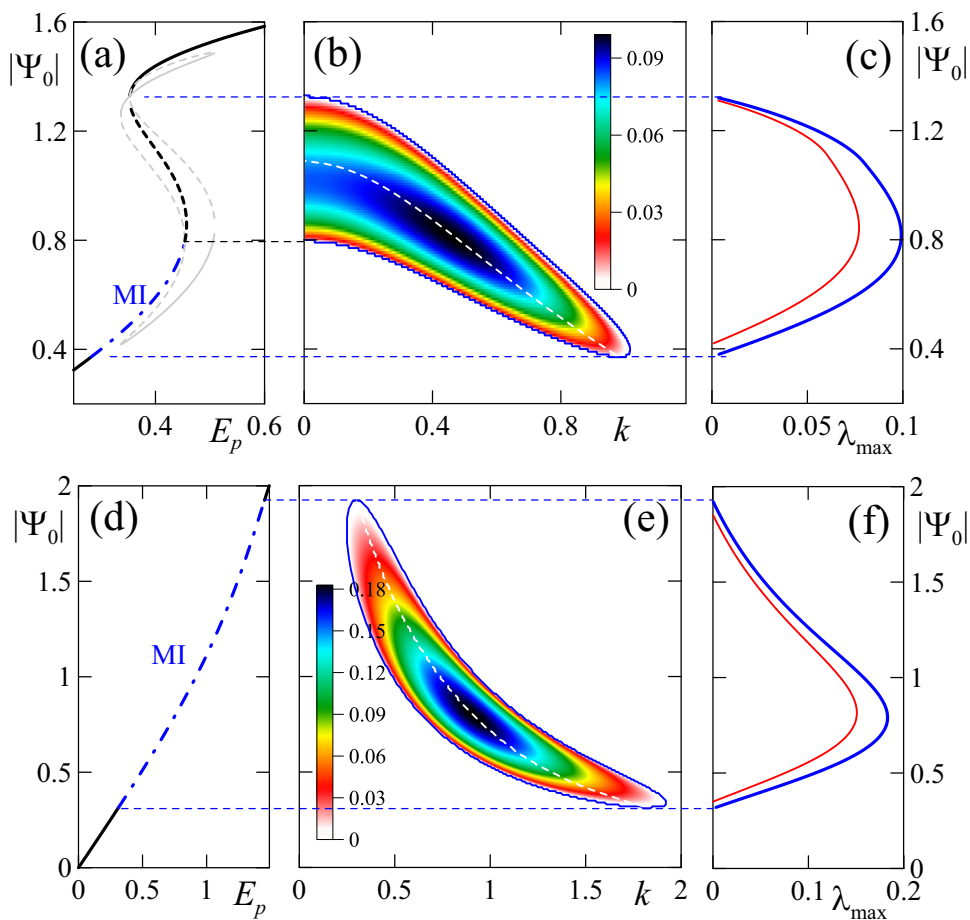
Figure 5.6: Modulation instability of the vectorial equations of motion (3.4)-(3.5) for $\alpha = -0.1$: (a)-(c) Analysis of homogeneous solutions (HSs) with $\Delta = -0.45$: (a) HS branches $|\Psi^{\pm}|$ over the pump power E_p: symmetric HSs (bold black), asymmetric HSs (thin grey) and MI range (blue chain line); continuous lines denote stable solutions, whereas dashed lines stand for unstable HSs; (b) growth rate $\Re\lambda(k, |\Psi_0|)$, boundary of instability range $\Re\lambda(k, |\Psi_0|) = 0$ (blue line) and stable domain $\Re\lambda(k, |\Psi_0|) < 0$ (white area); (c) maximal growth rates $\Re\lambda_s(k, |\Psi_0|)$ and $\Re\lambda_{as}(k, |\Psi_0|)$ for a given order parameter $|\Psi_0|$ of symmetric (thin red) and antisymmetric (bold blue) perturbations, respectively; the dashed white line in (b) shows the position of $\Re\lambda_{max}(k, |\Psi_0|)$ in the k-$|\Psi_0|$ plane. Horizontal dashed lines denote the onset and the cessation of the modulational instability; (d)-(f) show the respective figures with $\Delta = -0.1$.

parameter $|\Psi_0|$, there is a value of the wave vector k, where the growth rate takes its maximum $\Re\lambda_{max}$. The k value at $\Re\lambda_{max}$ determines the typical period of the arising pattern. In Fig. 5.6(f) we show that the maxima of $\Re\lambda_{as}(k, |\Psi_0|)$ are larger than that of $\Re\lambda_s(k, |\Psi_0|)$ for all values of $|\Psi_0|$. Therefore all arising patterns are expected to be governed by the dynamics arising from the antisymmetric modes.

Figure 5.6(a)-(c) shows $\Re\lambda(k, |\Psi_0|)$ for $\Delta = -0.45$. Like in the scalar case, there is a $|\Psi_0|$ range where the HS destabilizes against perturbations with $k = 0$, cf. the dashed black line in 5.6(a). The formation of vectorial patterns in this parameter range will be discussed in Subsec. 6.2.2 with the help of Fig. 6.13. Vectorial effects in the deep bistable regime $\Delta = -0.7$ shall be studied in Subsec. 6.2.3.

5.3.3. Analysis at the critical intensity

One can conclude, that for $\alpha < 0$ ($\alpha > 0$) there is a critical $|\Psi_0|$ range, where preferably asymmetric (symmetric) modes are amplified. In the following, analytical expressions for the respective critical quantities will be derived. For symmetric perturbations, the critical intensity[d] $I_{0,\mathrm{crit,s}}^{\pm}$ at the Turing instability points amounts to

$$I_{0,\mathrm{crit,s}}^{\pm} = \frac{1 + 4\gamma_c\Delta_0 \pm \sqrt{1 - 4\gamma_c(3\gamma_0\left(1 + \gamma_0\gamma_c\right) - \Delta_0(2 + \gamma_c\Delta_0))}}{6\gamma_c(1 + \alpha)}, \qquad (5.13)$$

whereas for antisymmetric perturbations we get

$$I_{0,\mathrm{crit,as}}^{\pm} = \frac{1 - \alpha + 4\gamma_c\Delta_0 \pm \sqrt{\left(1 - \alpha + 4\gamma_c\Delta_0\right)^2 - 4(3 - \alpha)(1 + \alpha)\gamma_c\left(\gamma_0 + \gamma_0^2\gamma_c + \gamma_c\Delta_0^2\right)}}{2(3 - \alpha)(1 + \alpha)\gamma_c}.$$
$$(5.14)$$

The wavevectors of the symmetric perturbations at their bifurcation point fulfill the relation

$$\left(k_{\mathrm{s}}^{\pm}\right)^2 = \Delta_c + \frac{1 + 2\gamma_0\gamma_c \mp \sqrt{1 - 4\gamma_c(3\gamma_0\left(1 + \gamma_0\gamma_c\right) - \Delta_0(2 + \gamma_c\Delta_0))}}{2(2\gamma_0 - \Delta_0)}, \qquad (5.15)$$

whereas for antisymmetric perturbations at the respective bifurcation point they read

$$\left(k_{\mathrm{as}}^{\pm}\right)^2 = \Delta_c + \frac{(1 - \alpha)(1 + 2\gamma_0\gamma_c) \mp \sqrt{(1 - \alpha + 4\gamma_c\Delta_0)^2 - 4(3 - \alpha)(1 + \alpha)\gamma_c(\gamma_0 + \gamma_0^2\gamma_c + \gamma_c\Delta_0^2)}}{4\gamma_0 - 2(1 - \alpha)\Delta_0}.$$
$$(5.16)$$

Equations (5.13) and (5.14) are only valid if $(k_{\mathrm{s}}^{\pm})^2 \geq 0$ and $(k_{\mathrm{as}}^{\pm})^2 \geq 0$, respectively. For detunings which would lead to $(k_{\mathrm{s}}^{\pm})^2 < 0$ ($(k_{\mathrm{as}}^{\pm})^2 < 0$), we have to set $(k_{\mathrm{s}}^{\pm})^2 = 0$ ($(k_{\mathrm{as}}^{\pm})^2 = 0$). Then the critical intensity $I_{k=0,\mathrm{crit,as}}^{+}$ at the upper bifurcation point is identical to I_0^{+} in Eq. (5.9) in case of antisymmetric perturbations. In case of symmetric perturbations, the critical intensity reads

$$I_{k=0,\mathrm{crit,s}}^{+} = \frac{-2\mathcal{B} + \sqrt{\mathcal{B}^2 - 3\mathcal{A}^2}}{3(1 + \alpha)}, \qquad (5.17)$$

with $\mathcal{A}$ and $\mathcal{B}$ as in Eq. (5.9). It should be noted that both $I_{k=0,\mathrm{crit,s}}^{+}$ and $I_{k=0,\mathrm{crit,as}}^{+}$ depend on Δ_c, whereas $I_{0,\mathrm{crit,s}}^{\pm}$ and $I_{0,\mathrm{crit,as}}^{\pm}$ do not. This stunning fact can be explained by taking a closer look on the derivation of the critical values for $k \neq 0$. The transverse wave vector and the cavity detuning appear only in the combination $\tilde{\Delta}_c = \Delta_c - k^2$. This suggests the interpretation that the detuning from the cavity resonance is compensated by the nonzero

---

[d]It should be mentioned that throughout this section, all intensities $I_0 = |\Psi_0|^2$ refer to the excitonic component of the intensity. Furthermore, it is important to note, that in Eqs. (5.13)-(5.16), the $-/+$ signs do not refer to the exciton spin but to the lower and upper destabilization point of the HSs, respectively.

wave vector of the arising patterns [79]. Thus these critical intensities do not depend on the effective quantity $\tilde{\Delta}_c$ at all. $I^+_{k=0,\mathrm{crit,s}}$ is the (scaled) upper boundary of the bistable symmetric HS. On the other side, $I^+_{k=0,\mathrm{crit,as}}$ exceeds this range for $\alpha < 0$, as can be seen in Fig. 5.7(b). This is due to the destabilization of symmetric HSs in favor of asymmetric HSs.
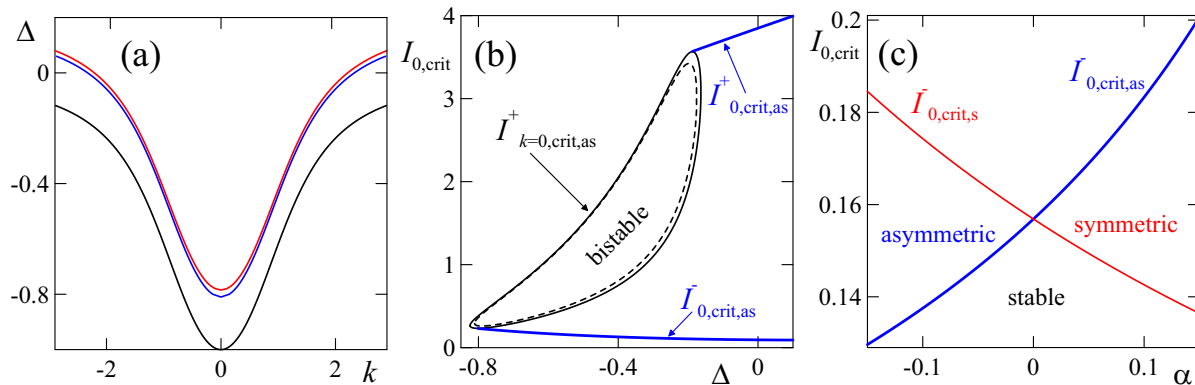

Figure 5.7: Results of the perturbation analysis of homogeneous solutions: (a) Lower branch of the linear polariton dispersion relation (black), wave vector ($k^{\pm}_{\mathrm{s}}$) of the perturbations at the critical intensity $I^{\pm}_{0,\mathrm{crit,s}}$ as a function of the detuning Δ (red) and ($k^{\pm}_{\mathrm{as}}$) of the periodic perturbation at the critical intensity $I^{\pm}_{0,\mathrm{crit,sa}}$ as a function of the detuning Δ (blue); (b) intensity $I^-_{0,\mathrm{crit,as}}$ at the lower bifurcation point and $I^+_{0,\mathrm{crit,as}}$ at the upper bifurcation point as a function of the detuning Δ for $\alpha = -0.1$ (bold blue lines); within the region encircled by the thin solid black curve also perturbations with $k = 0$ are unstable; the dashed black lines frame the range between the turning points of the bistability loop for symmetric HSs; (c) critical intensity for symmetric (thin red) and antisymmetric perturbations (bold blue) as a function of α for $\Delta_0 = -0.45$.

The main results of the above analysis are illustrated in Fig. 5.7. The curve of expected wave vectors of the patterns lies well above the branch of the linear dispersion relation, cf. Fig. 5.7(a). Since the former was derived from the full nonlinear equations, it can be interpreted as a dispersion relation with nonlinear blueshift. The implicit expression $\Delta(k^-)$ is represented by the red (blue) line for symmetric (antisymmetric) perturbations in Fig.5.7(a). However, it should be noted, that the perturbation analysis is only valid close to HSs. The horizontal asymptote of the lower branch of the nonlinear dispersion relation lies at $\Delta_0 = 2\gamma_0$ ($\Delta_0 = 2\gamma_0/(1 - \alpha)$), which is $\Delta = 0.2$ ($\Delta = 0.2222$) for our choice of the damping constants and $\alpha = -0.1$. Its minimum lies at $\Delta = -0.78462$ ($\Delta = -0.809945$). Thus, no patterns are expected below these detunings. The full analytical expression for these minima is very cumbersome and therefore not included here.

Figure 5.7(b) displays the full instability landscape for negative α. The intensity range between the inflection points of the bistability loop for symmetric HSs is framed by the dashed black contour. It is included in the range of symmetric HSs being unstable with respect to uniform perturbations which is calculated from Eq. (5.9) and depicted by a solid black contour. The bold blue lines denote the critical intensities $I^{\pm}_{0,\mathrm{crit,as}}$ according

to Eq. (5.14) in their existence range.

In Fig. 5.7(c), we plotted the critical intensity $I_{0,\mathrm{crit}}^-$ over α at $\Delta_0 = -0.45$ for both symmetric and antisymmetric perturbations. It can be seen that for $\alpha > 0$ the MI point for symmetric perturbations lies at a smaller pump power than that of the antisymmetric perturbations. This means, that the arising patterns can be expected to be symmetric $(\rho_E(x,y) \equiv 0)$ and each polarization is similar to the scalar hexagonal patterns from Ref. [163]. For $\alpha < 0$, however, the bifurcation point for antisymmetric perturbations lies at a smaller pump power than that for the symmetric ones. In Sec. 7.2, we will prove for dark solitons that these antisymmetric dynamics are reflected in a spatial effect, namely in the spatial separation of the two vector solitons formed in $+$ and $-$ polarization [165]. For hexagonal patterns, this spatial breakup is also expected to appear in the form of two spatially shifted $+$ and $-$ patterns. The polarization degree $\rho_E(x,y)$ is then also nontrivial [164].

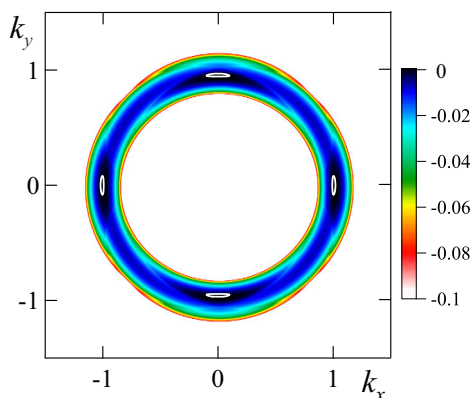### 5.3.4. Perturbation theory for the spin-dependent case with TE-TM splitting

Figure 5.8: Growth rate $\Re\lambda(k_x, k_y)$ at $|\Psi_0| = 0.37181$, corresponding to $E_p = 0.282$; the closed white curves denote $\Re\lambda(k_x, k_y) = 0$; parameters are chosen $\Delta = -0.45$, $\alpha = -0.1$ and $\beta = 0.05$.

Additionally taking into account the TE-TM splitting contribution in the equations of motion changes the nature of the perturbation scheme drastically. Since the term proportional to β breaks the pseudospin symmetry of the system directly, the above mentioned splitting of the eigenvalue problem into a symmetric and an antisymmetric part is no longer possible. Thus, the arising characteristic equation is of 8th order and does no longer exhibit feasible roots. Therefore, the growth rates have to be determined numerically. Since the isotropy in k_x-k_y plane is broken by the TE-TM splitting, the growth rates will depend not only on $k^2 = k_x^2 + k_y^2$ but on the very components k_x and k_y thus showing a direction dependence in the transverse momentum plane. This is shown

exemplarily in Fig. 5.8 for $\Delta = -0.45$, $\alpha = -0.1$, and $\beta = 0.05$. A pump power of $E_p = 0.282$ leads to $|\Psi_0| = 0.37181$ for the HSs. The occurrence of a spatial anisotropy for the stimulated amplification of polaritons in a perfectly isotropic microcavity was also observed in Ref. [178]. This spontaneous breaking of the isotropy was explained by the combination of the TE-TM cavity-mode splitting and the spin-dependent polariton-polariton scattering processes. In the framework of hexagonal pattern formation, the interplay of these two effects will lead to a spontaneous movement of the entire pattern, cf. Ref. [179] and Sec. 6.3. The anisotropy arising from the TE-TM polarization splitting can be used to generate optical beams carrying orbital angular momentum [180].

5.4. Chapter summary and concluding remarks

In this chapter, both the linear and nonlinear properties of homogeneous solutions of the equations of motion derived in Chapts. 2 and 3 were investigated.

The linear dispersion relation of spinless exciton-polaritons consists of two distinct branches. The nonlinearity causes a blueshift of both branches, which we calculated for spatially periodic perturbations at their bifurcation point. The TE-TM splitting between the cavity modes is inherited by the linear dispersion relation. Whereas the splitting of the photon-like upper polariton branch increases with the wave vector k, the splitting of the lower polariton branch vanishes for both $k = 0$ and $k \to \infty$ and approaches its maximum in between. It is important to note that the splitting of both branches is isotropic in the transverse plane despite originating from an anisotropic effect.

For appropriate choice of the detunings, the symmetric HSs show a bistable dependence on the pump power. We calculate a critical value for α, where asymmetric HSs bifurcate from these symmetric HSs. Together they form a set of multistable HSs, which is a typical feature of nonlinear systems with spin.

Both symmetric and asymmetric HSs can destabilize in favor of spatially periodic solutions. In our analysis we focused on periodic solutions nesting on a symmetric HS background. The structure of the perturbation scheme and its solutions depends crucially on the question whether one includes TE-TM splitting or not. Without TE-TM splitting, the problem exhibits a discrete spin symmetry and therefore decomposes into a symmetric and an asymmetric part. Whereas the symmetric part corresponds to the scalar problem, the asymmetric part can predict the spontaneous symmetry breaking linked with $\alpha < 0$. Both regimes will be discussed extensively in the following chapters. By including TE-TM splitting, however, the spin symmetry of the equations of motion is broken directly. Furthermore, it causes an anisotropy in the transverse momentum plane.

6. Dynamics of extended structures

The formation of spatially periodic patterns out of a thermodynamical equilibrium is a universal phenomenon in many nonlinear systems. It has therefore been a subject of vigorous scientific efforts in various areas of research such as convection processes, solid state physics, chemical reaction dynamics, nonlinear optics, and various self-assembled biological systems [7–11, 181]. Patterns can arise spontaneously when the interplay between nonlinearity and a cross-talk mechanism at different sites (e.g. diffraction or diffusion) destabilizes a spatially uniform field distribution. With the help of methods of nonlinear dynamics as described in Sec. 4.2 and performed in Sec. 5.3, one gets an analytical approach to the nature of this destabilization process and the bifurcation dynamics of the arising patterns.

The aforementioned requirements are met in many nonlinear optical systems, such as nonlinear media with counter-propagating waves [62–64] or other passive and active nonlinear optical systems [65–71]. The most investigated systems in optical pattern formation, however, are cavities filled with a nonlinear medium [72–84]. Besides being of own interest, the study of nonlinear optical cavities (especially with Kerr nonlinearity) is an important prerequisite for the investigation of polaritons in a cavity [29, 30, 163, 164, 179, 182], since these two systems share several features. The feedback introduced by the cavity (cf. Sec. 2.1) enhances nonlinear effects leading to a competition between several unstable modes. Furthermore, the losses due to the mirrors introduce dissipation which has to be compensated by an external pump. Another important requirement for the spatial instability leading to transverse patterns is the existence of a detuning between the frequency of the driving field and the cavity resonance. The emission of certain periodic patterns is then favored, since the detuning is compensated by their wave vector, cf. the passage after Eq. (5.17) in Subsec. 5.3.3. It has been shown, that vectorial effects which naturally arise if one takes into account the polarization of light, can lead to additional different structures including stripes and labyrinthine patterns. But the most common type of patterns is of hexagonal type. The competition of various patterns and pattern selection was addressed in Refs. [65, 79] in the framework of a passive Kerr cavity driven in the bistable regime. Using a weakly nonlinear theory, hexagonal patterns were proven to be the most stable ones in the vicinity of the Turing instability point. This statement is valid beyond that special case. For subcritically bifurcating hexagonal patterns in the Lugiato-Lefever regime, they will have a finite amplitude even at the threshold pump

power.

The conditions for spontaneous pattern formation were derived in Sec. 5.3. Based on this analysis we organize this chapter as follows: In Sec. 6.1 the scalar model is analyzed according to our publication [163]. Special emphasis is placed on the influence of the detunings on the shape and the existence range of patterns. In Sec. 6.2 we additionally take into account the exciton spin. The most important parameter is then naturally the cross-phase modulation parameter α, since it is responsible for the spatial shift between the two polarizations. These results have been presented in our paper [164]. In Sec. 6.3 the influence of the TE-TM splitting on the vectorial patterns will be discussed according to our publication [179].

6.1. Scalar polariton patterns

The formation of spatial patterns in dissipative nonlinear optical systems has been a topic of vigorous interest since the introduction of a paradigmatic model [72] by Lugiato and Lefever in 1987. Since then, the Kerr cavity has become by far the most studied model for pattern formation in nonlinear optics [78–84]. Besides its experimental relevance, the scalar Kerr cavity is of special theoretical importance, since its structure is comparably easy and therefore it allows for an extensive analysis of the destabilization of HSs. This analysis contains both the destabilization in favor of spatially periodic perturbations analog to Sec. 5.3 and amplitude equations adapted to the expected shape of the final patterns. Depending on the relative sign between the diffraction term and the nonlinearity one distinguishes between focussing and defocussing nonlinearity. The nature of this nonlinearity substantially influences the pattern formation process. Actually it was claimed from analytical calculations that there is no pattern formation in a defocussing Kerr cavity, since it is frustrated by bistable switching [79]. In the self-focussing case, however, subcritically bifurcating hexagonal patterns are predicted by the nonlinear analysis [78, 79].

Moreover, studying Kerr cavities is an important prerequisite for the investigation of pattern formation in a polaritonic cavity. Due to the strong coupling, exciton-polaritons provide a much richer range of dynamical regimes which is expressed in the characteristic shape of the dispersion relation. The effective dispersion relation at the operating point strongly depends on the chosen detuning of the pump frequency from the excitonic resonance. In our studies, we will always restrict ourselves to the lower polariton branch and disregard the photon-like upper polariton branch. The crucial parameter to address the different parts of the lower polariton branch is the detuning. We know from Eq. (5.15) (cf.

also Fig. 5.7) that scalar pattern formation is in principle possible for $-0.78462 < \Delta < 0.2$. Near the bottom of the lower polariton branch the dispersion relation is almost perfectly parabolic and therefore the arising patterns are expected to resemble those of the Kerr cavity. Increasing the detuning towards the excitonic resonance should alter the properties of these patterns. After crossing this resonance they are expected to break up. These three regimes will be investigated in this section.

Since the governing equations are much more complicated than in the case of the Kerr cavity, the stability analysis turns out to be more challenging, cf. Sec. 5.3. Thus it is necessary to study certain properties of the patterns via extensive numerical parameter scans using the methods presented in Sec. 4.2.

6.1.1. Pattern formation near the bottom of the lower polariton branch

Near the bottom of the lower polariton branch, the influence of the upper polariton branch is negligible and the effective polariton dispersion relation is almost parabolic. Therefore, the dynamics is expected to be of the Lugiato-Lefever type [72] with a defocussing Kerr nonlinearity. Characteristic for this type is the bistable dependence of the HSs on the external pump power. We can see from Eq. 5.7 that the scalar equations of motion (2.13)-(2.14) exhibit bistable HSs for $-0.79516 < \Delta < -0.18994$. It was claimed [79], that bistable switching would frustrate pattern formation for a self-defocussing medium. In the following we will find counterexamples proving this general statement wrong for polaritonic cavities.

The width of the modulationally unstable pump range depends strongly on the detuning Δ. This can be derived from Eq. (5.13). Figure 5.7(b) shows the dependence of the MI range on the detuning only for antisymmetric perturbations and $\alpha = -0.1$, but the case discussed here is actually very similar. We see that near the bottom of the lower polariton branch the MI range is rather small and lies totally within the bistability loop, cf. also Ref. [170]. Therefore, the formation of a stable spatial pattern is frustrated, since it immediately switches to the stable upper branch of the bistability curve.

For $\Delta = -0.55$ the MI point lies still within the bistability loop, cf. Fig. 6.1(a). Nevertheless, it is possible to observe the formation of a stable hexagonal pattern, cf. Fig. 6.1(b). Since the dispersion relation can still be regarded as parabola-like for $\Delta = -0.55$, it is not surprising, that the dynamics of the pattern formation has characteristics of the Lugiato-Lefever model. The corresponding branch $\max |\Psi(x,y)|$ is shown in Fig. 6.1(a). It bifurcates subcritically at the MI point which is in accordance with general statements
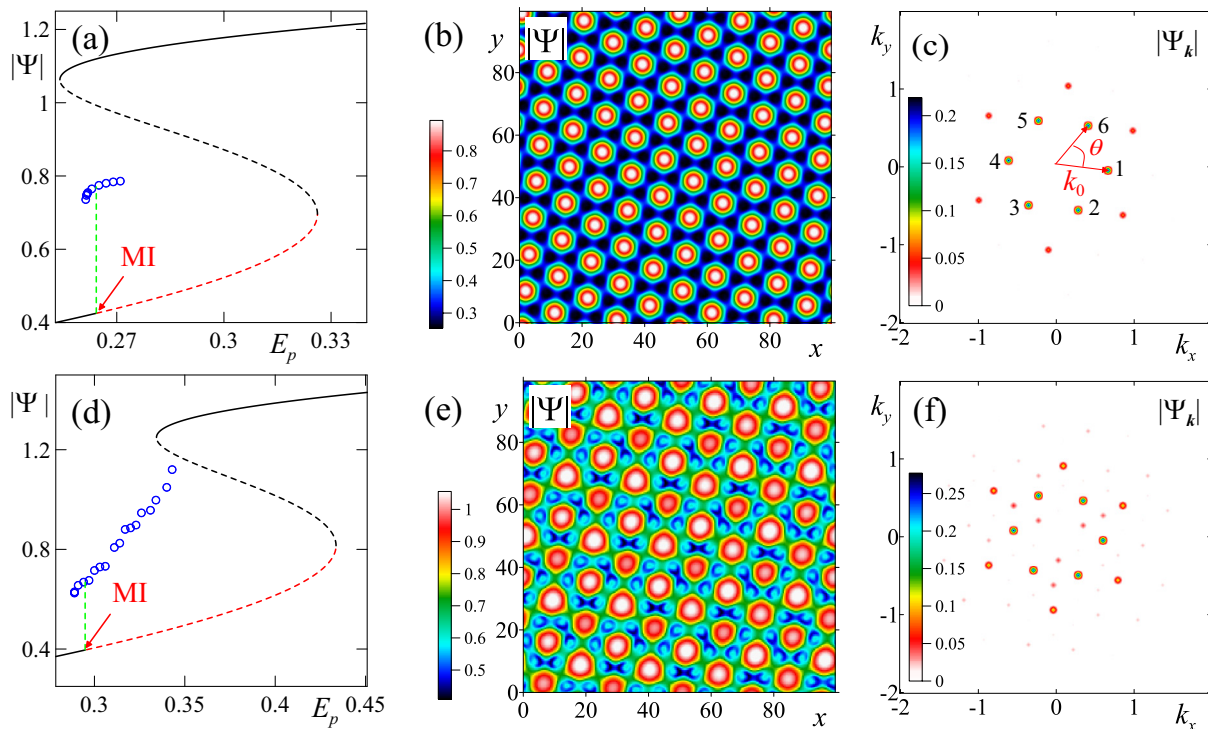
Figure 6.1: Formation of hexagonal patterns in the bistability domain: (a) $|\Psi|$ of stable HSs (solid black), unstable HSs (dashed black), modulationally unstable HSs (dashed red line), and $\max |\Psi(x,y)|$ of the hexagonal pattern (blue dots) versus the pump power E_p for $\Delta = -0.55$, (b) $|\Psi(x,y)|$ of perfect hexagonal pattern for $\Delta = -0.55$ and $E_p = 0.265$, (c) Fourier transformation $|\Psi_\mathbf{k}|$ of (b) normalized to omitted HS background, k_0 denotes the modulus of the Fourier components of the hexagonal pattern and θ is the angle of the Fourier component with respect to the distinguished Fourier component denoted by 1; (d)-(f) show the respective results for $\Delta = -0.45$ and $E_p = 0.341$.

proven for the Kerr cavity [78, 79]. Its stability range extends from about $E_p = 0.261$ to 0.272 and is therefore rather small compared with the cases that will be regarded below. Above $E_p = 0.272$ the arising pattern enters the attraction range of the unstable HS and thus switches to the stable upper branch of the bistability loop. The Fourier components of this pattern are shown in Fig. 6.1(c). Naturally, the strongest Fourier component stems from the DC background at $k_x = k_y = 0$. However, in order to improve the visibility of the other nontrivial Fourier components, we omitted the DC component in all figures showing Fourier images in this section. Nevertheless, the strength of the zeroth Fourier component is included indirectly, since all other peaks are normalized to its amplitude. Due to the perfect hexagonal structure of the pattern in Fig. 6.1(b), the first-order Fourier components are also arranged in a perfect hexagon[a]. The second order Fourier components arise naturally from four-wave mixing processes imprinted by the third-order nonlinearity. They are about one order of magnitude weaker and also arranged in a perfect hexagon.

---

[a] For further convenience, they are enumerated 1-6. This convention will be revisited in Sec. 6.3, where the influence of TE-TM splitting on the position of these six Fourier components is studied. In the framework of these studies, k_0 and the angle θ will also be needed.

For $\Delta > -0.52012$, the MI onset is left to the bistable pump range, cf. Fig. 5.7(b). Therefore, the formation of spatial patterns is no longer subjected to switching processes to the upper branch of the bistability loop. Once again, the arising stable patterns show perfect hexagonal structure and bifurcate subcritically, shown exemplarily for $\Delta = -0.45$ in Fig. 6.1(d). It is notable, that their stability range is substantially increased compared with that for $\Delta = -0.55$.

Apart from their stability range, the other main difference between the hexagonal patterns for $\Delta = -0.55$ and $\Delta = -0.45$ is their lattice spacing near the MI point. It decreases with increasing Δ, since the nonlinear dispersion relation gets broader in k space. This tendency was predicted in Eq. (5.15) and could also be deduced from the shape of the linear dispersion relation which gets wider if one increases Δ toward the excitonic resonance, cf. Fig. 5.7(a).

By increasing the pump field, more power can be added to the system. For $\Delta = -0.55$, this lead straightforwardly to a switching to the upper branch of the bistability loop. For $\Delta = -0.45$, however, the patterns have a wider stability range. An example is shown in Fig. 6.1(e) where the coupling between adjacent peaks is enhanced which leads to a spontaneous symmetry breaking of the amplitude of hitherto undistinguishable peaks. The occurrence of these periodical defects was described for the prototypical model of a self-focussing Kerr cavity in Ref. [84]. Analyzing the Fourier transformation of the pattern sheds further light on the origin of the defects. Whereas in case of a perfect hexagonal pattern, all Fourier orders form perfect hexagons, this symmetry is clearly broken in Fig. 6.1(f). This Fourier profile exhibits a remarkable triangular symmetry which can be seen best by looking at the triangle inside the hexagon spanned by the main Fourier orders.

For $\Delta < -0.55$ the stability range of the hexagonal patterns shrinks further and finally vanishes. Our simulations reveal this threshold to lie between $\Delta = -0.55$ and $\Delta = -0.6$. Thus it is not possible to exhaust the range of detunings down to $\Delta = -0.78462$. However, we will show in Subsec. 6.2.3 that there is another effect linked to the existence of stable dark solitons, which allows to circumvent the bistable frustration of pattern formation also for $\Delta < -0.6$ in the vectorial case with $\alpha < 0$.

6.1.2. Pattern formation beyond the parabolic approximation

By increasing the pump frequency towards the excitonic resonance, the influence of the upper polariton branch can no longer be neglected. Also the approximation of the parabolic dispersion relation is not valid any more. Regarding pattern formation, the crucial difference in comparison to the Lugiato-Lefever model, is the absence of bistability.

This opens the gate for the observation of pattern formation over the entire modulationally unstable pump range.
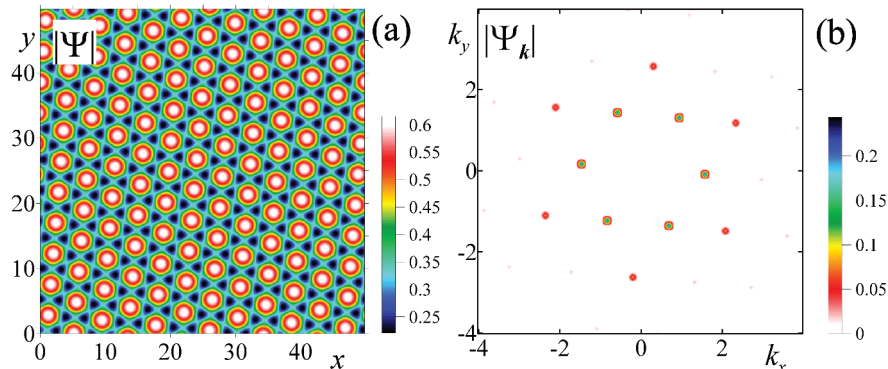

Figure 6.2: (a) perfect hexagonal pattern $|\Psi(x,y)|$ for $\Delta = -0.1$ and $E_p = 0.35$; (b) Fourier transformation $|\Psi_{\mathbf{k}}|$ of (a) normalized to omitted HS background.

For $\Delta > -0.18994$, the output intensity depends uniquely on the input power. This property originates from the influence of the upper branch polaritons and distinguishes cavity polaritons from the Lugiato-Lefever model. We have derived two values $I_{0,\text{crit,s}}^{\pm}$ for the critical intensity of the Turing instability, cf. Eq. (5.13). For the bistable case, however, the upper value $I_{0,\text{crit,s}}^{+}$ always lies within the unstable range and therefore the excitation of stable patterns in its vicinity is not possible. On the other hand, if one chooses, e.g., $\Delta = -0.1$, it should be possible to observe the formation of regular patterns both near $I_{0,\text{crit,s}}^{-}$ and $I_{0,\text{crit,s}}^{+}$. The results of these simulations are shown Figs. 6.2-6.6 and summarized in Fig. 6.7.
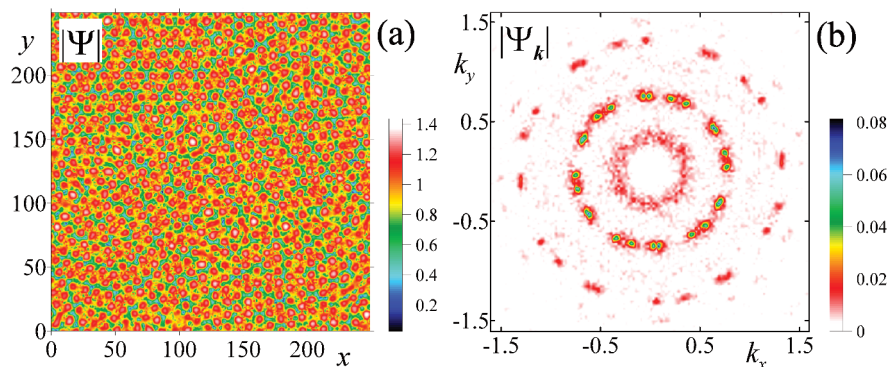

Figure 6.3: (a) Formation of domains without long-range order for $\Delta = -0.1$ and $E_p = 0.7$; (b) Fourier transformation $|\Psi_{\mathbf{k}}|$ of (a) normalized to omitted HS background.

Near $I_{0,\text{crit,s}}^{-}$, the range of excitable wave vectors at the bifurcation points is rather point-like, cf. Fig. 5.4(b). The excited pattern reflects this property perfectly and is thus perfectly hexagonal, cf. Fig. 6.2. The argument made at $\Delta = -0.55$ also applies here, cf. Fig. 6.1(b)-(c).
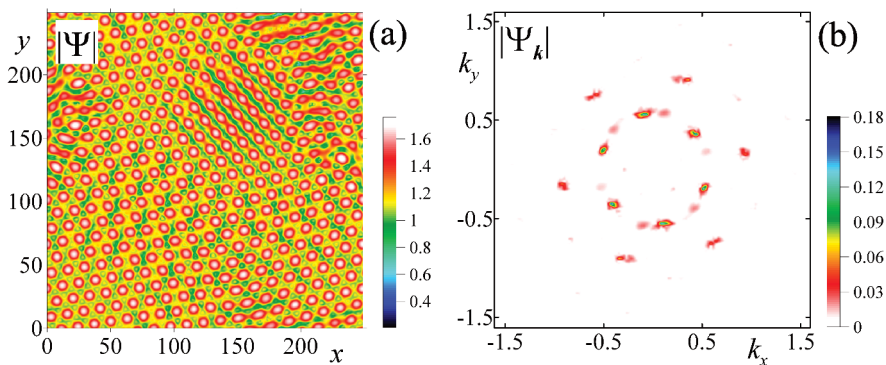
Figure 6.4: (a) transition from domains to labyrinthine structure for $\Delta = -0.1$ and $E_p = 0.9$; (b) Fourier transformation $|\Psi_{\mathbf{k}}|$ of (a) normalized to omitted HS background.

Increasing the pump power causes distortions of the formerly perfect hexagonal pattern. In contrast to the cases discussed before, the distorted patterns arising for $\Delta = -0.1$ are not subjected to bistable frustration. Thus, it is possible to further increase the pump which leads to the emergence of more imperfections and eventually to the formation of several domains, cf. Fig. 6.3(a). Whereas the hexagonal short-range order within a domain is still preserved, there is no long-range order between different domains. This is a fundamental difference to the slightly distorted patterns presented in Fig. 6.1. The Fourier spectrum in Fig. 6.3(b) confirms these findings: The main Fourier modes are no longer arranged in a perfect hexagon. However, they are still situated within a ring with a well-defined distance from the origin. Actually counting them leads to a number of 24 Fourier modes. We can interpret this as a coexistence of four patterns with different inclinations in the x-y plane.
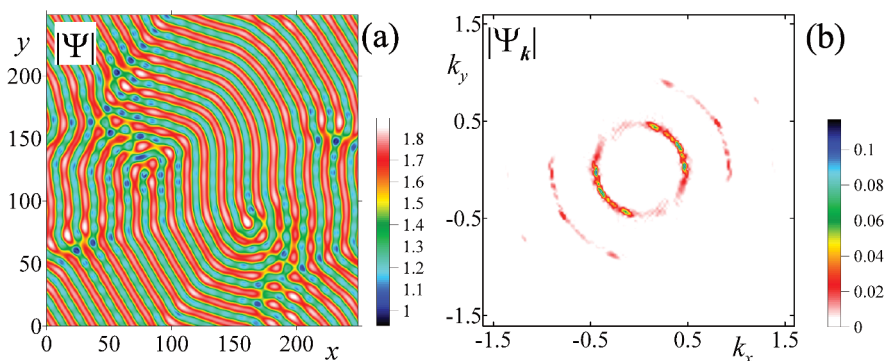

Figure 6.5: (a) labyrinthine pattern for $\Delta = -0.1$ and $E_p = 1.1$; (b) Fourier transformation $|\Psi_{\mathbf{k}}|$ of (a) normalized to omitted HS background.

By further increasing the pump power, the number of main Fourier orders is reduced to six again, cf. Fig. 6.4(b). However, their arrangement strongly deviates from a perfect hexagon. In the actual pattern in Fig. 6.4(a), this fact is represented by imprinting a predominant direction.

This development consequently leads to the formation of a labyrinthine stripe pattern, cf. Fig. 6.5(a). This pattern exhibits several interesting features the most striking being the absence of two-dimensional spots. Instead, the underlying structure rather consists of roll patterns which are disturbed by several dislocations and arches [66, 69]. The Fourier profile is basically dominated by two competing pairs of main Fourier peaks.
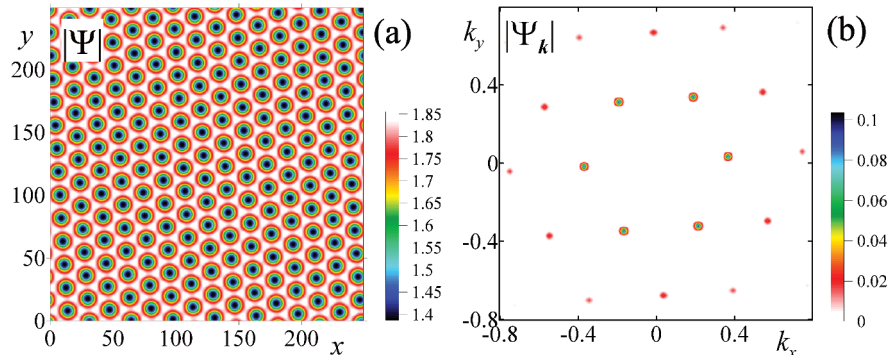

Figure 6.6: (a)perfect honeycomb pattern for $\Delta = -0.1$ and $E_p = 1.3$; (b) Fourier transformation $|\Psi_\mathbf{k}|$ of (a) normalized to omitted HS background.

Near $I_{0,\mathrm{crit,s}}^+$, a perfect honeycomb pattern occurs, cf. Fig. 6.6(a). It can be interpreted as an inverted hexagonal pattern. Returning to a structure with high symmetry was suggested by the instability growth rate depicted in Fig. 5.4(b), which becomes again point-like in the vicinity of $I_{0,\mathrm{crit,s}}^+$. The Fourier profile in Fig. 6.6(b) again consists of six spots arranged in a perfect hexagon. Their peak amplitude amounts about 10 % of the amplitude of the HS peak. This is considerably smaller than the 25 % reached for $E_p = 0.35$ and reflects the fact, that the honeycomb pattern is formed by dips nesting on a comparably high HS background.
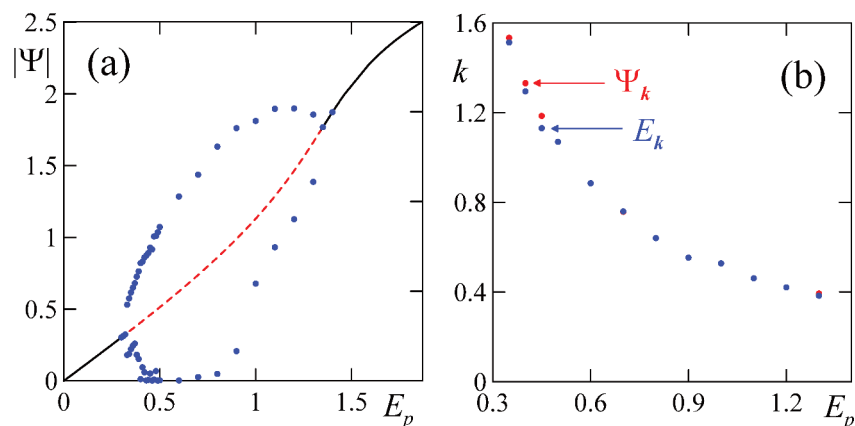

Figure 6.7: (a) stable HSs (bold black lines), modulationally unstable HSs (dashed red lines), $\max|\Psi(x,y)|$ and $\min|\Psi(x,y)|$ of the arising patterns (blue dots) over the pump power, (b) wave number $k = \sqrt{k_x^2 + k_y^2}$ of the strongest Fourier mode over the pump power.

In Fig. 6.7(a) we depicted $\max|\Psi(x,y)|$ and $\min|\Psi(x,y)|$ of all these patterns showing

thereby that the predicted direct link between $I_{0,\text{crit,s}}^{-}$ and $I_{0,\text{crit,s}}^{+}$ from Eq. (5.13) exists. We note, however, that a line connecting the blue dots in Fig. 6.7(a) cannot be interpreted as a genuine branch, but only connects the maxima and minima of the different patterns at their respective pump powers. The actual branches would obey a more complicated bifurcation scheme and are not included in this work, since the main objective of this analysis consists in showing that the various stable patterns cover an extraordinarily wide pump range. The investigated polaritonic system therefore turns out to provide a more robust environment for the formation of stable patterns in a wide pump range than the Kerr cavity, where an early transition to optical turbulence is reported [83]. Another remarkable fact is, that $\min |\Psi(x, y)| = 0$ is reached during the transformation from hexagons to domains.

The absolute value of the strongest Fourier mode's wave vector is usually indirectly proportional to the lattice spacing. In Fig. 6.7(b), this quantity is shown for various pump powers both for the Fourier transformation of $\Psi(x, y)$ (red dots) and $E(x, y)$ (blue dots). The monotonous decrease refers to the the fact, that the lattice spacing increases with the pump power. The blue and red dots are almost identical. This behavior is an indication, that the system is still away from the excitonic resonance. Further increasing Δ will cause a considerable difference between these two values, cf. Figs. 6.10(b) and (d) in the next subsection.

6.1.3. Pattern formation above the excitonic resonance

Near the nonlinearly blue-shifted excitonic resonance, many spatial frequencies are excited likewise. For detunings above the linear excitonic resonance ($\Delta_0 = 0$), a crucial influence of the strongly nonparabolic LPB dispersion can be expected, which will manifest itself in effects involving large wave vectors k (cf. Fig. 5.5(d)).

We note that the model (2.13)-(2.14) disregards the strong dephasing mechanisms of exciton-polaritons with very large values of k (i.e. almost free excitons). These additional relaxation mechanisms are associated mostly with the scattering of the almost free excitons with acoustic phonons [183]. Therefore the model (2.13)-(2.14) is reasonable only if the overwhelming part of the spectrum is bounded within the domain of the polariton dispersion relation where the photonic component does not vanish. It is worth mentioning that this condition is satisfied for all solutions obtained here even for the case of slightly positive detunings $\Delta_0 < 2\gamma_0$, cf. Fig. 5.7(a).

The appearance of large wave vectors k in the spectrum can lead to the breakup of hitherto perfect hexagonal patterns and the formation of domains without long-range order. We

note that impurities occur at almost all detunings, as long as a sufficiently high pump power is applied. In general, the loss of periodicity and long-range order far away from the bifurcation point is a typical scenario for pattern formation in dissipative systems [79, 83]. The peculiarity of the examples studied in this section is that these defects already appear near the bifurcation point, so that the pump range of perfect hexagonal patterns decreases and finally vanishes for sufficiently high detuning above the linear excitonic resonance.
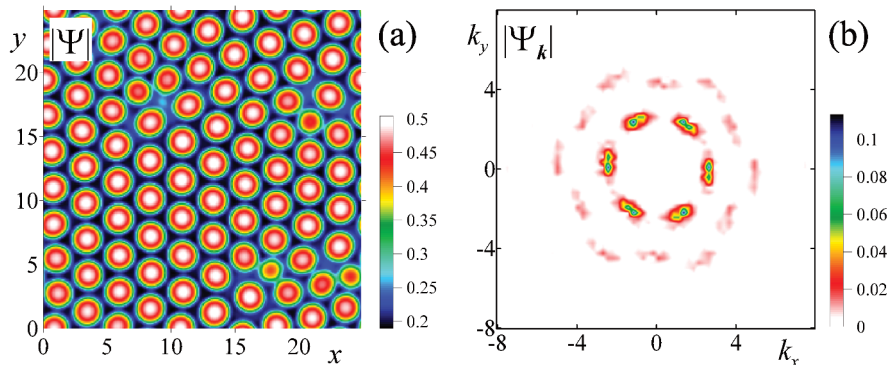

Figure 6.8: (a) $|\Psi(x,y)|$ for $\Delta = 0.1$ and $E_p = 0.322$: penta-hepta defects appear, (b) Fourier transformation $|\Psi_{\mathbf{k}}|$ of (a) normalized to omitted HS background.

For instance, slightly above the linear excitonic resonance one observes first imperfections in the patterns such as penta-hepta defects (cf. Fig. 6.8(a) and [79]). Intuitively, the formation of these defects can be explained by examining the growth rate $\Re\lambda(k, |\Psi_0|)$ at the critical intensity for the respective detunings. For $\Delta = 0.1$, the excitable wave vectors span a range of almost an octave, cf. Fig. 5.5(d). Consequently, the interaction of different patterns with more than one wave vector is observed, which results in the formation of point defects, shown in Fig. 6.8(a). The Fourier transformation in Fig. 6.8(b) confirms the interpretation of two competing patterns.
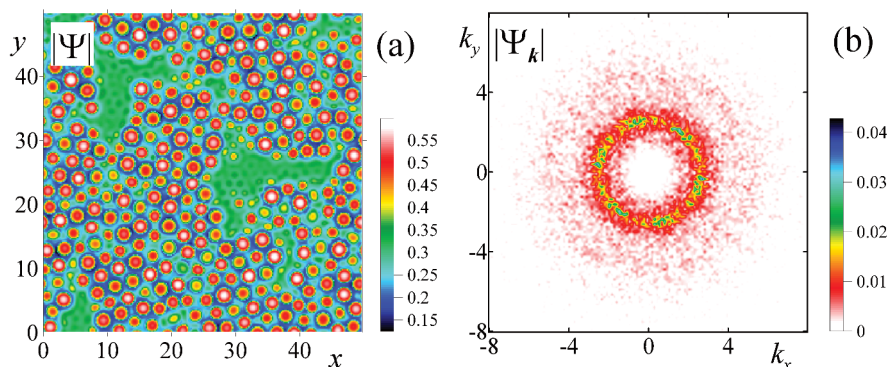

Figure 6.9: (a) $|\Psi(x,y)|$ for $\Delta = 0.15$ and $E_p = 0.318$: loss of long-range order, formation of domains where short-range order is still conserved, (b) Fourier transformation $|\Psi_{\mathbf{k}}|$ of (a) normalized to omitted HS background.

The beating between different modes gets even more pronounced, if the detuning is

furthermore increased. For $\Delta = 0.15$, patterns with wave vectors $2 \lesssim k \lesssim 7$ can be excited. The resulting loss of long-range order manifests itself in the formation of separated domains, each of them still possessing short-range order between its building blocks, cf. Fig. 6.9(a). The corresponding Fourier profile shows the competition of many modes. However, their wave numbers $k = \sqrt{k_x^2 + k_y^2}$ are confined in the range of 2.5 to 2.8. This fact provides the regular features such as short-range order.
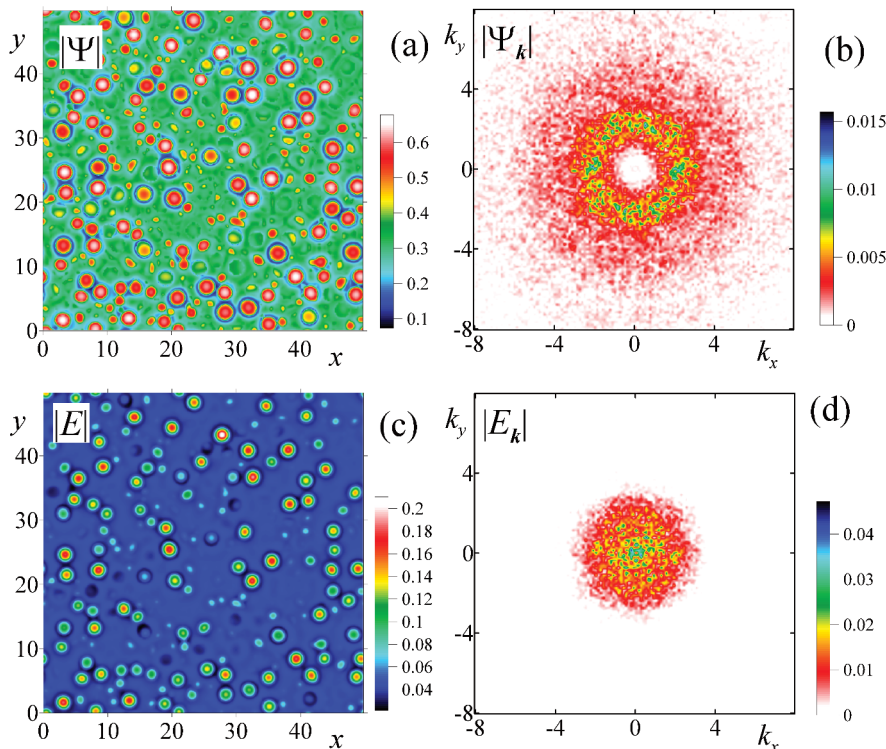

Figure 6.10: (a) $|\Psi(x,y)|$ for $\Delta = 0.19$ and $E_p = 0.3142$, total loss of short- and long-range order leading to the formation of a gas of polariton solitons, (b) Fourier transformation $|\Psi_{\mathbf{k}}|$ of (a) normalized to omitted HS background; (c) and (d) show the respective quantities of the photonic component.

For $\Delta = 0.19$ the nonlinear interaction of various patterns with many different wave vectors must lead to a loss of short-range order between the constituents of these patterns, which exactly means the formation of a gas of independent polariton solitons, cf. Fig. 6.10(a) and (c) for its excitonic and photonic component, respectively. The interaction between polaritons from the lower and upper polariton branch causes the formation of these hybrid breathing polariton solitons [144]. The comparison between the shapes of the excitonic and photonic component of the field reveals the influence of the nonlinearity, which softens the sharp edges of $|\Psi(x,y)|$, whereas the more pronounced shape of $|E(x,y)|$ is dominated by the photon diffraction. This feature is even more evident in the respective Fourier profiles. The brightest spots of the Fourier transformation of $\Psi(x,y)$ lie on a circular ring between about $k = 2$ and $k = 3$, cf. Fig. 6.10(b). The Fourier transformation

of $E(x, y)$, however, is concentrated in the region with $k < 1$. Both Fourier profiles reflect the internal structure of the respective component of the breathers, as it was shown for single solitons in Ref. [144]. The discrepancy between the two Fourier profiles can be explained with the help of the polariton dispersion relation: pumping near the excitonic resonance leads to solutions with high k, i.e., solutions with a strong excitonic component. On the other hand, the comparably weak photonic component is characterized by wave vectors in the vicinity of the origin.

Similarly, the transmutation from a stationary two-dimensional pattern to localized structures consisting of a sharp peak emitting concentric rings of alternating high and low intensities was reported in Ref. [184] using a degenerate optical parametric oscillator. This behavior is explained by the interaction of a Hopf bifurcation and a Turing bifurcation leading to a competition between the respectively arising periodic and stationary patterns.

The transition from periodic optical patterns to multipeaked cavity solitons was also studied in Refs. [185, 186] for a saturable absorber in a cavity. In Ref. [187] the spontaneous crystallization of a gas of solitons in a polariton Bose-Einstein condensate is investigated.

The upper limit for the formation of patterns was calculated in Sec. 5.3 and is $\Delta_0 = 2\gamma_0$, thus $\Delta = 0.2$. As long as one stays below this *nonlinear* resonance, it is also justified to neglect the exciton dispersion which is $10^4 - 10^5$ times weaker than the photon diffraction.

6.2. Pseudospin dynamics of polariton patterns

Including the exciton spin adds a vectorial degree of freedom to the equations of motion. This was described exemplarily for the case of a Kerr nonlinearity in Refs. [80, 81]. Since the polariton equations with exciton spin exhibit the same structure in the nonlinearity they can be expected to share several characteristics derived for the Kerr cavity. These transverse instabilities mediated by the polarization effects typically lead to the formation of hexagonal or stripe patterns. However, the dynamics of the polarization fronts can also lead to labyrinthine patterns, cf. Ref. [188] for the case of degenerate four-wave mixing.

The cross-phase modulation parameter α between the two spins can have either sign [151, 153, 159, 189]. The HS analysis in Sec. 5.3 has revealed that the expected shape of the arising patterns depends crucially on this sign. Whereas for $\alpha > 0$ a linearly polarized solution consisting of two identical polarization patterns is expected, for $\alpha < 0$

the spontaneous symmetry breaking manifests itself in the formation of two spatially shifted polarization patterns associated with opposite exciton spins. This behavior is consistent with the typology of symmetric and asymmetric solutions introduced in Sec. 4.1 and examined analytically for HSs in Sec. 5.3.

For $\alpha = 0$ the equations for both $+/-$ polaritons degenerate to two decoupled scalar equations which were already investigated Sec. 6.1.

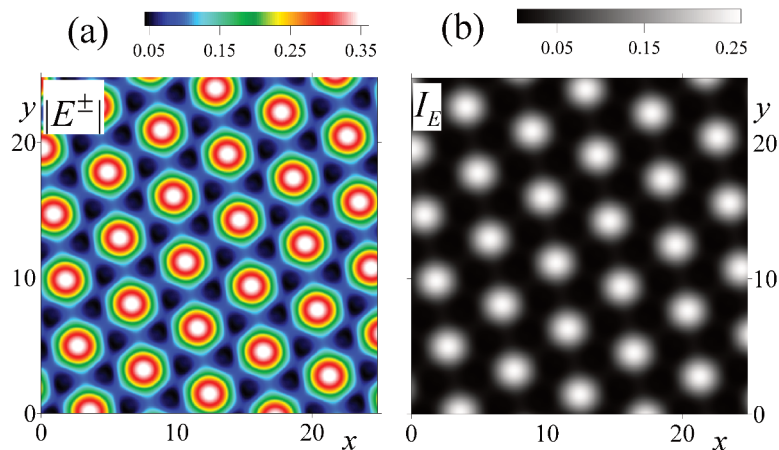## 6.2.1. Symmetric intensity patterns for positive cross-phase modulation parameter α

Figure 6.11: (a) Two-dimensional profile $|E^+(x,y)| = |E^-(x,y)|$ of a hexagonal pattern for $\alpha > 0$; (b) field intensity $I_E(x,y) = |E^+(x,y)|^2 + |E^-(x,y)|^2$. Parameters are $\alpha = 0.1$, $\Delta = -0.1$ and $E_p = 0.35$.

For $\alpha > 0$ the two fields are actually coupled. Hexagonal patterns arise above the bifurcation point for MI. The patterns for both polarizations are identical (cf. Fig. 6.11(a)) which manifests itself in a linearly polarized hexagonal pattern with polarization degree $\rho_E(x,y) \equiv 0$. Therefore the location of maxima and minima of the field intensity $I_E(x,y)$ coincides with that of the respective field moduli $|E^\pm(x,y)|$, cf. Fig. 6.11(b). This symmetric pattern fulfills the prediction from Sec. 5.3 where its symmetry was deduced from the fact, that the symmetric perturbations are preferred compared with the antisymmetric ones for $\alpha > 0$. These symmetric patterns do not exhibit any novel properties in comparison with the scalar patterns studied in Sec. 6.1.

6.2.2. Asymmetric pseudospin patterns patterns for negative cross-phase modulation parameter α

For the physically more relevant case $\alpha < 0$, however, antisymmetric perturbations are dominating. This is reflected by a spontaneous spatial shift between the patterns of the two polarizations similar to the spatial splitting between dark solitons reported in Ref. [165], cf. Sec. 7.2.
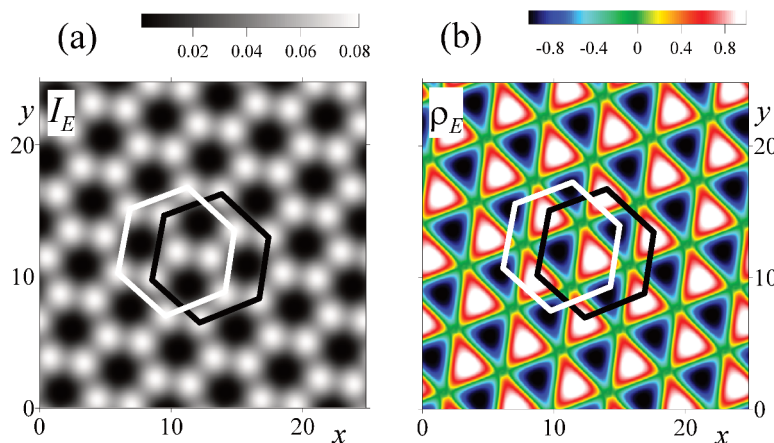

Figure 6.12: Symmetry breaking mechanism leading to the formation of vectorial hexagonal patterns for $\alpha < 0$: (a) total intensity $I_E(x,y) = |E^+(x,y)|^2 + |E^-(x,y)|^2$ of the photon field; (b) polarization degree $\rho_E(x,y)$. The white (black) hexagon indicates the maxima of $|E^-(x,y)|$ ($|E^+(x,y)|$). Parameters are $\alpha = -0.1$, $\Delta = -0.1$ and $E_p = 0.35$.

In Fig. 6.12 a prototypical example near $I^-_{0,\text{crit,as}}$ for $\Delta = -0.1$ is studied. Figure 6.12(a) shows the total field intensity $I_E(x,y)$. Although being hexagonal, the arising intensity pattern differs substantially from the intensities of the single polarizations, because the spatial splitting between the two hexagonal lattices is not small but rather in the same order of magnitude as the the lattice spacing. $I_E(x,y)$ can be classified as honeycomb-like, despite being formed by two hexagonal patterns $|E^+(x,y)|$ and $|E^-(x,y)|$. The spatial shift between these two patterns is indicated by the black and white hexagon indicating the maxima of $|E^+(x,y)|$ and $|E^-(x,y)|$, respectively. It manifests itself in the nontrivial polarization degree $\rho_E(x,y)$ depicted in Fig. 6.12(b). The spatial shift between the two polarizations matches with the structure of the patterns: the maxima of $|E^+(x,y)|$ coincide with the minima of $|E^-(x,y)|$ and vice versa.

A similar scenario can be observed near $I^-_{0,\text{crit,as}}$ for $\Delta = -0.45$, cf. Fig. 6.13. Here, $|E^+(x,y)|$ and $|E^-(x,y)|$ are shifted along a line coinciding with a basis vector of the hexagonal lattice. This changes the phenotype of the arising intensity pattern substantially. Figure 6.13(a) shows a stripe-like pattern. A look at Fig. 6.13(b) shows that both the bright and the dark stripes experience a modulation of the polarization degree. Therefore,
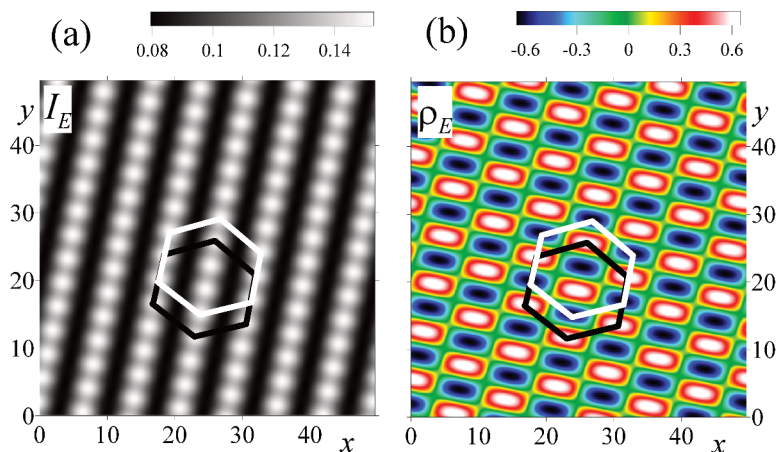
Figure 6.13: Symmetry breaking mechanism leading to the formation of modulated stripes for $\alpha < 0$: (a) total intensity $I_E(x,y) = |E^+(x,y)|^2 + |E^-(x,y)|^2$ of the photon field; (b) polarization degree $\rho_E(x,y)$. The white (black) hexagon indicates the maxima of $|E^-(x,y)|$ ($|E^+(x,y)|$). Parameters are $\alpha = -0.1$, $\Delta = -0.45$ and $E_p = 0.2816$.

the hexagonal nature of the pattern is preserved, at least with respect to the polarization degree $\rho_E(x,y)$.

Up to this point, we restricted our observations to the close vicinity of the bifurcation point $I^-_{0,\text{crit,as}}$ and varied mainly the detuning. However, in Subsec. 6.1.2 it was shown that for, e.g., $\Delta = -0.1$ the HSs show a monostable dependence on the pump power, cf. also Ref. [163]. This makes the whole modulationally unstable pump range accessible for the formation of a variety of stable extended patterns. In Fig. 6.14 we present two examples for different pump powers leading to different types of stripe patterns in I_E.

Figures 6.14(a)-(c) show vectorial labyrinthine patterns. From the polarization degree $\rho_E(x,y)$ in Fig. 6.14(c) it can be seen, that there is a spatial shift between the stripes of $|E^+(x,y)|$ and $|E^-(x,y)|$. Another peculiarity is the occurrence of point defects, marked in Fig. 6.14(c).

Near the upper bifurcation point $I^-_{0,\text{crit,as}}$, the field $|E^+(x,y)|$ forms a honeycomb pattern, cf. [163] and Fig. 6.14(d). The intensity profile in Fig. 6.14(e) shows several domains originating from various dislocations in the hexagonal structure of $|E^\pm|$. Whereas in the domain on the right, $I_E(x,y)$ preserves the original hexagonal structure due to impurities in the fields, the other domain shows a stripe-like pattern. The polarization degree $\rho_E(x,y)$ in Fig. 6.14(f), however, still bears the hexagonal symmetry of the original profiles.

All examples with $\alpha < 0$ in this section show genuine vectorial characteristics which can not be observed in the framework of the scalar model [163]. Furthermore, it was shown that the additional consideration of TE-TM splitting between the cavity modes induces a spontaneous motion of the whole polariton pattern, cf. Sec. 6.3 and Ref. [179].
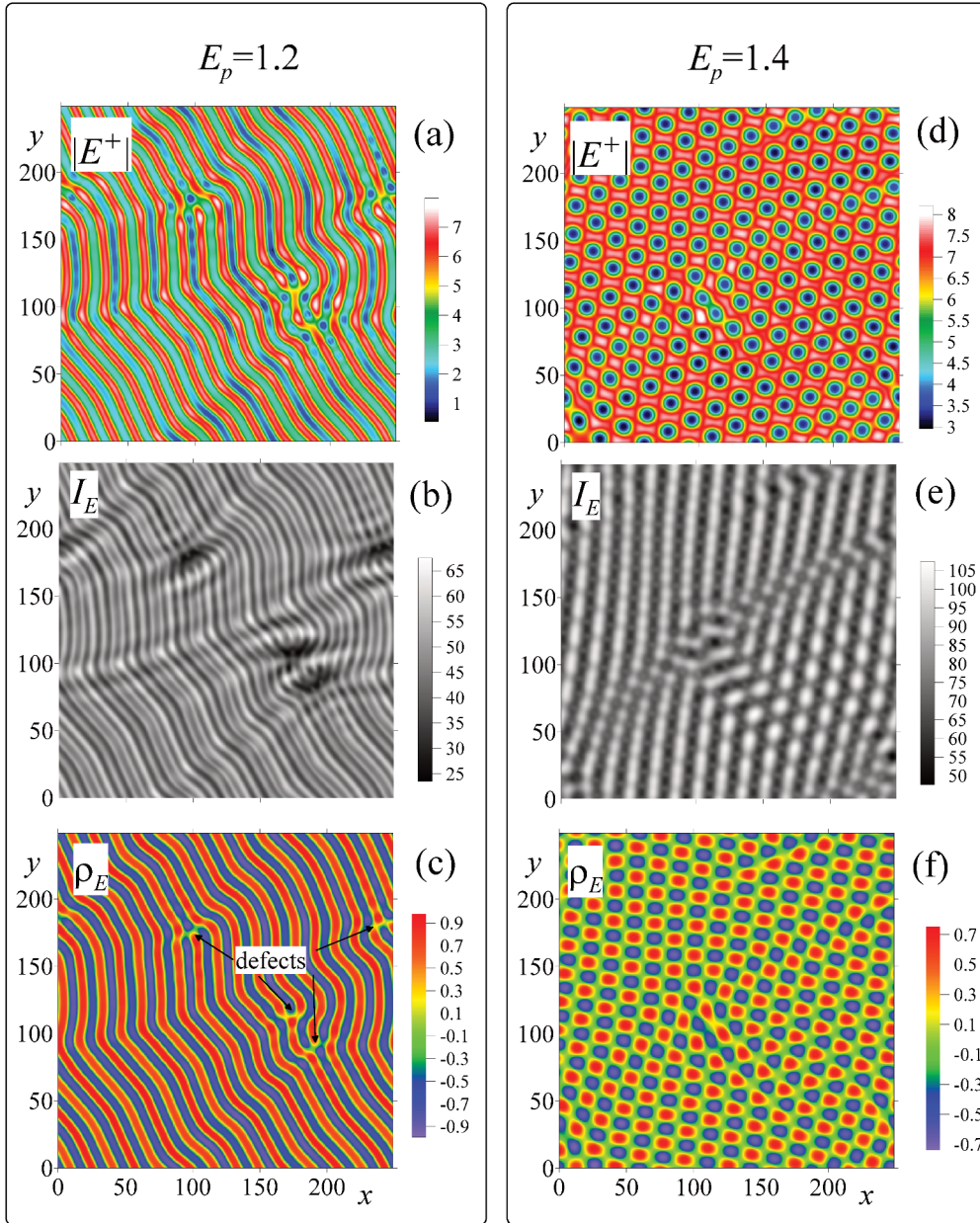
Figure 6.14: Formation of various vectorial patterns for $\alpha = -0.1$ and $\Delta = -0.1$: (a)-(c) labyrinthine stripe patterns for $E_p = 1.2$: (a) $|E^+(x,y)|$; (b) total intensity $I_E(x,y) = |E^+(x,y)|^2 + |E^-(x,y)|^2$ of the photon field; (c) polarization degree $\rho_E(x,y)$. (d)-(f) honeycomb patterns add to modulated stripes for $E_p = 1.4$: (d) honeycomb pattern $|E^+(x,y)|$; (e) stripe-like total intensity $I_E(x,y) = |E^+(x,y)|^2 + |E^-(x,y)|^2$ of the photon field; (f) hexagonally patterned polarization degree $\rho_E(x,y)$.

In Ref. [81] the formation of stripe patterns with uniform polarization degree along each stripe was reported for a vectorial Kerr cavity. However, in order to match the parameters used there in the polaritonic system studied here, one would have to choose $\alpha = 7$, which lies outside the physical range yet known for this parameter.

6.2.3. Formation of domain walls near the bottom of the lower polariton branch

For a scalar self-defocussing Kerr cavity it was previously claimed that pattern formation is frustrated in the bistable pump range, since all patterns are subjected to bistable switching which drives the solution to the stable upper branch of the bistability loop [79].
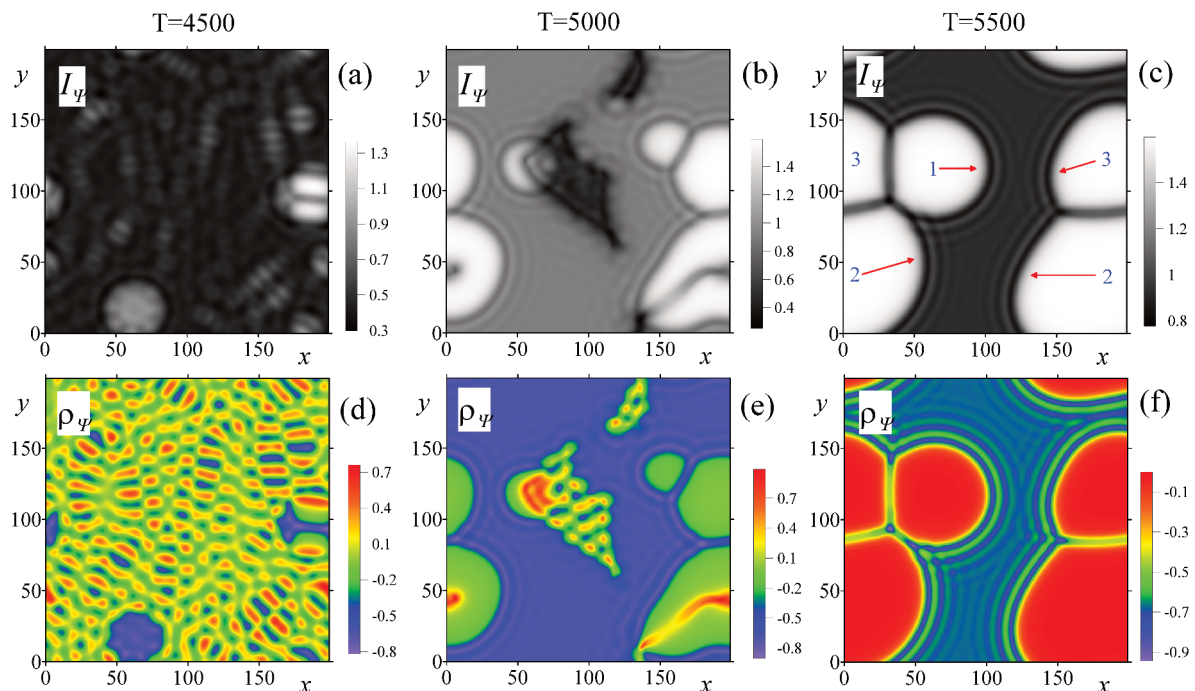

Figure 6.15: Buildup of a domain structure for $\Delta = -0.7$, $\alpha = -0.1$ and $E_p = 0.19$; (a)-(c) show the polaritonic intensity and (d)-(f) show the respective polarization degree; (a) and (d): formation of several condensation nuclei with both positive and negative polarization degree; (b) and (e): expansion and competition of the nuclei; (c) and (f): suppression of the condensation nucleus with positive ρ_Ψ, the expansion of the remaining enumerated nuclei is shown by red arrows.

In this subsection, it is shown that the aforementioned bistable switching to the upper part of the bistability loop can be circumvented in the case of vectorial exciton-polaritons according to Eqs. (3.4)-(3.5). Figure 6.15 shows the crucial moments of the dynamical evolution near the MI point for $\Delta = -0.7$. The excitonic component of the intensity and the respective polarization degree after 450 photon lifetimes are shown in Figs. 6.15(a) and (d), respectively. They still exhibit residues of a regular pattern. At some sites, the amplitude of the pattern is so high, that it enters the attraction range of the upper branch of the bistability loop. This leads to the formation of expanding domains with high amplitude, cf. Fig. 6.15(b). Figure 6.15(e) reveals, that these condensation nuclei occur in both polarizations likewise. However, competition between expanding domains with opposite polarization degree leads to the elimination of smaller regions in favor of larger

ones and eventually to the suppression of one polarization, cf. Figs. 6.15(c) and (f) for the status after 550 photon lifetimes. The profile consists of three spatially distinct domains designated by 1 to 3. It should be noted, that the used split-step Fourier algorithm for numerically solving Eqs. (3.4)-(3.5) requires periodic boundary conditions. The arrows denote the motion of the domain walls.
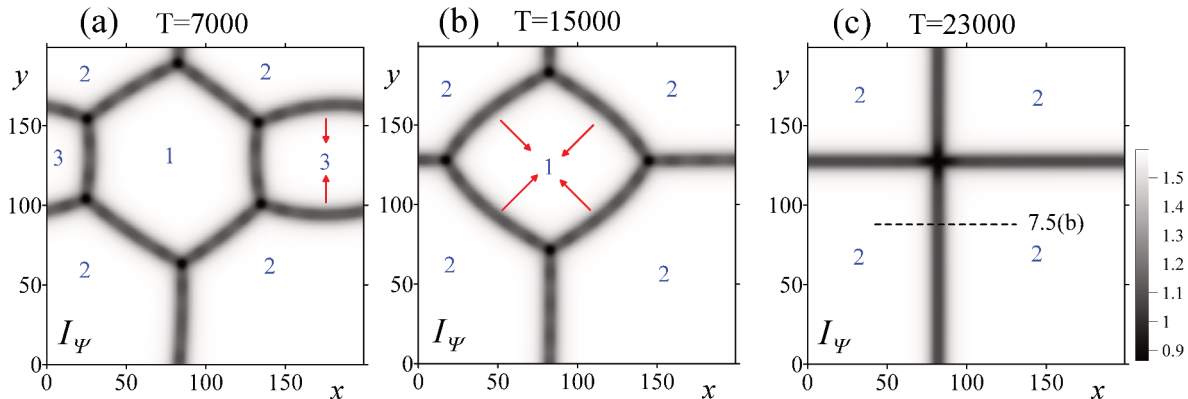

Figure 6.16: Movement of the domain structure built up in Fig. 6.15: (a) three spatially distinct domains (enumerated by 1 to 3) are separated by slowly moving dark solitons (direction of motion indicated by red arrows), (b) region 3 has vanished after the merging of the surrounding solitons, (c) region 1 has vanished, resulting in two crossed stationary dark solitons.

Once the polarization degree of all remaining domains has the same sign, it is obsolete to show $\rho_\Psi(x, y)$ which is qualitatively identical to $I_\Psi(x, y)$. The inflation of the domains ends, when they fill the entire x-y plane, cf. Fig. 6.16(a). They are separated by stable entities that can be interpreted as one-dimensional dark vector solitons [100, 165]. The vector solitons move slowly due to curvature forces [190]. Due to this motion the number of domains will decrease. The domain walls framing the smallest region, in this case region 2, have the largest curvature. After about 1500 photon lifetimes they merge eventually, cf. Fig. 6.16(b). The final steady state is reached after about 2300 photon lifetimes with the disappearance of all curved surfaces and of region 1, cf. Fig. 6.16(c). The formation of these stable patterns depends strongly on external parameters, namely the detunings and the pump power. In order to analyze the stability range of these patterns quantitatively it is useful to have a closer look at the dark vector solitons separating the domains in Fig. 6.16(c). This will be done in Subsec. 7.2.2. In particular, it is necessary to choose a pump power that lies both in the modulationally unstable pump range of the HSs and in the stable pump range of these solitons.

The destabilization of a spatially homogeneous flow leading to the formation of spin textured states surrounded by half solitons induced by the instability of a polaritons superfluid has been shown recently in Ref. [27]. The transformation from spin domains to half solitons driven by the transition from linear to nonlinear optical spin Hall effect was

shown in Ref. [191]. The formation of a Wigner crystal of half solitons [187] is a further example of self organization of a polarization pattern.

For $\alpha > 0$, the dark soliton solutions to be considered are symmetric [165]. Their stability range is significantly smaller than that of the asymmetric solitons reported for $\alpha < 0$. Particularly, the switching point to the upper branch of the bistability loop lies usually at too high pumps to match this stability range. Therefore, the stabilization mechanism presented in this section was not observed for positive α.

6.3. Moving hexagonal patterns due to TE-TM splitting

The polariton pseudospin [151] inherited from the excitons adds a new degree of freedom to the polariton dynamics. Its influence on the formation of spatial patterns has been studied extensively in the preceding section. In this section, we want to examine the influence of TE-TM splitting of the polaritons which was introduced to the equations of motion in Sec. 3.2. It causes a precession of the pseudospin whose rotation velocity depends on both the modulus and the direction of the polariton momentum $\mathbf{k}$, cf. Subsec. 5.3.4 and Refs. [151, 192–196]. The spatial separation between exciton-polaritons with different spins induced by this spin-orbit interaction is termed optical spin Hall effect [192–196]. Furthermore, the directionally dependent pseudospin precession due to the TE-TM splitting can cause a uniform motion of the whole polariton pattern linked with a directional density current. This effect was shown in our paper [179] and will be explained in this section.

Figure 6.1(b) shows a scalar pattern. Due to its hexagonal structure its Fourier components are also arranged in a perfect hexagon, cf. Fig. 6.1(c). In the following analysis, it is sufficient to disregard the internal structure of the Fourier peaks and treat them as point-like. Furthermore, the higher order peaks arising from the four-wave mixing can also be disregarded, since their amplitude is several orders of magnitude smaller than that of the main peaks.

If we now simulate the full equations of motion (3.15)-(3.16), vectorial patterns will arise due to $\alpha < 0$, cf. Sec. 6.2. The bright peaks of the scalar pattern therefore split into spatially separated spots with opposite polarization degree, cf. Figs. 6.12 and 6.13. This observation is also depicted in Figs. 6.17(a) and (b). Moreover, these patterns are subject to a uniform motion in the resonator plane whose velocity is proportional to β, cf. Figs. 6.17(c) and (d). Like in the optical spin Hall effect [192, 193], the polaritons experience a directionally dependent pseudospin precession whose rotation velocity and rotation direction shows a nontrivial dependence on the transverse wave vector $\mathbf{k}$, cf. Fig. 5.8.
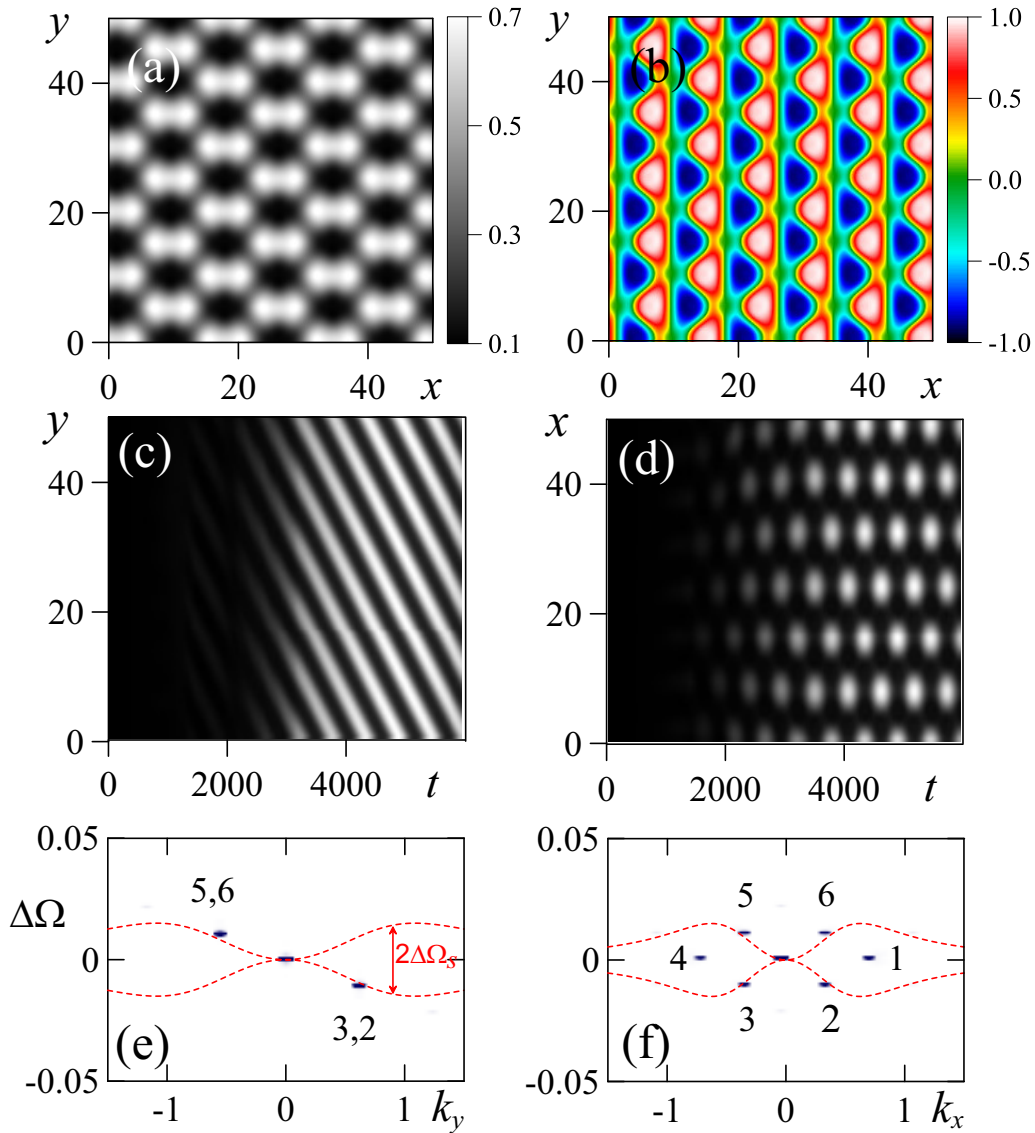
Figure 6.17: Moving hexagonal patterns for $\beta = 0.05$: (a) Intensity profile $I_E(x,y)$, (b) polarization degree $\rho_E(x,y)$, (c) and (d) show the time evolution of $I_E(x,y)$ through the sections $x = 0$ and $y = 0$, respectively, their respective Fourier components are depicted below in (e) and (f). The frequency shifts calculated with Eq. (6.11) are denoted with red dashed lines. Parameters are $\beta = 0.05$, $\alpha = -0.1$ and $E_p = 0.283$.

Therefore the different Fourier components enumerated with 1-6 in Fig. 6.1(c) are dressed with different phases which additionally show a slow time dependence. There is a direct link between the phase of these Fourier components and the position of the intensity maxima of the actual pattern. Thus the peaks of the pattern are forced to start a uniform drift.

The time evolution at the sections through $x = 0$ and $y = 0$ is depicted in Figs. 6.17(c) and (d), respectively. These figures illustrate the fact that the whole pattern moves uniformly parallel to the y axis. The Fourier transformations of these sections are shown in Figs.

6.17(e) and (f), respectively. The frequency components with $k_y > 0$ in Fig. 6.17(e), namely 2 and 3, are redshifted. On the other hand, the frequency components 5 and 6 having $k_y < 0$ are blueshifted by the same value. Therefore, these Fourier components lie in a plane which is slightly tilted along the k_y axis. For a given frequency shift $\Delta\Omega_s$ the velocity of the hexagonal pattern's movement can be read as the slope of the line connecting these points:

$$v = \frac{\Delta\Omega_s}{k_y} = \frac{\Delta\Omega_s}{k_0 \sin\theta}, \tag{6.1}$$

where k_0 and θ were defined in Fig. 6.1(c). In the following we want to derive an analytical expression for the frequency shift $\Delta\Omega_s$ connecting it with the polariton TE-TM splitting. Therefore the hexagonal pattern will be represented as a discrete Fourier series containing only the homogeneous background and its six main spectral components:

$$\begin{pmatrix} E^\pm \\ \Psi^\pm \end{pmatrix} = \mathbf{p}\,(0)\,A_0^\pm + \sum_{j=1}^{6} \mathbf{p}\,(k_0)\,A_j^\pm e^{i(\mathbf{k}_j + \Delta\mathbf{k}_j)\mathbf{r} - i\Delta\Omega_j t}. \tag{6.2}$$

Here, the vector $\mathbf{p}\,(k)$ contains the Hopfield coefficients for the lower polariton branch introduced in Eq. (5.2). It should be noted that these coefficients depend on the modulus of $\mathbf{k}_j$ and are thus identical for all six Fourier components. The momenta

$$\mathbf{k}_j = k_0 \begin{pmatrix} \cos\theta_j \\ \sin\theta_j \end{pmatrix} \quad \text{with } \theta_j = \frac{\pi}{3}\,(j-1) \tag{6.3}$$

are taken from the unperturbed scalar hexagonal patterns according to Fig. 6.1(c). The TE-TM splitting causes small corrections $\Delta\mathbf{k}_j$ to these momenta and $\Delta\Omega_j$ to the respective frequencies of the spatial components. Since the TE-TM splitting is rather small it is reasonable to assume the amplitudes A_j to be constant in first order. Inserting the ansatz (6.2) into the full equations of motion (3.15)-(3.16) yields a system of coupled nonlinear equations

$$(\Delta\Omega_j - \Delta_{\mathrm{LPB}}\,(\mathbf{k}_j + \Delta\mathbf{k}_j))\,A_j^\pm + N_j^\pm = \beta\,(i\,(k_{xj} + \Delta k_{xj}) \pm (k_{yj} + \Delta k_{yj}))^2\,e_{k_0}^2 A_j^\mp. \tag{6.4}$$

Here, the nonlinear mixing terms $N_j^\pm$ have the form

$$N_j^\pm \propto \sum_{m=0}^{6} \sum_{n=0}^{6} \left(A_m^\pm A_n^{*\pm} + \alpha A_m^\mp A_n^{*\mp} \right) A_{j-m+n}^\pm, \tag{6.5}$$

where A_{j-m+n} denotes the amplitude of the mode with $\mathbf{k} = \mathbf{k}_j - \mathbf{k}_m + \mathbf{k}_n$. Since the dispersion relation has to be fulfilled, there are several phase (and frequency) matching

conditions which had to be met in order to derive Eq. (6.4). They read

$$\Delta \mathbf{k}_1 = -\Delta \mathbf{k}_4, \quad \Delta \mathbf{k}_2 = -\Delta \mathbf{k}_5, \quad \Delta \mathbf{k}_3 = -\Delta \mathbf{k}_6, \quad \Delta \mathbf{k}_1 = \Delta \mathbf{k}_2 + \Delta \mathbf{k}_6 \qquad (6.6)$$

and

$$\Delta \Omega_1 = -\Delta \Omega_4, \quad \Delta \Omega_2 = -\Delta \Omega_5, \quad \Delta \Omega_3 = -\Delta \Omega_6, \quad \Delta \Omega_1 = \Delta \Omega_2 + \Delta \Omega_6, \qquad (6.7)$$

respectively. The TE-TM proportional to the small parameter β induces small corrections $\Delta \Omega_j$ and $\Delta \mathbf{k}_j$ to the frequencies and the wave vectors of the hexagonal pattern, respectively. Expanding Eq. (6.4) up to first order in these small perturbations yields

$$\left(\Delta \Omega_j - 2\Delta'_{\text{LPB}} \left(k_0^2 \right) \left(k_{xj} \Delta k_{xj} + k_{yj} \Delta k_{yj} \right) \right) A_j^{\pm} = \beta e_{k_0}^2 \left(i k_{xj} \pm k_{yj} \right)^2 A_j^{\mp}. \qquad (6.8)$$

The leading term of the Taylor expansion of the lower polariton branch reads

$$\Delta'_{\text{LPB}} \left(k_0^2 \right) \equiv \left. \frac{\partial \Delta_{\text{LPB}} \left(k^2 \right)}{\partial \left(k^2 \right)} \right|_{k^2 = k_0^2} = \frac{1}{2} \left(1 - \frac{k_0^2}{\sqrt{4 + k_0^4}} \right). \qquad (6.9)$$

Evaluating the solvability condition of the homogeneous system of linear equations (6.8) leads to an expression connecting the frequency and the phase shifts:

$$\Delta \Omega_j = 2\Delta'_{\text{LPB}} \left(k_0^2 \right) \left(k_{xj} \Delta k_{xj} + k_{yj} \Delta k_{yj} \right) \pm \frac{1}{2} \beta k_0^2 \left(1 - \frac{k_0^2}{\sqrt{4 + k_0^4}} \right). \qquad (6.10)$$

This relation must be fulfilled by the Fourier components of the moving hexagonal pattern, cf. Figs. 6.17(e) and (f). The relations $\Delta \Omega_1 = 0$ and $\Delta \Omega_4 = 0$ can be fulfilled by $\Delta k_{x1} = \frac{1}{2} \beta k_0$ and $\Delta k_{x4} = -\frac{1}{2} \beta k_0$, respectively. The requirements for $\Delta \Omega_{2,3} = -\Delta \Omega_{5,6} = -\Delta \Omega_s$ are met if the respective wave vectors fulfill the relations $\Delta k_{x2,5} / \Delta k_{y2,5} = -\Delta k_{x3,6} / \Delta k_{y3,6} = -\tan (\pi/3) = -\sqrt{3}$. The frequency shift $\Delta \Omega_s$ is then given by

$$\Delta \Omega_s = \frac{1}{2} \beta k_0^2 \left(1 - \frac{k_0^2}{\sqrt{4 + k_0^4}} \right). \qquad (6.11)$$

It should be noted that these corrections are constructed in a manner that they fulfill both the phase matching conditions (6.6) and the frequency matching conditions (6.7). The formula (6.11) for the frequency splitting shows a structural similarity to the TE-TM splitting of the lower polariton branch according to Eq. (5.6). However, they differ by a factor of 2. Nonetheless, this highly unexpected similarity allows for another way to explain the uniform movement of the pattern: Due to the TE-TM splitting of the lower

polariton branch, cf. Fig. 5.2, the Fourier components of the hexagonal pattern can jump spontaneously to the subbranches of the lower polariton branch. The phase-matching condition (6.6) demands opposite Fourier components to enter different subbranches. This leads to an effective tilt of the hexagon along a certain axis in Fourier space[b], cf. Fig. 6.17(e). The structural similarity of the expressions (5.6) and (6.11) for the frequency shift can be regarded as a main achievement of the analysis in Sec. 5.1, since it shows a link between a highly elaborate numerics-aided analysis and a very basic study of the linear dispersion relation's behavior due to TE-TM splitting.
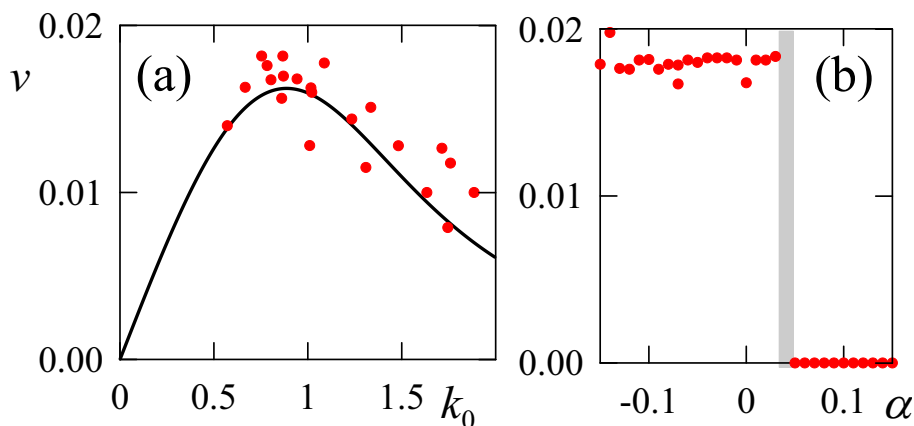

Figure 6.18: (a) Drift velocity of moving hexagonal patterns over their main wave vector k_0. The red dots denote results from direct simulations of the equations of motion. The solid black line displays the analytical result in Eq. (6.1). (b) Velocity of the patterns over the parameter α from direct simulations.

The dependence of the main wave vector k_0 on the detuning and the pump power was studied in Sec. 6.1 for scalar patterns. The velocity of various moving patterns taken from simulations of the vectorial equations of motion (3.15)-(3.16) for various detunings and pump powers is plotted over the main vector k_0 of the pattern (red dots in Fig. 6.18(a)). These finding show a marvellous agreement with the analytical result from Eq. (6.1). Deviations may be explained by the fact that we had to approximate the Fourier amplitudes A_j as constant in the derivation of the analytical formula.

In Fig. 6.18(b) the velocity is plotted over α, taken from direct simulations of the equations of motion. Moving hexagonal patterns arise for negative values of α and also for small positive values of α. If α exceeds a positive threshold, however, the arising patterns become stationary. This behavior can be explained by looking at the structure of the different patterns. It turns out that all stationary patterns are linearly polarized whereas the moving patterns exhibit a nontrivial polarization degree. In Secs. 5.3 and 6.2 we showed for $\beta = 0$ that $\alpha < 0$ leads to asymmetric patterns ($E^+(x, y) \neq E^-(x, y)$), whereas

---

[b]This axis is imprinted to the system by the polarization state of the pump. In the present case the tilt is along the k_y axis, cf. Fig. 6.17(e).

$\alpha > 0$ results in symmetric patterns ($E^+(x,y) = E^-(x,y)$). Since the TE-TM splitting breaks the symmetry between $+$ and $-$ fields, this threshold will be lifted a bit to positive α. Above the threshold value (cf. gray region in Fig. 6.18(b)) the symmetrizing force stemming from α overpowers the symmetry breaking induced by β. However, the existence of two spatially shifted solutions in the $+$ and $-$ polarization is a prerequisite for the observed spontaneous movement. Note that the motion of molecules formed by vector solitons was shown in Ref. [145]. This is also the reason why the movement reported here could not be observed earlier in the framework of vectorial Kerr cavities [80, 81] since there the cross-phase modulation parameter is usually not negative but positive and much larger than one.

6.4. Chapter summary and concluding remarks

This chapter contains a comprehensive overview over the formation of spatially periodic transverse polariton pattern in a semiconductor microcavity. It summarizes the result of numerous numerical simulations. These simulations were based on the MI analysis from Sec. 5.3 which particularly facilitated the choice of appropriate parameters (detunings, pump power).

The scalar equations of motion (2.13)-(2.14) already exhibit different regimes of pattern formation. Near the bottom of the lower polariton branch the dynamics is expected to be similar to that of Kerr cavities. However, we observed the formation of subcritically bifurcating hexagonal patterns with the pump range of bistable HSs. These findings prove the statement wrong that pattern formation suffers from bistable switching to the upper HS in the bistable regime [79]. However, the stability range of the polariton patterns is comparably small.

By increasing the detuning towards the excitonic resonance this stability range can be increased. For $\Delta > -0.18994$ the HSs depend monostably on the pump power which allows the formation of stable extended patterns over the whole modulationally unstable pump range. Whereas near the smaller (bigger) critical intensity according to Eq. (5.13) the arising patterns are undisturbed hexagons (inverted hexagons), they suffer from point defects if one chooses pump powers further away from these critical points and eventually lose their short-range order thus forming domains. Going even further away from the critical points leads to the formation of labyrinthine stripe pattern. Approaching an finally crossing the excitonic resonance $\Delta_0 = 0$ introduces a new effect: the hitherto perfect hexagonal patterns experience point defects already at the critical intensity. By

approaching the nonlinearly blueshifted excitonic resonance $\Delta_0 = 2\gamma_0$ this behavior becomes more pronounced by forming a gas of oscillating polariton solitons.

The exciton spin adds an additional degree of freedom to the system. Since the equations of motion are symmetric under the permutation of spins $+1$ and -1, they exhibit both linearly and elliptically polarized solutions for a linearly polarized pump beam. We found that the sign of the cross-phase modulation parameter α between excitons with different spins is crucial for the topology of the arising patterns. For $\alpha > 0$ the linear polarization of the pump is conserved in the arising hexagonal patterns which can be reduced to the scalar pattern by a simple scaling of all fields. For $\alpha < 0$, however, the spin symmetry is broken spontaneously. This symmetry breaking is expressed in a spatial shift between the two patterns connected with opposite spins. Depending on their displacement the resulting intensity pattern can either be honeycomb-like or consist of modulated stripes. Like in the scalar case, the occurrence of domain structures and labyrinthine patterns was shown for sufficiently high detunings. Near the bottom of the lower polariton branch one can observe the spontaneous formation of stable domains framed by one-dimensional dark vector solitons. This mechanism also counteracts the bistable frustration of pattern formation reported for Kerr cavities.

The aforementioned symmetry of the equations of motion is broken directly by the TE-TM splitting of the cavity modes. This additional term forces the vectorial patterns to move uniformly in one of the transverse directions. Similar to the optical spin Hall effect, this motion is induced by the directionally dependent pseudospin precession of the polaritons, cf. Subsec. 5.3.4. An analytical expression for the dependence of the velocity on the main wave vector of the pattern was derived from a nonlinear analysis of the shift of the hexagonal pattern's Fourier components. The comparison with the simulation results shows good agreement.

7. Dynamics of dark polariton solitons

After having studied spatially extended polariton patterns in Chapt. 6, we shall have a look at spatially confined structures in Chapts. 7 and 8. This chapter is devoted to the study of dark cavity solitons. In Chapt. 8, we will investigate bound states of domain walls. Before dealing with the formation of spatially confined structures in a polaritonic microcavity, we want to introduce the basic concepts in the framework of simpler nonlinear systems. A prototypical model where the formation of spatial solitons and bound states can be studied is given by the nonlinear Schrödinger equation (NLSE) [197]. The balance between defocussing tendencies due to diffraction and the (re-)focussing due to the nonlinear medium can lead to the formation of stable wave packets which conserve their finite size. Since the NLSE in one transverse dimension is integrable [87, 91, 198], higher order solitons can be found by the inverse scattering method. It is important to note that all these solutions are represented by discrete spots in phase space. This characteristic feature is due to the absence of losses and suggests the denotation conservative soliton or Hamiltonioan soliton. Due to their robustness and their spatial confinement, solitons are promising candidates for all-optical information storage and processing devices [6, 55, 56, 92, 93, 199, 200]. Depending on the sign of the difference between the soliton's peak intensity and the intensity of the surrounding HS, one distinguishes between bright and dark solitons. Bright solitons are characterized by a spot with high intensity embedded in a HS of lower intensity. Dark solitons, however, are formed by a spot of low intensity nesting on a HS of higher intensity. In the lossless case, it is even possible to reach a lower intensity of zero in both cases. Dark solitons can be set and reset by an optical control pulse. This allows the interpretation of a dark soliton as an optical bit in the framework of an all-optical information storage device.

Nondiffracting wave packets were also observed in nonlinear cavities [48, 55, 56, 90, 92–98, 184, 201]. These solutions are not solitons in the strict sense as introduced above. An additional condition for their stability is the balance between losses and energy supply. Thus these solutions are usually termed cavity solitons. It should be noted, that it is also possible to create dissipative solitons without using cavities. The denotation cavity soliton was introduced in 1998 in Ref. [202]. However, the concept of cavity solitons as self-trapped switching waves was introduced before in Ref. [99]. Contrary to the Hamiltonian systems studied above, the pump power then parameterizes a continuous family of solitons. In the language of dynamical systems, this family of solitons displays

an attractor in phase space. This observation turns out to be important, when one tries to create solitons either in a simulation or in an experiment. By shining a spatiotemporally limited excitation beam, it is possible to prepare a state which is in the attraction range of the attractor and will finally approach it when evolved in time. After this localized state has formed, it can stay forever, even after its excitation beam has been turned off.

All cavities mentioned above in Refs. [48, 55, 56, 90, 92–98, 184, 201] have been opperated in the weak-coupling regime. It should be noted that applications of cavity solitons in the weak-coupling regime are limited by the relatively weak nonlinearity and slow response times. The typical pump intensities needed to evoke bistability are therefore in the range of 10 kW/cm². In the strong-coupling regime, however, the nonlinearity which is of excitonic origin, is about two orders of magnitude stronger [3, 111, 135, 203]. Therefore the required pump intensity can be decreased down to about 100 W/cm² which would enable low-threshold optical bistability [39, 40, 204] and thus make the strong-coupling regime even more interesting for the above mentioned applications. Another advantage of the strong-coupling regime originates from the typical response times of the coherent interaction lying in the picosecond range, cf. Sec. 2.1. This is about three orders of magnitude faster than the incoherent interaction in the weak-coupling regime. One can conclude that the strong-coupling regime would allow for fast applications at comparably low pump energies.

Trapping photons in small volumes is also a demanding task. Thus it would be difficult to achieve a dense packing of light-only cavity solitons, as it is the case in the weak-coupling regime, where cavity solitons can have a typical diameter of about $10\,\mu$m. The polaritons formed in the strong-coupling regime, however, have a much smaller effective wavelength originating from their excitonic component [3, 12, 111, 134]. The diameter of the two-dimensional polariton solitons can be reduced to about $3\,\mu$m [170]. This would also be the approximate size of the respective optical bit.

Solitonic effects have also been discussed in the framework of polariton condensates [31, 32] and shown experimentally [205] in microcavity operated in the strong-coupling regime. Furthermore polariton droplets arising from parametric effects have been observed in Refs. [23, 196, 206]. A special type of topological soliton is referred to as vortex [17, 28, 31, 32, 38, 162]. These vortices also offer possibilities as polaritonic memory devices [38].

The properties of dark solitons arising from the scalar equations of motion are summarized in Ref. [100]. The discussion of dark solitons with consideration of the exciton spin in Secs. 7.1 and 7.2 will be based on these findings and has been published in our paper [165]. Similar to the case of extended patterns, the shape of the arising stable solitons turns out

to depend on the sign of the cross-phase modulation parameter α. Stable solutions for $\alpha > 0$ will again merely arise from the scalar case by scaling all fields with $\sqrt{1 + \alpha}$. For $\alpha < 0$, however, a spontaneous spatial symmetry breaking between the two polarizations similar to that for the vectorial patterns investigated in Sec. 6.2 will lead to the formation of vectorial solitons.

7.1. Linearly polarized two-dimensional solitons for positive cross-phase modulation parameter α

The nature of stable solitons arising in a nonlinear system is dictated by the relative sign η between the nonlinearity and the diffraction term. This is discussed in the framework of the Lugiato-Lefever model in Refs. [78, 79, 207]. In the self-focussing case ($\eta = +1$) stable bright solitons can form. In the self-defocussing case ($\eta = -1$) these bright solitons are usually unstable since nonlinearity and diffraction do not counteract but both result in an outwards pointing force on the flanks of the bright soliton. On the other hand, dark solitons are genuinely stable in the presence of a defocussing nonlinearity [87, 91, 98, 197]. Dark solitons always nest on the upper branch of a bistability loop, cf. Fig. 7.1. Therefore, the presence of bistable HSs is a necessary prerequisite for the existence of dark solitons. We have shown in Sec. 5.2 that the symmetric HSs are bistable for $-0.79516 < \Delta < -0.18994$. In the current section we will choose $\Delta = -0.7$ in order to meet the bistability condition.

In the framework of nonlinear optics, dark solitons were also discussed in, e.g., a cavity with a saturable defocussing nonlinearity [202], in semiconductor microcavities operated in the weak-coupling regime [48], and in a passive quantum-well-semiconductor resonator [90].

Furthermore, stable dark cavity solitons have been reported recently both theoretically and experimentally in the weak- [48, 87, 94, 208] and in the strong-coupling regime [170]. The profile $|\Psi^+(x, y)| = |\Psi^-(x, y)|$ of a two-dimensional dark polariton soliton is shown in Fig. 7.1(a). These linearly polarized solitons are also referred to as *symmetric solitons*. Figure 7.1(b) shows the section through the profile at $y = 0$. Note, that this section is not automatically a one-dimensional dark soliton, although these solutions also exist. It was pointed out before, that dissipative solitons can usually be represented by subsurfaces in phase space. In order to illustrate this fact graphically, it is reasonable to project these high-dimensional objects on a subspace spanned by only a few parameters. The arising branch is formed by the red lines in Figs. 7.1(c) and 7.1(d). The dark soliton is
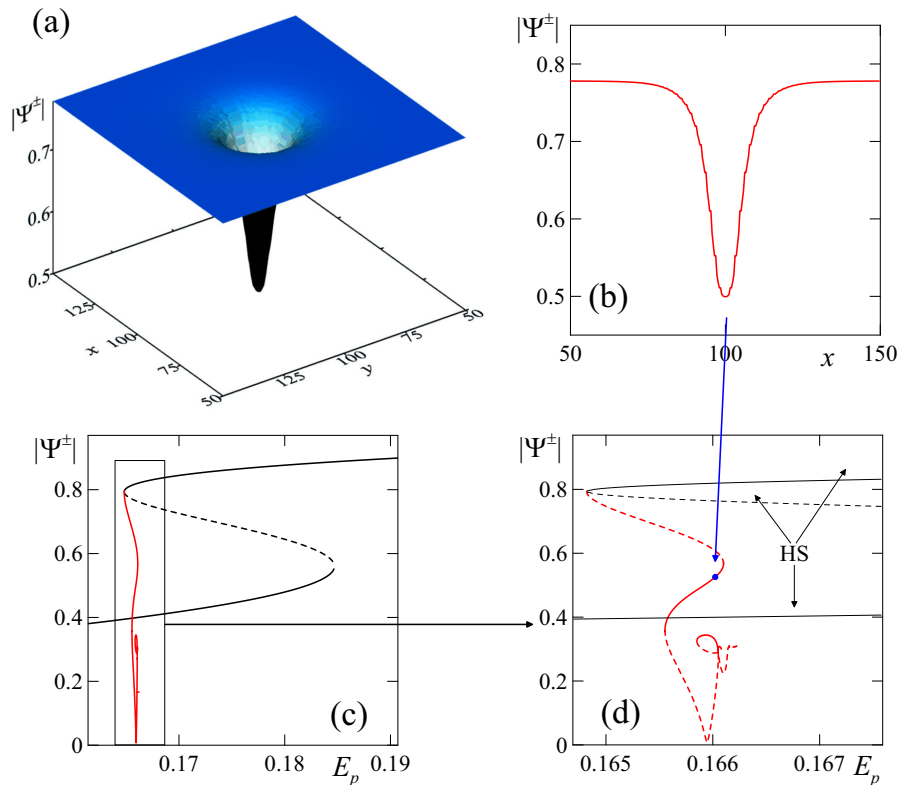
Figure 7.1: (a) Two-dimensional profile $|\Psi^+(x,y)| = |\Psi^-(x,y)|$ of a stable dark soliton at $E_p = 0.16603$, (b) section through (a) at $y = 0$, (c) amplitude of the symmetric homogeneous state (black line) and $\min|\Psi^{\pm}(x,y)|$ for dark solitons (red line), shown as a function of E_p, (d) is a close-up of the rectangular region from (c) showing the bifurcations and the branch $\min|\Psi^{\pm}(x,y)|$ of the dark soliton. The blue dot marks the position of the profile on the branch. Parameters are chosen $\Delta = -0.7$ and $\gamma_0 = \gamma_c = 0.1$. Bold lines denote stable solutions and dashed lines denote unstable solutions.

represented by $\min|\Psi(x,y)|$ which is plotted over the pump power E_p. The branch of the symmetric dark soliton bifurcates subcritically from the left folding point of the linearly polarized HSs' bistability loop. The soliton branch consists of alternating stable and unstable subbranches. Due to the subcritical nature of the bifurcation, there is an unstable subbranch in the vicinity of the bifurcation point. Its relative amplitude compared with the HS is small and increases with increasing E_p. It finally reaches a turning point after which the dark soliton stabilizes. This stable subbranch also contains the exemplary profile from Fig. 7.1(a), which is denoted by a blue dot. The stable dark soliton gets deeper by decreasing the pump power. This mechanism is typical for a subcritical bifurcation.

By decreasing E_p one then reaches the next turning point which displays the transition to another unstable soliton. Going along its branch leads straightforwardly to another transition which once again features a stable dark soliton. It is a higher-order soliton with a Mexican-hat like shape featuring a main minimum at $r \neq 0$. Thus it is separated in phase space from the first-order soliton. We will show in the framework of vectorial solitons, that it is possible to create a higher order soliton be merging two first-order

solitons, cf. Fig. 7.6.

It should be noted, that the results presented so far can be reduced to the scalar case presented in Ref. [170] by scaling all fields and the pump with $\sqrt{1 + \alpha}$. They serve as a prerequisite for the study of dark soliton formation with the inclusion of exciton spin, that will be presented in the following section.

7.2. Elliptically polarized solitons for negative cross-phase modulation parameter α

7.2.1. Two-dimensional vectorial solitons

After having examined the formation of linearly polarized solitons for $\alpha > 0$, we want to investigate the case $\alpha < 0$. The physical mechanisms originating from the exciton spin that act on the solitons will turn out to be similar to that described in the framework of pattern formation in Sec. 6.2. Whereas in the case of pattern formation, the spontaneous symmetry breaking leads to a relative shift of the whole polarization pattern for $\alpha < 0$, the solitons are spatially confined and thus allow to study this symmetry breaking mechanism in a purer form. Once again, the sign of α turns out to be the crucial parameter. We already know, that for $\alpha > 0$, the linearly polarized dark solitons are stable, cf. Sec. 7.1.

Branches and profiles

For $\alpha < 0$, the whole symmetric soliton branch destabilizes, cf. the dashed blue branch in Fig. 7.2(a). More precisely, any asymmetric perturbation grows exponentially in time eventually switching to elliptical polarization. Of course, this symmetric branch then bifurcates from the left folding point of the bistability loop formed by the symmetric HSs. The destabilization of the symmetric soliton is comparable to the destabilization of symmetric patterns described in Sec. 6.2. A qualitatively new family of stable vectorial solutions arises via spontaneous symmetry breaking for $\alpha < 0$. It has to be emphasized that the symmetry between fields with pseudospin $+1$ and -1 only exists for a linearly polarized pump ($\rho_{E_p} = 0$). The spontaneous breaking of this symmetry leads to stable elliptically polarized stable solutions despite a linearly polarized holding beam. This effect highlights the physical relevance of the polariton pseudospin. The same objective cannot be addressed if the symmetry of the equations of motion is broken a priori by applying an
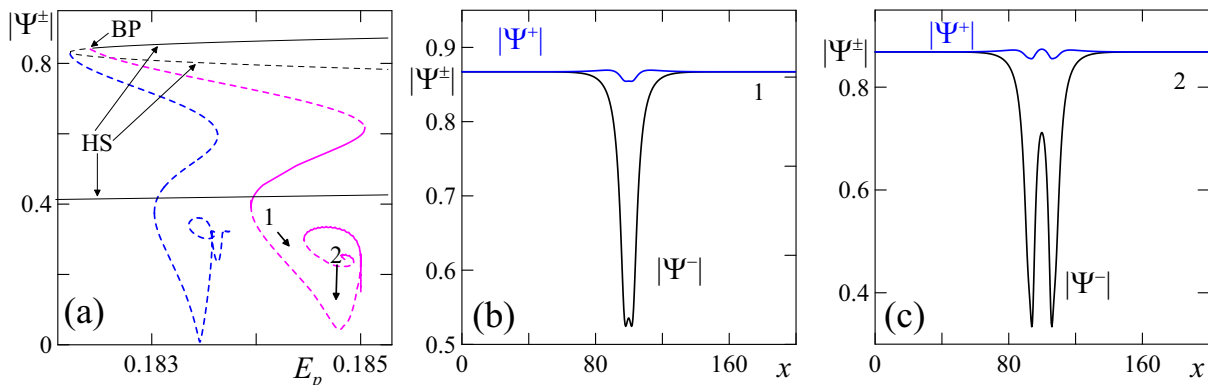
Figure 7.2: Branches and profiles of two-dimensional vectorial dark solitons: (a) Amplitude of symmetric homogeneous states (HSs) in the vicinity of the left folding point of their bistability loop and $\min|\Psi(x,y)^-|$ for dark solitons vs. external pump power E_p, $\rho_{E_p} = 0$, for $\alpha = -0.1$; symmetric states are depicted black (homogeneous) and blue (soliton) whereas the branch of the asymmetric solitons is shown magenta; solid and dashed lines mark stable and unstable solutions, respectively; (b) profile of a stable asymmetric vector soliton for $E_p = 0.1845$ (point 1); (c) profile of a stable higher order asymmetric vector soliton for $E_p = 0.1847$ (point 2).

elliptically polarized holding beam as it was done in Ref. [209], where one-dimensional vector solitons were predicted for $\rho_{E_p} = 0.2$.

A typical profile of a stable soliton is depicted in Fig. 7.2(b). Whereas one polarization (here Ψ^+) develops a fully-fledged dark soliton, the other one differs barely from the upper HS. Thus the total vector soliton is elliptically polarized and therefore termed asymmetric soliton or dark half-soliton according to Refs. [189, 210, 211]. It is evident that both types of dark vector solitons with left- and right- dominant polarization components coexist for the same parameter sets. A similar type of vectorial solitons also arose in the framework of pattern formation, cf. Fig. 6.16 in Sec. 6.2. In that case, a periodic pattern broke up due to bistable frustration which led to the formation of several domains framed by vector solitons. Whereas the focus of that section has been on the dynamics of the domains, we want to have a closer look on the properties of the vectorial solitons in this section. The influence of vectorial effects on the formation of cavity solitons was also studied in a Kerr cavity [212] and in vectorial second harmonic generation [213].

In Sec. 5.2 an analysis describing the bifurcation behavior of asymmetric HSs from symmetric HSs was performed. It culminated in the statement that above a critical value for α (cf. Eq. (5.10)) no asymmetric HSs can exist. The qualitative picture of the bifurcation of the asymmetric localized solutions is similar to the homogeneous case, though, however, the critical value cannot be obtained analytically. Direct numerical simulation of the stationary version of Eqs. (3.4)-(3.5) shows that the branch of asymmetric vector polariton solitons bifurcates from the branch of symmetric solitons for $\alpha < 0.162$. This branch exhibits stable intervals provided that $\alpha < 0.11$. Note that the symmetric and the asymmetric soliton branch coincide if both polarizations are uncoupled ($\alpha = 0$).

For the more realistic value of the coupling parameter $\alpha = -0.1$ [151], the branch of the asymmetric vector cavity polariton solitons emanates from the symmetric HS in the bifurcation point where it becomes unstable against asymmetric perturbations. The modulus of the fields can be obtained by choosing the plus sign in Eq. 5.9. The branch of the asymmetric soliton lies at higher E_p values than the symmetric soliton branch and, more importantly, has a wider stability range. This can be crucial for potential applications as all-optical memory devices. The width of the stability range increases for bigger negative values of α.

Like in the symmetric case, the total soliton branch contains more than one stable subbranch. As the subbranches marked by 1 and 2 in Fig. 7.2(a) are separated in phase space, the corresponding solitons must be topologically different, since they cannot be transformed into one another by, e.g., smoothly varying an external parameter such as E_p. Regarding their respective profiles in Figs. 7.2(b) and (c) indicates this difference quite clearly: whereas the fundamental soliton in Fig. 7.2(b) belonging to subbranch 1 has only one minimum, the soliton in Fig. 7.2(c) belonging to subbranch 2 exhibits two pronounced minima and can therefore be classified as a higher order soliton.

Spatial splitting of linearly polarized solitons

We proceed with the numerical analysis of the soliton dynamics originating from the polarization (or spin) instability of polaritons. The analysis of the steady-state solutions reveals that the entire branch of the symmetric dark soliton is unstable for $\alpha < 0$, cf. Fig. 7.2(a). The dynamical evolution of a symmetric dark cavity polariton soliton is shown in Fig. 7.3. The pump power is chosen $E_p = 0.1837$, which lies in the middle of the symmetric soliton branch. Shortly after the start of the time evolution, the dark soliton formed in E^+ has vanished and the solution has adapted to the surrounding HS. The remaining intensity dip in E^- creates a spot in the polarization degree, cf. 7.3(d). Figures 7.3(b) and (e) show the profiles after another 20 photon lifetimes. The intensity dip in E^- moves outwards radially. Actually, the intensity profiles are rather undulated, cf. 7.3(c) after 70 photon lifetimes. Eventually, they approach the asymmetric HS. Simulations for different values of the pump power reveal, that this dynamic is accelerated by choosing a smaller E_p.

As it was mentioned, a dark vector polariton soliton has a substantial interval of stability and, therefore, becomes a new stable attractor of the system for negative values of the coupling parameter $\alpha < 0$. The dynamical evolution of a symmetric dark cavity polariton soliton is shown in Fig. 7.4 for $\alpha = -0.1$ and $E_p = 0.1845$. The initial intensity profile in Fig. 7.4(a) is formed by two dark solitons in E^+ and E^-. Like in the case discussed above,
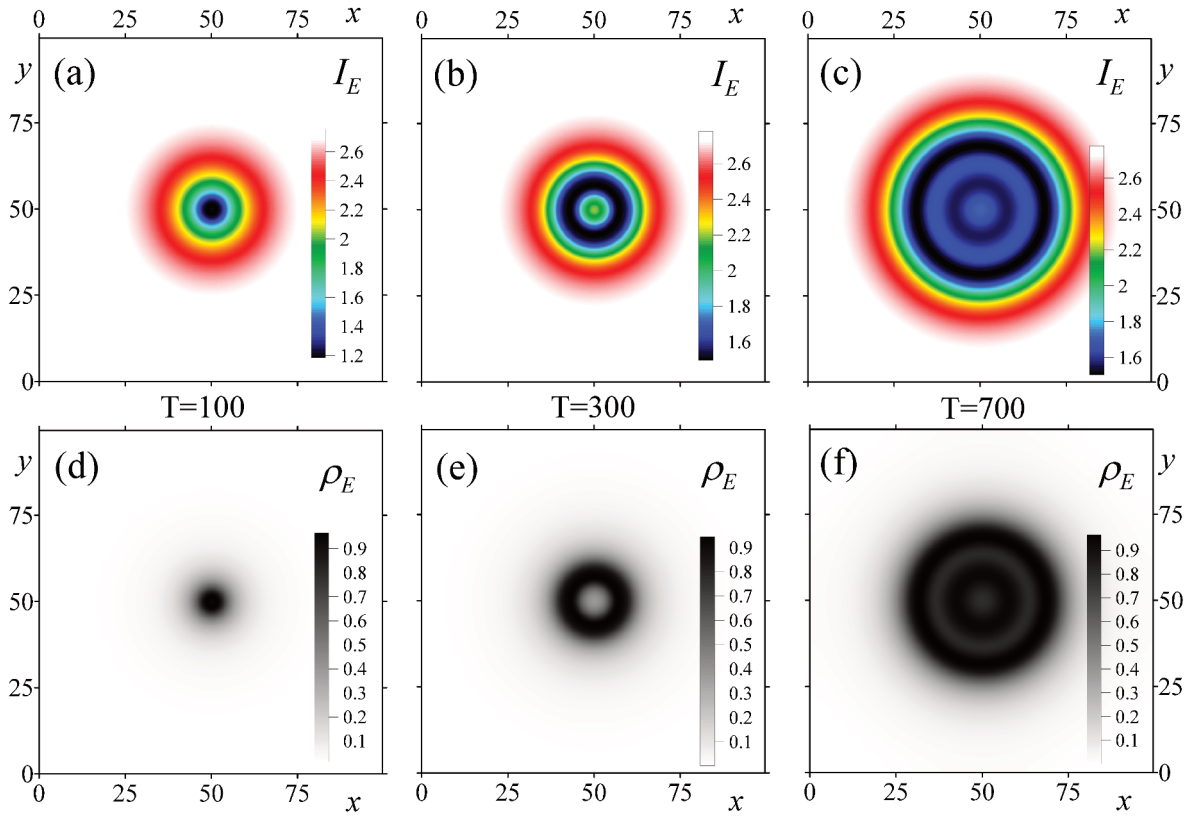
Figure 7.3: Decay of a symmetric dark soliton for $\alpha = -0.1$: (a) $I_E(x,y)$ after 10 photon lifetimes; (b) $I_E(x,y)$ after 30 photon lifetimes; (c) $I_E(x,y)$ after 70 photon lifetimes; (d)-(f) show the respective value of the polarization degree; parameters are chosen $\Delta = -0.7$ and $E_p = 0.1837$.

the soliton in E^- vanishes after about 10 photon lifetimes. The soliton in E^+, however, remains stable for the rest of the time evolution, cf. Figs. 7.4(b) and (c) for the time evolution of a 1D section through the intensity and the polarization degree, respectively. The final intensity profile after 100 photon lifetimes is shown in Fig. 7.4(b). The dip is much less pronounced, since it is only formed by a dark soliton in $E^+(x,y)$, whereas $E^-(x,y)$ has approached the upper symmetric HS.

This behavior changes substantially by choosing α sufficiently close to 0, e.g. $\alpha = -0.05$. In this case, he existence ranges of symmetric and asymmetric cavity polariton solitons is guaranteed and the destructive tendency of the cross-phase modulation term is attenuated. Thus the two components split spontaneously into two asymmetric vector solitons with opposite polaritonic spins, i.e. with the left- and right- elliptical polarization of their centers (cf. Figs. 7.5(a) and (b)). The time evolution of intensity and polarization degree in Figs. 7.5(c) and (d) reveals, that that the dynamics is substantially slower than in the case of $\alpha = -0.1$: It takes about 200 photon lifetimes until the two components start diverging. The final distance of the peaks amounts about 50 μm.
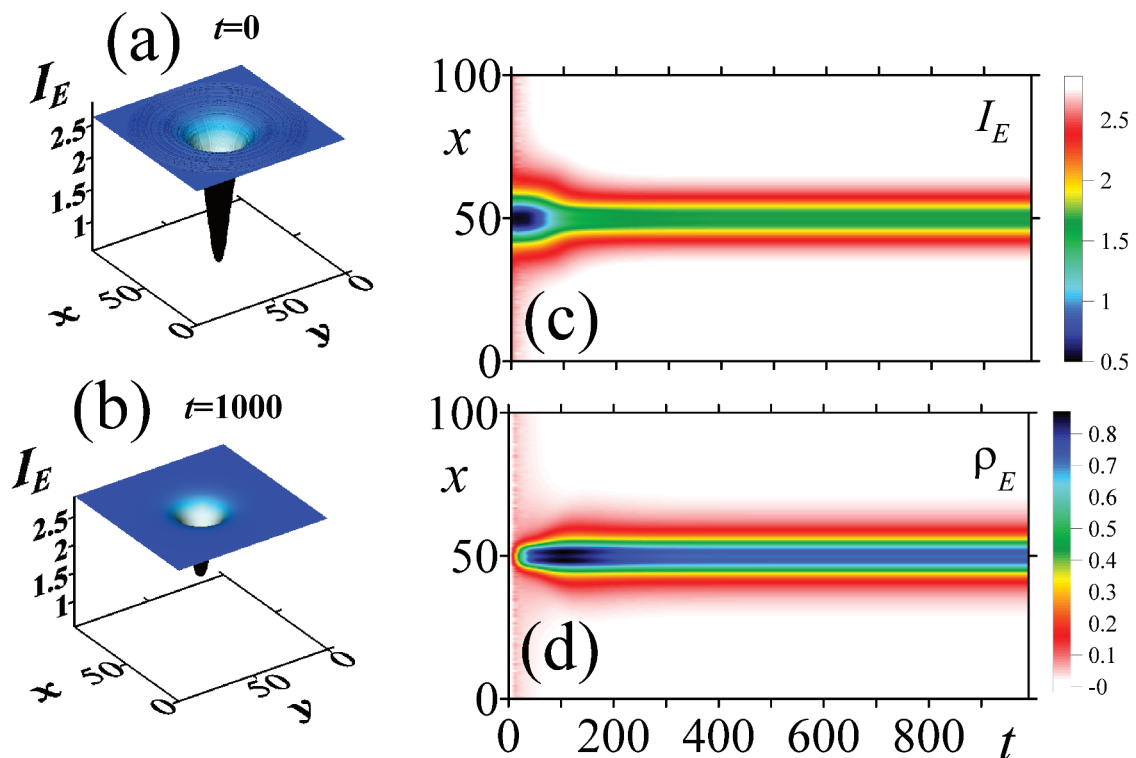
Figure 7.4: Decay of a symmetric dark soliton for $\alpha = -0.1$: (a) initial 2D intensity profile; (b) final 2D intensity profile; (c) time evolution of $I_E(x, y = 0)$; (d) time evolution of $\rho_E(x, y = 0)$; parameters are chosen $\Delta = -0.7$ and $E_p = 0.1845$.

This spontaneous splitting process is actually crucial for the understanding of vectorial pattern formation as it was presented in Sec. 6.2. The initial soliton profile 7.5(a) at $t = 0$ is linearly polarized, cf. Fig. 7.5(d). As we can see from , e.g., Fig. 7.2(a), it belongs to an unstable branch. Thus it can either decay to the HS or each of its components separates spatially from the other. The latter scenario comes to pass for the present choice of parameters. The resulting stationary solution consisting of two vectorial solitons with opposite polarization degree can be compared with the smallest building block of the vectorial patterns displayed in Figs. 6.12 and 6.13. Each of those hexagonal patterns is formed by a left-elliptically polarized vector soliton and a right-elliptically polarized vector soliton represented by the corners of the white and the black hexagon, respectively. Differing from the pure case discussed here, the elements of the various patterns are much closer packed. This is due to the fact that each building block is influenced by all its neighbors so that the spacing between them can be estimated using the analysis from Sec. 5.3, especially Eq. (5.16) and Fig. 5.7(a).
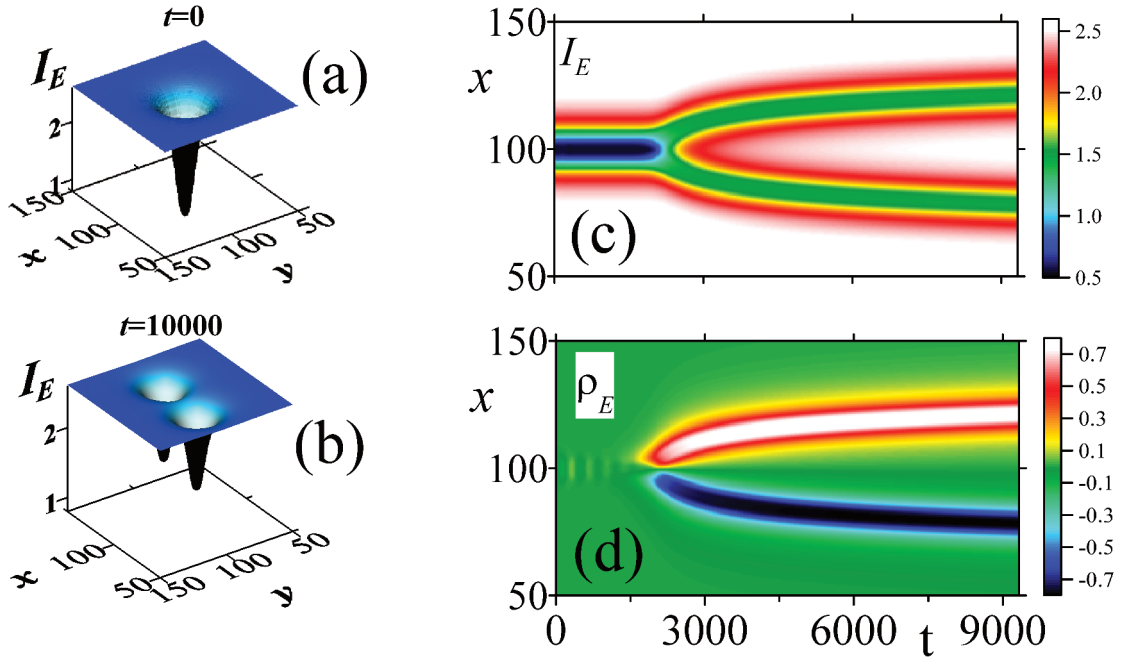
Figure 7.5: A symmetric soliton splits spontaneously into two spatially distinct vector solitons with opposite circular polarization degree, shown here for $\alpha = -0.05$ and $E_p = 0.1786$: (a) initial 2D intensity profile; (b) final 2D intensity profile; (c) temporal evolution of $I_E(x, y = 0)$; (d) temporal evolution of $\rho_E(x, y = 0)$.

Merging of two vector solitons

We have analyzed also the interaction of two vector cavity polariton solitons with different polarizations that are brought close together. It is evident from the splitting dynamics of symmetric dark cavity polariton solitons that two vector dark solitons repel each other provided that their spins have opposite signs or, in other words, their photonic components have opposite elliptical polarizations. By contrast, two asymmetric vector cavity polariton solitons with the same spin signs attract each other and then eventually fuse forming one higher-order cavity polariton soliton provided that the chosen pump power allows it to be stable. The main results of these studies can be seen in Fig. 7.6. A qualitative picture of the radial dependence of each of the initial profiles and the final profile is given in Figs. 7.2(b) and (c), respectively. The fusion process at about 150 photon lifetimes is particularly interesting, since it shows the transition from two simple cylindrically symmetric objects to one cylindrically symmetric object with a richer structure. The fusion of two interacting cavity solitons was also studied in Ref. [95] using a degenerate optical parametrical oscillator. The final bound state is stabilized by coupled internal oscillations and can thus be interpreted as a higher order soliton.
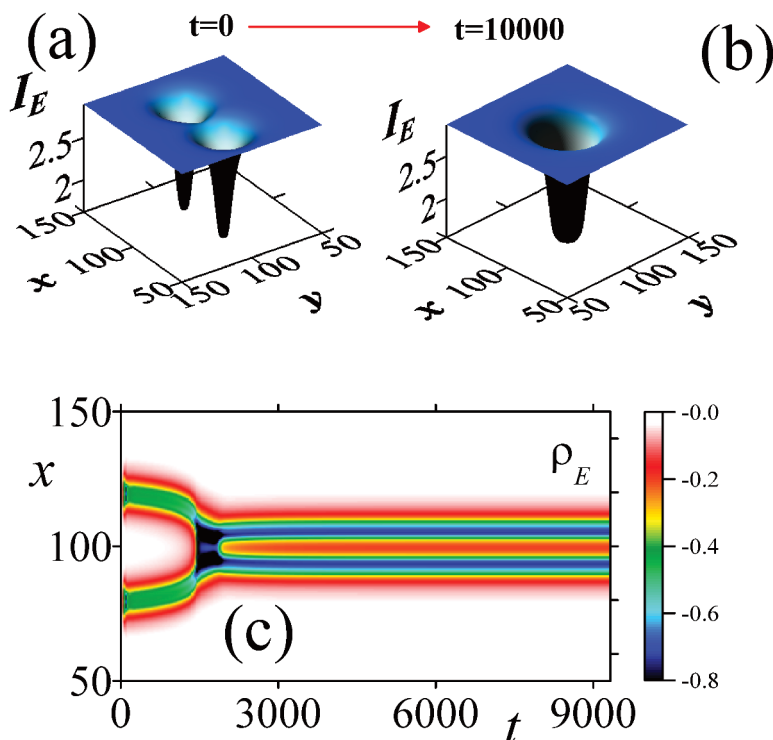
Figure 7.6: Two vector solitons with the same parity merge to one higher-order vector soliton, shown here for $\alpha = -0.1$ and $E_p = 0.1847$: (a) initial 2D intensity profile; (b) final 2D intensity profile; (c) temporal evolution of $\rho(x, y = 0)$; a 1D section through the radially symmetric final profile can be seen in Fig. 7.2(c).

7.2.2. One-dimensional vectorial solitons

In Subsec. 6.2.3, we studied the formation of vectorial patterns within the bistability loop. Instead of being subjected to bistable frustration, the dynamics gave rise to the formation of various large-scale domains. The frames of these domains can be interpreted as dark stripe solitons. Like in the case of two-dimensional solitons, we will study their properties and thereby analyze the stability conditions of the aforementioned domain formation process.

$|\Psi^+|$ and $|\Psi^-|$ of the section through Fig. 6.16(c) are shown in Fig. 7.7(b). Both polarizations nest on the upper branch of the bistability loop. Whereas $|\Psi^+|$ develops a fully-fledged dark soliton, the other polarization $|\Psi^-|$ stays near the HS. Thus, this configuration is a half soliton [189, 211] or vector soliton [165] and is only stable for $\alpha < 0$. Dark solitons are usually created by adequately disturbing the upper branch of the bistability loop [165]. The present simulations show that their attraction range in phase space can also be entered from the modulational instability of its lower branch.

In order to form stable dark vector solitons in this way, it is therefore necessary to choose
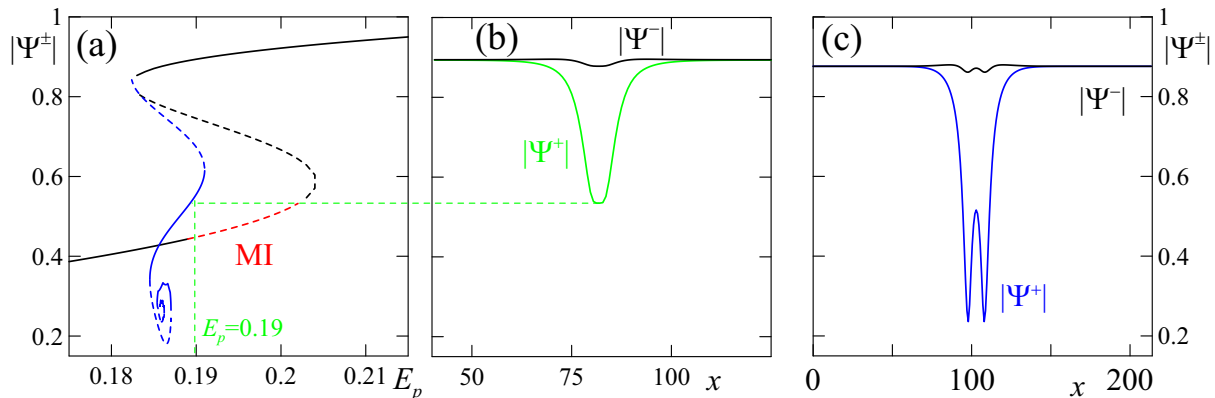
Figure 7.7: Branches and profiles of a one-dimensional dark vector soliton: (a) Amplitude of symmetric homogeneous states (HSs, black lines) in the vicinity of the left folding point of their bistability loop and $\min|\Psi(x,y)^-|$ for one-dimensional dark solitons (blue lines) vs. external pump power E_p, $\rho_{E_p} = 0$, for $\alpha = -0.1$; solid and dashed lines mark stable and unstable solutions, respectively; modulationally unstable HSs are marked with a dashed red line; profile of a stable first-order asymmetric vector soliton for $E_p = 0.19$; (c) profile of a stable higher order asymmetric vector soliton for $E_p = 0.1859$.

a pump power that lies both in the modulationally unstable pump range of the HSs (marked by the red dashed line in Fig. 7.7(a)) and in the stable pump range of these solitons. The branch of the solitons can be determined by means of the Newton-Raphson iterative method. This method allows for the determination of both stable and unstable solutions depicted in Fig. 7.7(a) with bold and dashed blue lines, respectively. It should be noted that the stability range of the one-dimensional soliton is larger than that of the two-dimensional soliton. Figure 7.7(c) shows a higher-order soliton. Like in the two-dimensional case, it can arise from the merging of two attracting first-order solitons.

7.3. Chapter summary and concluding remarks

This chapter is devoted to the study of various aspects of soliton formation in a semiconductor microcavity. These results have been produced by means of extensive direct numerical simulations of the respective equations of motion. The iterative Newton solver was used to double-check the reliability of the obtained results and add yet another facet by offering the possibility to study the whole soliton branches containing not only stable solitons of various orders, but also unstable branches. The HS analysis from Sec. 5.2 gave valuable hints for choosing reasonable detunings and pump powers.

Due to the defocussing nature of the polaritonic nonlinearity the only genuinely stable soliton solutions are one- and two-dimensional dark solitons. In this chapter, we used equations of motion with exciton spin, but without TE-TM splitting. Investigating the

influence of the exciton spin on the formation of dark solitons reveals certain similarities to the afore studied periodic patterns. The crucial parameter is once again the cross-phase modulation parameter α between excitons with different spins. For $\alpha > 0$ the stable soliton solutions are linearly polarized and can thus be reduced to the scalar case investigated in Ref. [170] by scaling all fields with $\sqrt{1 + \alpha}$. Dark solitons bifurcate from the left folding point of the bistability loop. In the case of $\alpha < 0$, however, the spontaneous symmetry breaking favors elliptically polarized vector solitons whose branch and stability range is broadened compared with the respective symmetric soliton branch. After preparing a symmetric soliton one observes its splitting into two spatially distinct vector solitons due to spontaneous symmetry breaking. Whereas two oppositely poled vector solitons repel each other, one can observe an attractive force between two vector solitons with the same polarization degree. The merging of these two vector solitons can eventually lead to the formation of a higher order soliton.

The results obtained for two-dimensional solitons can be transferred to the case of stripe solitons. An important property of these quasi-one-dimensional solitons is there broad stability range. The occurrence of domains arising from pattern formation within the bistability loop can be explained by the overlap of the MI range with the stability range of the one-dimensional vector solitons.

8. Dynamics of one-dimensional domain walls

Like in the preceding chapter, solutions of the spin-dependent equations of motion (2.13)-(2.14) are studied. In Chapt. 7, the existence of bistable symmetric HSs was exploited as a prerequisite for the formation of dark solitons. In the current chapter, we consider the whole set of multistable HSs as it was presented in Sec. 5.2. The coexistence of various different stable HSs at the same pump power allows to study the competition of domains prepared at those HS values and the subsequent behavior of their domain walls. According to Ref. [214], one can distinguish between amplitude domains and phase domains.

Amplitude domains are formed between two nonequivalent domains. The typical behavior of walls between HSs with different amplitude will be studied in Sec. 8.1 for $\alpha > 0$. In this case, its dynamics is dictated by the mere competition between symmetric HSs. Generally, a front connecting two nonequivalent HSs moves in such a way that the more stable state annihilates the other. The pump power, where both domains could be linked by a stationary wall, is called *Maxwell point* (MWP).

For $\alpha < 0$, however, this typical behavior is overpowered by the formation of stable elliptically polarized domains, cf. Sec. 8.2. Once again, there are no stationary domain walls between the nonequivalent states.

The discrete symmetry of the vectorial equations under permutation of $+$ and $-$ fields allows for the construction of equivalent states, i.e., two states with the same intensity but opposite polarization degree. In the terminology of Ref. [214] they are called *phase domains*. Due to the discrete symmetry between the two domains, a front between them is generally expected to be at rest. However, this stationary system can be destabilized in favor of a pair two counterpropagating fronts when it reaches a bifurcation point by tuning a system parameter such as the pump power. The transition from a resting to a moving front is called Ising-Bloch transition [215–218]. It was described in many different physical systems such as liquid crystals [219, 220], anisotropic ferromagnets [221], and semiconductor etalons [222]. Also in systems being far from equilibrium the aforementioned symmetry can be preserved which leads to pairs of equivalent solutions. However, the force acting on a front can be nonzero. A common denotation for the underlying bifurcation is nonequilibrium Ising-Bloch (NIB) transition. It has been observed in many systems

including reaction-diffusion systems [216–218], optical parametric oscillators [223], systems described by the complex parametrically driven Ginzburg-Landau equation [215], and in second harmonic generation [224]. A universal criterion for the onset of a NIB transition was shown in Ref. [224] using the fact that a bifurcation from a resting solitary wave to a moving one has to be linked to the onset of the translational mode.

The results presented in this chapter have not been published yet.

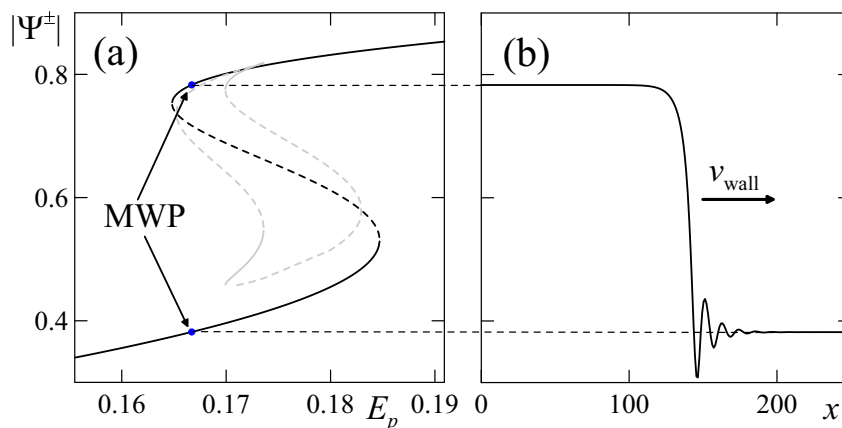## 8.1. Moving domain walls between linearly polarized domains for $\alpha > 0$

Figure 8.1: Domain walls for $\alpha = 0.1$: (a) Amplitude of symmetric (black) and asymmetric (gray) homogeneous states (HSs); solid and dashed lines denote stable and unstable solutions, respectively; MWP denotes the Maxwell point of the symmetric HSs at $E_p = 0.16665$; (b) Profile of a moving domain wall $|\Psi^{\pm}|$ at $E_p = 0.1667$. The detunings are chosen $\Delta = -0.7$.

In the scalar case [170] according to Eqs. (2.13)-(2.14) there is exactly one E_p value, where the upper and the lower HS in bistability can be connected by a stationary 1D front. This E_p value is the Maxwell point. The occurrence of a standing 1D front between the upper and lower symmetric HS can also be observed in the vectorial case for $\alpha > 0$. The value E_{MWP} of the pump at the MWP is calculated by scaling the scalar MWP with $\sqrt{1 + \alpha}$. It is marked with a blue dot in Fig. 8.1(a). For $E_p > E_{\mathrm{MWP}}$, the movement of the domain wall causes the spatial broadening of the upper HS at the expense of the lower HS, cf. Fig. 8.1(b). On the other hand, for $E_p < E_{\mathrm{MWP}}$, the movement of the domain wall will be reversed thus leading to the expansion of the lower HS. It is impossible to construct a stationary domain wall, since its existence conditions have to be met with arbitrary precision. This fact agrees with the general statement that it is impossible to build a stationary wall between two nonequivalent states.

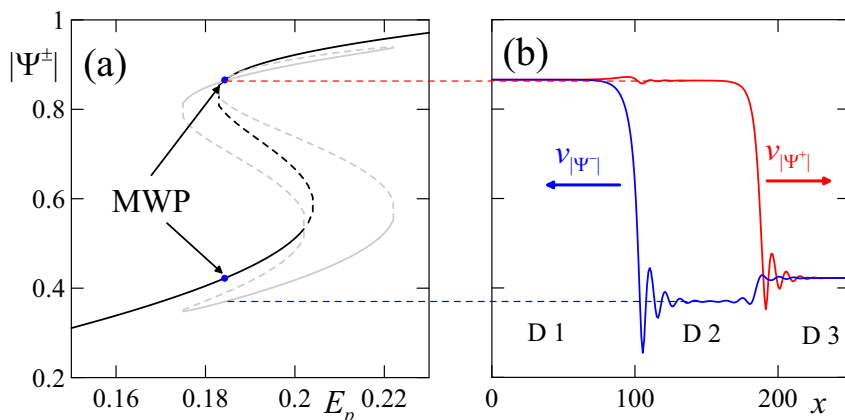## 8.2. Formation of elliptically polarized domains for $\alpha < 0$

Figure 8.2: Domain walls for $\alpha = -0.1$: (a) Amplitude of symmetric (black) and asymmetric (gray) homogeneous states (HSs); solid and dashed lines denote stable and unstable solutions, respectively; MWP denotes the calculated value of the Maxwell point of the symmetric HSs at $E_p = 0.1843$; (b) Profiles of diverging domain walls for $|\Psi^+|$ (red) and $|\Psi^-|$ (blue) at $E_p = 0.1843$; D1 (D3) shows the domain of the upper (lower) symmetric HS, the domain of the asymmetric HS is denoted with D2. The detunings are chosen $\Delta = -0.7$.

For $\alpha < 0$ the scaled MWP lies at a point where stable symmetric HSs and asymmetric HSs compete, cf. the case $\alpha = -0.1$ in Fig. 8.2(a). We showed for dark solitons (cf. Ref. [165] and Sec. 7.2) and hexagonal patterns (cf. Ref. [164] and Sec. 6.2) that the negative α is responsible for a spontaneous symmetry breaking mechanism leading to the destabilization of symmetric solutions in favor of asymmetric solutions. The same holds here for the case of domain walls. An initially prepared configuration consisting of a domain wall between upper symmetric HS (denoted with D1 in Fig. 8.2(b)) and lower symmetric HS (denoted with D3 in Fig. 8.2(b)) destabilizes. The result of these diverging domain walls is a stable domain formed by asymmetric HSs and denoted with D2 in Fig. 8.2(b). This instability of the initial configuration is not foremost due to the competition between two nonequivalent states but because of the predominance of asymmetric HSs.

8.3. Nonequilibrium Ising-Bloch transition for elliptically polarized domains

Having stated in the former section that the stable HSs for $\alpha < 0$ are asymmetric ($\rho_\Psi \neq 0$), we proceed with a survey of one-dimensional domains formed by asymmetric HSs and the dynamics of the walls between these domains. Unlike the solutions discussed so far, the domains have the same intensity and differ only in (the sign of) their polarization degree. Thus they are equivalent and called phase domains in the terminology of Ref. [214].
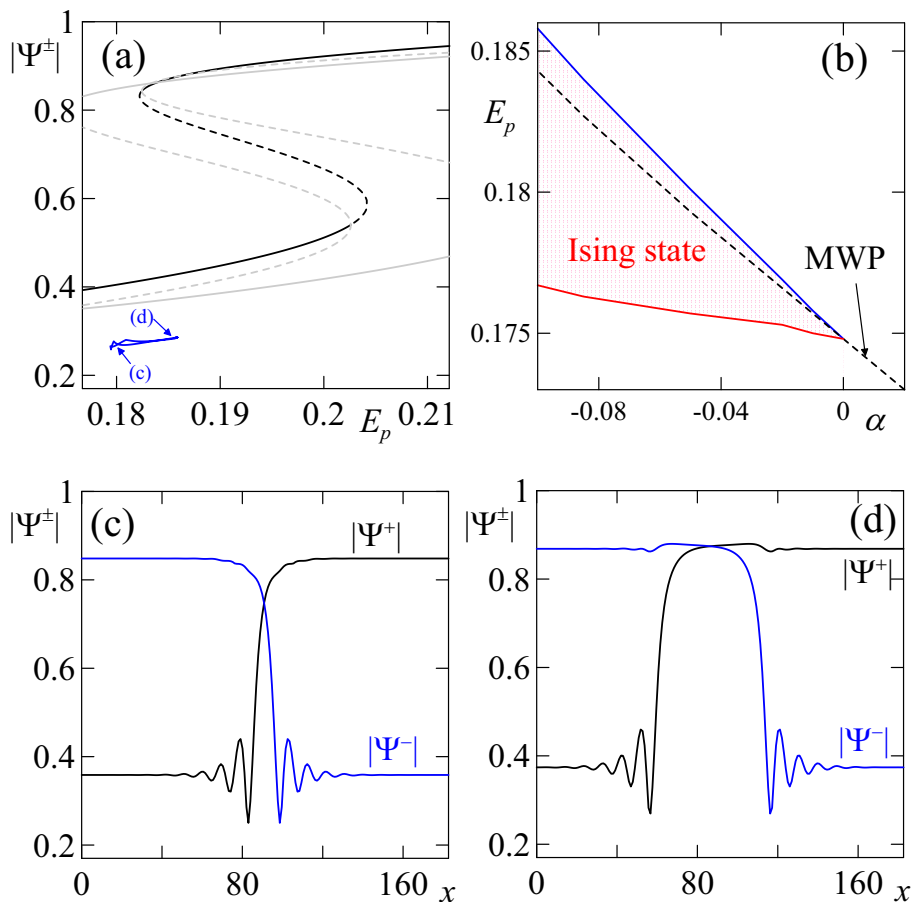
Figure 8.3: Nonequilibrium Ising-Bloch transition: (a) black (gray) lines show the amplitude of symmetric (asymmetric) HSs; solid and dashed lines denote stable and unstable solutions, respectively; dark blue lines: $\min|\Psi^{\pm}|$ of the Ising wall; (b) dotted area: pump range of stationary phase domain walls as a function of α; dashed black line: scaled Maxwell points for the competition of upper and lower symmetric HS; (c) perfect Ising wall for $E_p = 0.18$; (d) broadened domain wall for $E_p = 0.18586$; parameters are chosen $\alpha = -0.1$ and $\Delta = -0.7$.

An example of a stationary wall between two equivalent states is shown in Fig. 8.3(c) for $E_p = 0.18$. The full stability range of the bound states for $\alpha = -0.1$ reaches from $E_p = 0.1767$ to 0.1859 (cf. blue line $\min|\Psi^+|$ in Fig. 8.3(a)), its dimension is thus comparable to that of the scalar bright soliton [100]. This is exactly the pump range where the asymmetric HS wins the competition with the symmetric HSs as described in the preceding section. According to the terminology in Refs. [96, 224] the resting fronts of this bound state can be denoted as Ising fronts. While increasing the pump power, one observes that the hitherto spatially confined domain wall has become a spatially extended transition domain, cf. Fig. 8.3(d) at $E_p = 0.18586$. For $E_p > 0.1859$ the two walls lose cohesion and move in opposite directions. This formation of Bloch walls indicates the onset of the NIB transition. On the other hand, below $E_p = 0.1767$ the bound state destabilizes in favor of the lower branch of the bistable symmetric HSs.

Since the cross-phase modulation parameter α being negative is a necessary condition

for the relative stability of asymmetric HSs in comparison with symmetric HSs, it seems worthwhile to analyze its influence on the width of the stability range of Ising walls quantitatively. Therefore we determined the dependence of the NIB transition on α both with the static Newton-Raphson solver and by directly simulating the equations of motion. The results are shown in Fig. 8.3(b). For $\alpha > 0$ there are no Ising walls since the asymmetric HSs always destabilize in favor of symmetric HSs whose movement is then dictated by the relative value of the pump power compared with the scaled Maxwell point. For $\alpha < 0$, however, there is a pump range where stable Ising walls exist, cf. the dotted area in Fig. 8.3(b). This range originates at the Maxwell point for $\alpha = 0$ and gets broader when $-\alpha$ is increased. Therefore $\alpha = 0$ is the bifurcation point of a NIB transition supported by the stability of asymmetric HSs for $\alpha < 0$.

8.4. Chapter summary and concluding remarks

This chapter concludes the study of spatially nonuniform solutions that can form in the transverse plane of the polaritonic microcavity by giving a thorough investigation of one-dimensional domain walls in a polaritonic system with spin. We determined the Maxwell point for domain walls between domains formed by lower and upper branch of the bistability loop, respectively, for positive values of the parameter α. For $\alpha < 0$ we observed the typical transition to elliptically polarized stable solutions. The asymmetric HSs prove to be suitable for the construction of equivalent domains, i.e., domains with equal intensity but opposite polarization degree which are termed phase domains. These domain walls have a broad stability range. The transition from stationary (Ising) to moving (Bloch) walls is observed at the upper boundary of the stable pump range. Since these solutions can only be stable for negative values of α, we identify $\alpha = 0$ as a bifurcation point of a nonequilibrium Ising-Bloch transition.

9. Summary

In this thesis we investigated the nonlinear dynamics of exciton-polaritons in a coherently pumped semiconductor microcavity both analytically and numerically. Our efforts aimed at exploiting the peculiarities of exciton-polaritons which are based on their hybrid nature. For that, the wave-particle dualism of these quasi-particles can also be highlighted. Depending on the choice of parameters (mainly detunings and pump inclination) the main features of the polaritons can be both excitonic which corresponds to spatial localization or photon-like expressed by a wave-like behavior.

Our main focus was put on the investigation of effects originating from the exciton spin whose strong coupling to left and right circularly polarized cavity photons leads to the rare case of a bosonic two-level system.

The splitting between TE- and TM polarized cavity modes provides a linear interaction mechanism for polaritons with opposite pseudospin. It competes with the nonlinear contribution to the Coulomb interaction between two excitons with opposite pseudospin. The interplay of these two different mechanism also reveals the hybrid quantum nature of exciton-polaritons. This work contains a comprehensive theoretical study of the polariton pseudospin of unprecedented depth making use of various solutions of the equations of motion and their interplay.

The solutions of the equations of motion which were studied in order to highlight the various properties of exciton-polaritons include homogeneous solutions (HSs), dark cavity solitons, spatially periodic patterns, and domain walls between different HSs. Due to the Kerr-like nonlinearity, one can achieve bistability of the linearly polarized HSs by properly detuning the pump frequency against the excitonic resonance. The bifurcation of multistable elliptically polarized HSs at a critical value of the cross-phase modulation parameter α according to Eq. (5.10) constitutes the importance of genuine effects originating from the exciton spin.

A prototypic example of a nonlinear effect is the spontaneous formation of spatially periodic patterns. We used it as a working horse to exemplify the influence of all tunable parameters of the system and the arising effects. We concentrated on the lower polariton branch which is distinguished by its unique shape thus offering different regimes of pattern formation which can be triggered by the choice of the detuning from the excitonic resonance. The arising patterns can be compared with those arising from the Lugiato-Lefever model

which describes a cavity with Kerr nonlinearity. Actually, near the bottom of the lower polariton branch the dispersion relation is approximately parabolic. Thus the effective model in this parameter range can be approximated by a self-defocussing Kerr cavity and the arising polariton patterns are similar to the well-known hexagonal patterns in a Kerr cavity. Contrary to the self-defocussing Kerr cavity one can achieve a pattern forming instability without having bistable HSs by approaching the excitonic resonance. This offers the possibility to observe pattern formation over the whole modulationally unstable range without bistable frustration. Slightly above the linear excitonic resonance a link to soliton physics arises when the hitherto periodic patterns break up into a gas of breathing solitons. We interpret this localization as a manifestation of the particle nature of polaritons near the excitonic resonance.

The spin degree of freedom allows for the formation of vectorial polariton patterns consisting of two spatially shifted patterns in the respective polarizations. The spontaneous formation of an elliptically polarized total field despite being pumped by a linearly polarized holding beam adds another evidence to the importance of effects originating from the exciton spin. This spatial shift is by no means unique for periodic patterns, since we also observed it in the framework of dark solitons where a linearly polarized soliton experiences a spontaneous splitting into two spatially distinct elliptically polarized vectorial solitons.

Additionally taking into account the linear coupling of left and right polarization originating from the TE-TM splitting of the cavity modes sets the entire pattern into a uniform motion in the plane of the resonator. Similar to the optical spin Hall effect, this drift is induced by the directionally dependent pseudospin precession of polaritons. The moving direction is imprinted by the line connecting the two shifted polarization patterns. It should be noted that this shift is required such that each polarization is driven by the other one. This motion can also be witnessed in a purer fashion by preparing a molecule consisting of two vectorial solitons with opposite polarization degree in close spatial vicinity. This configuration results in a spontaneous motion of the entire molecule, since each soliton is driven by the other one. Thus these phenomena are generic and can be expected to occur in other nonlinear systems with a spin-orbit interaction mechanism.

Besides dark solitons and vectorial patterns, the spin degree of freedom allows the formation of domain walls between asymmetric HSs with opposite polarization degree. Since these domains have equal intensity they allow for a transition from stationary (Ising) to moving (Bloch) walls. This nonequilibrium Ising-Bloch transition is observed at $\alpha = 0$. The existence of a broad pump range of stable one-dimensional Ising walls for, e.g., $\alpha = -0.1$ makes exciton-polaritons a possible candidate for future optical information processing devices.

A general and well-known feature of many nonlinear systems is the existence of bistable HSs as a prerequisite for dark solitons as well as the coexistence of stable HS and subcritically bifurcating pattern as a prerequisite for existence of bright solitons. However, in the case of exciton-polaritons there are several more links between the different types of solutions which have been highlighted throughout this work. Besides the already mentioned link between patterns and the formation of domains framed by dark solitons, there is another relationship between patterns and solitons: Near the excitonic resonance periodic patterns break up and form a gas of breathing solitons. This unveils a characteristic link between spatially extended and spatially confined solutions caused by the influence of the excitonic resonance.

Bibliography

[1] J. Fraunhofer, "Bestimmung des Brechungs- und des Farbenzerstreungs-Vermögens verschiedener Glasarten, in Bezug auf die Vervollkommnung achromatischer Fernröhre," Annalen der Physik **56**, 264 (1817).

[2] F. Koyoma, "Recent Advances of VCSEL Photonics," IEEE Journal of Lightwave Electronics **24**, 4502 (2006).

[3] A. V. Kavokin, J. J. Baumberg, G. Malpuech, and F. P. Laussy, "Microcavities" (Oxford University Press, Oxford 2007).

[4] H. M. Gibbs, "Optical Bistability: Controlling Light with Light," Academic Press, Orlando (1985).

[5] N. Akhmediev and A. Ankiewicz, "Dissipative Solitons," Lecture Notes in Physics, Springer, Berlin (2005).

[6] T. Ackemann, W. J. Firth, and G.-L. Oppo, "Fundamentals and Applications of Spatial Dissipative Solitons in Photonic Devices," Advances in Atomic, Molecular, and Optical Physics **57**, 324 (2009).

[7] V. E. Zakharov and L. A. Ostrovsky, "Modulation instability: The beginning," Physica D **238**, 540 (2009).

[8] P. Manneville, "Dissipative Structures and Weak Turbulence," Academic Press, San Diego, London (1995).

[9] P. Manneville, "Instabilities, Chaos and Turbulence," 2nd ed., Imperial College Press, London (2010).

[10] R. Hoyle, "Pattern Formation - An introduction to methods," Cambridge Univ. Press (2006).

[11] M. C. Cross and P. C. Hohenberg, "Pattern formation outside of equilibrium," Rev. Mod. Phys. **65**, 851 (1993).

[12] C. Weisbuch, M. Nishioka, A. Ishikawa, and Y. Arakawa, "Observation of the Coupled Exciton-Photon Mode Splitting in a Semiconductor Quantum Microcavity," Phys. Rev. Lett. **69**, 3314 (1992).

[13] M. Fox, "Quantum Optics - An Introduction," Oxford Univ. Press, Oxford (2006).

[14] R. Balili, V. Hartwell, D. Snoke, L. Pfeiffer, and K. West, "Bose-Einstein Condensation of Microcavity Polaritons in a Trap," Science **316**, 1007 (2007).

[15] H. Deng, G. Weihs, D. Snoke, J. Bloch, and Y. Yamamoto, "Polariton lasing vs. photon lasing in a semiconductor microcavity," Science **298**, 199 (2002).

[16] M. Richard, J. Kasprzak, R. André, R. Romestain, Le Si Dang, G. Malpuech, and A. Kavokin, "Experimental evidence for nonequilibrium Bose condensation of exciton polaritons," Phys. Rev. B **72**, 201301(R) (2005).

[17] Y. G. Rubo, "Half Vortices in Exciton Polariton Condensates," Phys. Rev. Lett. **99**, 106401 (2007).

[18] J. Kasprzak, R. Andr'e, Le Si Dang, I. A. Shelykh, A. V. Kavokin, Y. G. Rubo, K. V. Kavokin, and G. Malpuech, "Build up and pinning of linear polarization in the Bose condensates of exciton polaritons," Phys. Rev. B **75**, 045326 (2007).

[19] S. Christopoulos, G. Baldassarri Höger von Högersthal, A. J. D. Grundy, P. G. Lagoudakis, A. V. Kavokin, J. J. Baumberg, G. Christmann, R. Butté, E. Feltin, J.-F. Carlin, and N. Grandjean, "Room-Temperature Polariton Lasing in Semiconductor Microcavities," Phys. Rev. Lett. **98**, 126405 (2007).

[20] B. Deveaud-Plédran, "On the condensation of polaritons," J. Opt. Soc. Am. B **29**, A138 (2012).

[21] D. D. Solnyshkov, H. Flayac, and G. Malpuech, "Stable magnetic monopoles in spinor polariton condensates," Phys. Rev. B **85**, 073105 (2012).

[22] D. D. Solnyshkov, I. A. Shelykh, N. A. Gippius, A. V. Kavokin, and G. Malpuech, "Dispersion of interacting spinor cavity polaritons out of thermal equilibrium," Phys. Rev. B **77**, 045314 (2008).
[23]

[23] D. Sanvitto, A. Amo, F. P. Laussy, A. Lemaître, J. Bloch, C. Tejedor, and L. Viña, "Polariton condensates put in motion," Nanotechnology **21**, 134025 (2010).

[24] I. Carusotto, and C. Ciuti, "Probing Microcavity Polariton Superfluidity through Resonant Rayleigh Scattering," Phys. Rev. Lett. **93**, 166401 (2004).

[25] A. Amo, D. Sanvitto, F. P. Laussy, D. Ballarini, E. del Valle, M. D. Martin, A. Lemaître, J. Bloch, D. N. Krizhanovskii, M. S. Skolnick, C. Tejedor, and L. Viña, "Collective fluid dynamics of a polariton condensate in a semiconductor microcavity," Nature **457**, 291 (2009).

[26] A. Amo, S. Pigeon, D. Sanvitto, V. G. Sala, R. Hivet, I. Carusotto, F. Pisanello, G. Leménager, R. Houdré, E. Giacobino, C. Ciuti, and A. Bramati, "Polariton Superfluids Reveal Quantum Hydrodynamic Solitons," Science **332**, 1167 (2011).

[27] H. Terças, H. Flayac, D. D. Solnyshkov, and G. Malpuech, "Non-Abelian Gauge Fields in Photonic Cavities and Photonic Superfluids," Phys. Rev. Lett. **112**, 066402 (2014).

[28] E. A. Ostrovskaya, J. Abdullaev, A. S. Desyatnikov, M. D. Fraser, and Y. S. Kivshar, "Dissipative solitons and vortices in polariton Bose-Einstein condensates," Phys. Rev. A **86**, 013636 (2012).

[29] V. Ardizzone, P. Lewandowski, M. H. Luk, Y. C. Tse, N. H. Kwong, A. Lücke, M. Abbarchi, E. Baudin, E. Galopin, J. Bloch, A. Lemaître, P. T. Leung, P. Roussignol, R. Binder, J. Tignon, and S. Schumacher, "Formation and control of Turing patterns in a coherent quantum fluid," Scientific Reports **3**, 3016 (2013).

[30] H. Saito, T. Aioi, and T. Kadokura, "Order-Disorder Oscillations in Exciton-Polariton Superfluids," Phys. Rev. Lett. **110**, 026401 (2013).

[31] H. Flayac, I. A. Sehlykh, D. D. Solnyshkov, and G. Malpuech, "Topological stability of the half-vortices in spinor exciton-polariton condensates," Phys. Rev. B **81**, 045318 (2010).

[32] K. G. Lagoudakis, T. Ostatnický, A. V. Kavokin, Y. G. Rubo, R. André, and B. Deveaud-Plédran, "Observation of Half-Quantum Vortices in an Exciton-Polariton Condensate," Science **326**, 974 (2009).

[33] M. O. Borgh, J. Keeling, and N. G. Berloff, "Spatial pattern formation and polarization dynamics of a nonequilibrium spinor polariton condensate," Phys. Rev. B **81**, 235302 (2010).

[34] X. Ma, I. Yu. Chestnov, M. V. Charukhchyan, A. P. Alodjants, and O. A. Egorov, "Oscillatory dynamics of nonequilibrium dissipative exciton-polariton condensates in weak-contrast lattices," Phys. Rev. B **91**, 214301 (2015).

[35] G. Li, T. C. H. Liew, O. A. Egorov, and E. A. Ostrovskaya, "Incoherent excitation and switching of spin states in exciton-polariton condensates," Phys. Rev. B **92**, 064304 (2015).

[36] F. Manni, K. G. Lagoudakis, T. C. H. Liew, R. André, and B. Deveaud-Plédran, "Spontaneous Pattern Formation in a Polariton Condensate," Phys. Rev. Lett. **107**, 106401 (2011).

[37] T. Gao, P. S. Eldridge, T. C. H. Liew, S. I. Tsintzos, G. Stavrinidis, G. Deligeorgis, Z. Hatzopoulos, and P. G. Savvidis, "Polariton condensate transistor switch," Phys. Rev. B **85**, 235102 (2012).

[38] H. Sigurdsson, O. A. Egorov, X. Ma, I. A. Shelykh, and T. C. H. Liew, "Information processing with topologically protected vortex memories in exciton-polariton condensates," Phys. Rev. B **90**, 014504 (2014).

[39] A. Tredicucci, Y. Chen, V. Pellegrini, M. Börger, and F. Bassani, "Optical bistability of semiconductor microcavities in the strong-coupling regime," Phys. Rev. A **54**, 3492 (1996).

[40] A. Baas, J. Ph. Karr, H. Eleuch, and E. Giacobino, "Optical bistability in semiconductor microcavities," Phys. Rev. A **69**, 023809 (2004).

[41] D. N. Krizhanovskii, S. S. Gavrilov, A. P. D. Love, D. Sanvitto, N. A. Gippius, S. G. Tikhodeev, V. D. Kulakovskii, D. M. Whittaker, M. S. Skolnick, and J. S. Roberts, "Self-organization of multiple polariton-polariton scattering in semiconductor microcavities," Phys. Rev. B **77**, 115336 (2008).

[42] O. Kyriienko, E. A. Ostrovskaya, O. A. Egorov, I. A. Shelykh, and T. C. H. Liew, "Bistability in microcavities with incoherent optical or electrical excitation," Phys. Rev. B **90**, 125407 (2014).

[43] N. A. Gippius, S. G. Tikhodeev, V. D. Kulakovskii, D. N. Krizhanovskii, and A. I. Tartakovskii, "Nonlinear dynamics of polariton scattering in semiconductor microcavity: Bistability vs. stimulated scattering," Europhys. Lett. **67**, 997 (2004).

[44] C. Diederichs, J. Tignon, G. Dasbach, C. Ciuti, A. Lemaître, J. Bloch, P. Roussignol, and C. Delalande, "Parametric oscillation in vertical triple microcavities," Nature (London) **440**, 904 (2006).

[45] P. G. Savvidis, J. J. Baumberg, R. M. Stevenson, M. S. Skolnick, D. M. Whittaker, and J. S. Roberts, "Angle-Resonant Stimulated Polariton Amplifier," Phys. Rev. Lett. **84**, 1547 (2000).

[46] R. M. Stevenson, V. N. Astratov, M. S. Skolnick, D. M. Whittaker, M. Emam-Ismail, A. I. Tartakovskii, P. G. Savvidis, J. J. Baumberg, and J. S. Roberts, "Continuous Wave Observation of Massive Polariton Redistribution by Stimulated Scattering in Semiconductor Microcavities," Phys. Rev. Lett. **85**, 3680 (2000).

[47] C. Ciuti, P. Schwendimann, and A. Quattropani, "Theory of polariton parametric interactions in semiconductor microcavities," Semicond. Sci. Technol. **18**, 279 (2003).

[48] Ye. Larionova, C. O. Weiss, and O. Egorov, "Dark solitons in semiconductor resonators," Opt. Express **13**, 8308 (2005).

[49] U. Bortolozzo and S. Residori, "Storage of Localized Structure Matrices in Nematic Liquid Crystals," PRL **96**, 037801 (2006).

[50] F. Leo, S. Coen, P. Kockaert, S.-P. Gorza, P. Emplit, and M. Haelterman, "Temporal cavity solitons in one-dimensional Kerr media as bits in an all-optical buffer," Nat. Photonics **4**, 471 (2010).

[51] A. Jacobo, D. Gomila, M. A. Matías, and P. Colet, "Logical operations with localized structures," New J. Phys **14**, 013040 (2012).

[52] D. Ballarini, M. De Giorgi, E. Cancellieri, R. Houdré, E. Giacobino, R. Cingolani, A. Bramati, G. Gigli, and D. Sanvitto, "All-optical polariton transistor," Nature Commun. **4**, 1778 (2013).

[53] I. Shelykh, K. V. Kavokin, A. V. Kavokin, G. Malpuech, P. Bigenwald, H. Deng, G. Weihs, and Y. Yamamoto, "Semiconductor microcavity as a spin-dependent optoelectronic device," Phys. Rev. B **70**, 035320 (2004).

[54] T. C. H. Liew, I. A. Shelykh, and G. Malpuech, "Polaritonic devices," Physica E **43**, 1543 (2011).

[55] S. Barland, J. R. Tredicce, M. Brambilla, L. A. Lugiato, S. Balle, M. Giudici, T. Maggipinto, L. Spinelli, G. Tissoni, T. Knödl, M. Miller, and R. Jäger, "Cavity solitons as pixels in semiconductor microcavities," Nature (London) **419**, 699 (2002).

[56] F. Pedaci, S. Barland, E. Caboche, P. Genevet, M. Giudici, J. R. Tredicce, T. Ackemann, A. J. Scroggie, W. J. Firth, G.-L. Oppo, G. Tissoni, and R. Jäger, "All-optical delay line using semiconductor cavity solitons," Appl. Phys. Lett. **92**, 011101 (2008).

[57] G. Malpuech, A. Kavokin, A. Di Carlo, and J. J. Baumberg, "Polariton lasing by exciton-electron scattering in semiconductor microcavities," Phys. Rev. B **65**, 153310 (2002).

[58] G. Malpuech, Y. G. Rubo, F. P. Laussy, P. Bigenwald, and A. V. Kavokin, "Polariton laser: thermodynamics and quantum kinetic theory," Semicond. Sci. Technol. **18**, S395 (2003).

[59] H. Deng, G. Weihs, D. Snoke, J. Bloch, and Y. Yamamoto, "Polariton lasing vs. photon lasing in a semiconductor microcavity," Proc. Natl. Acad. Sci. U.S.A. **100**, 15318 (2003).

[60] J. J. Baumberg, A. V. Kavokin, S. Christopoulos, A. J. D. Grundy, R. Butté, G. Christmann, D. D. Solnyshkov, G. Malpuech, G. Baldassarri Höger von Högersthal, E. Feltin, J.-F. Carlin, and N. Grandjean, "Spontaneous Polarization Buildup in a Room-Temperature Polariton Laser," Phys. Rev. Lett. **101**, 136409 (2008).

[61] W. Firth and C. Paré, "Transverse modulational instabilities for counterpropagating beams in Kerr media," Opt. Lett. **13**, 1096 (1988).

[62] J. Y. Courtois and G. Grynberg, "Spatial pattern formation for counterpropagating beams in a Kerr medium: a simple model," Opt. Comm. **87**, 186 (1992).

[63] G. D'Alessandro and W. J. Firth, "Spontaneous Hexagon Formation in a Nonlinear Optical Medium with Feedback Mirror," Phys. Rev. Lett. **66**, 2597 (1991).

[64] G. D'Alessandro and W. J. Firth, "Hexagonal spatial patterns for a Kerr slice with a feedback mirror," Phys. Rev. A **46**, 537 (1992).

[65] M. Tlidi, R. Lefever, and P. Mandel, "Pattern selection in optical bistability," Quantum Semiclass. Opt. **8**, 931 (1996).

[66] J. B. Geddes, J. Lega, J. V. Moloney, R. A. Indik, E. M. Wright, and W. J. Firth, "Pattern Selection in Passive and Active Nonlinear Optical Systems," Chaos, Solitons and Fractals **4**, 1261 (1994).

[67] F. T. Arecchi, S. Boccaletti, P. L. Ramazza, "Pattern formation and competition in Nonlinear optics," Phys. Rep. **318**, 1 (1999).

[68] S. Ciliberto, P. Coullet, J. Lega, E. Pampaloni, and C. Perez-Garcia, "Defects in Roll-Hexagon Competition," Phys. Rev. Lett. **65**, 2370 (1990).

[69] A. J. Scroggie, D. Gomila, W. J. Firth, and G.-L. Oppo, "Spontaneous and induced motion of optical patterns," Appl. Phys. B **81**, 963 (2005).

[70] G. J. de Valcárcel and K. Staliunas, "Phase-bistable Kerr cavity solitons and patterns," Phys. Rev. A **87**, 043802 (2013).

[71] E. Tesio, G. R. M. Robb, T. Ackemann, W. J. Firth, and G.-L. Oppo, "Spontaneous optomechanical pattern formation in cold atoms," Phys. Rev. A **86**, 031801(R) (2012).

[72] L. A. Lugiato and R. Lefever, "Spatial dissipative structures in passive optical systems," Phys. Rev. Lett. **58**, 2209 (1987).

[73] G. L. Oppo, M. Brambilla, and L. A. Lugiato, "Formation and evolution of roll patterns in optical parametric oscillators," Phys. Rev. A **49**, 2028 (1994).

[74] L. A. Lugiato, "Transverse Nonlinear Optics: introduction and Review," Chaos, Solitons and Fractals **4**, 1251 (1994).

[75] L. A. Lugiato, W. Kaige, and N. B. Abraham, "Spatial pattern formation and instabilities in resonators with nonlinear dispersive media," Phys. Rev. A **49**, 2049 (1994).

[76] W. J. Firth and A. J. Scroggie, "Spontaneous Pattern Formation in an Absorptive System," Europhys. Lett. **26**, 521 (1994).

[77] C. Etrich, D. Michaelis, U. Peschel, and F. Lederer, "Short-term stability of patterns in intracavity vectorial second-harmonic generation," Phys. Rev. E **58**, 4005 (1998).

[78] W. J. Firth, A. J. Scroggie, G. S. McDonald, and L. A. Lugiato, "Hexagonal patterns in optical bistability," Phys. Rev. A **46**, R3609 (1992).

[79] A. J. Scroggie, W. J. Firth, G. S. McDonald, M. Tlidi, R. Lefever, and L. A. Lugiato, "Pattern Formation in a Passive Kerr Cavity," Chaos, Solitons and Fractals **4**, 1323 (1994).

[80] J. B. Geddes, J. V. Moloney, E. M. Wright, W. J. Firth, "Polarisation patterns in a nonlinear cavity," Opt. Comm. **111**, 623 (1994).

[81] M. Hoyuelos, P. Colet, M. San Miguel, and D. Walgraef, "Polarization patterns in Kerr media," Phys. Rev. E **58**, 2992 (1998).

[82] T. Maggipinto, M. Brambilla, and W. J. Firth, "Characterization of Stationary Patterns and Their Link With Cavity Solitons in Semiconductor Microresonators," IEEE Journ. of Quant. Electronics, **39**, 206 (2003).

[83] D. Gomila and P. Colet, "Transition from hexagons to optical turbulence," Phys. Rev. A **68**, 011801(R) (2003).

[84] D. Gomila and P. Colet, "Dynamics of hexagonal patterns in a self-focusing Kerr cavity," Phys. Rev. E **76**, 016217 (2007).

[85] B. Crosignani, M. Segev, D. Eugin, P. Di Porto, A. Yariv, and G. Salamo, "Self-trapping of optical beams in photorefractive media," J. Opt. Soc. Am. B **10**, 446 (1993).

[86] P. V. Mamyshev, A. Villeneuve, G. I. Stegeman, and J. S. Aitchinson, "Steerable optical waveguides formed by bright spatial solitons in AlGaAs," Electron. Lett. **30**, 726 (1994).

[87] Y. S. Kivshar and X. Yang, "Dynamics of Dark Solitons," Chaos, Solitons and Fractals **4**, 1745 (1994).

[88] M. Tlidi, P. Mandel, and R. Lefever, "Localized Structures and Localized Patterns in Optical Bistability," Phys. Rev. Lett. **73**, 640 (1994).

[89] M. Tlidi and P. Mandel, "Spatial Patterns in Nascent Optical Bistability," Chaos Solitons Fractals **4**, 1475 (1994).

[90] V. B. Taranenko, I. Ganne, R. Kuszlewicz, and C. O. Weiss, "Spatial solitons in a semiconductor microresonator," Appl. Phys. B **72**, 377 (2001).

[91] Y. Kivshar and G. Agrawal, "Optical Solitons: From Fibers to Photonic Crystals," Acad. Press, 2003.

[92] Y. Tanguy, T. Ackemann, W. J. Firth, and R. Jäger, "Realization of a Semiconductor-Based Cavity Soliton Laser," Phys. Rev. Lett. **100**, 013907 (2008).

[93] M. Brambilla, L. A. Lugiato, F. Prati, L. Spinelli, and W. J. Firth, "Spatial Soliton Pixels in Semiconductor Devices," Phys. Rev. Lett. **79**, 2042 (1997).

[94] D. Michaelis, U. Peschel, and F. Lederer, "Multistable localized structures and superlattices in semiconductor optical resonators," Phys. Rev. A **56**, R3366 (1997).

[95] D. V. Skryabin and W. J. Firth, "Interaction of cavity solitons in degenerate optical parametric oscillators," Opt. Lett. **24**, 1056 (1999).

[96] D. Michaelis, U. Peschel, C. Etrich, and F. Lederer, "Quadratic Cavity Solitons - The Up-Conversion Case," J. of Quantum Electronics **39**, 255 (2003).

[97] L. Spinelli, G. Tissoni, M. Brambilla, F. Prati, and L. A. Lugiato, "Spatial solitons in semiconductor microcavities," Phys. Rev. A **58**, 2542 (1998).

[98] U. Peschel, D. Michaelis, and C. O. Weiss, "Spatial Solitons in Optical Cavities," IEEE J. Quatum Electron. **39**, 51 (2003).

[99] N. N. Rosanov and G. V. Khodova, "Diffractive autosolitons in nonlinear interferometers," J. Opt. Soc. Am. B **7**, 1057 (1990).

[100] O. A. Egorov, D. V. Skryabin, and F. Lederer, "Theory of Polariton Solitons in Semiconductor Microcavities," Springer Series in Optical Sciences **170**, 171-193 (2012)

[101] A. Wallraff, D. I. Schuster, A. Blais, L. Frunzio, R.-S. Hiang, J. Majer, S. Kumar, S. M. Girvin, and R. J. Schoelkopf, "Strong coupling of a single photon to a qubit using circuit quantum electrodynamics," Nature **431**, 162 (2004).

[102] K. Słowik, R. Filter, J. Straubel, F. Lederer, and C. Rockstuhl, "Strong coupling of optical nanoantennas and atomic systems," Phys. Rev. B **88**, 195414 (2013).

[103] A. Einstein, "Über einen die Erzeugung und Verwandlung des Lichtes betreffenden heuristischen Gesichtspunkt," Annalen der Physik **17**, 132 (1905).

[104] P. A. Franken, A. E. Hill, C. W. Peters, and G. Weinreich, "Generation of Optical Harmonics," Phys. Rev. Lett. **7**, 118 (1961).

[105] R. Y. Chiao, E. Garmire, and C. H. Townes, "Self-Trapping of Optical Beams," Phys. Rev. Lett. **13**, 479 (1964).

[106] A. L. Schawlow and C. H. Townes, "Infrared and Optical Masers," Phys. Rev. Lett. **112**, 1940 (1958).

[107] T. H. Maiman, "Stimulated Optical Radiation in Ruby," Nature **187**, 493 (1960).

[108] P. N. Butcher and D. Cotter, "The Elements of Nonlinear Optics," Cambridge University Press (2003).

[109] R. W. Boyd, "Nonlinear Optics," 3$^{\text{rd}}$ ed., Wiley-VCH (2008).

[110] M. Born and E. Wolf, "Principles of Optics," 7$^{\text{th}}$ ed., Cambridge University Press (1999).

[111] B. Deveaud (editor), "The Physics of Semiconductor Microcavities," Wiley-VCH (2007).

[112] D. Sanvitto and V. Timofeev (editors), "Exciton Polaritons in Microcavities," Springer (2012).

[113] J. J. Baumberg and L. Viña, "Special issue on microcavities," Semicond. Sci. Technol. **18**, S279 (2003).

[114] A. Kronenberger and P. Pringsheim, "Über das Absorptionsspektrum des festen Benzols bei $-180°$," Z. Phys. B **40**, 75 (1926).

[115] J. Frenkel, "On the Transformation of light into Heat in Solids. I," Phys. Rev. **37**, 17 (1931).

[116] J. Frenkel, "On the solid body model of heavy nuclei," Phys. Z. der Sowjetunion **9**, 533 (1936).

[117] G. H. Wannier, "The Structure of Electronic Excitation Levels in Insulating Crystals," Phys. Rev. **52**, 191 (1937).

[118] N. F. Mott, "Conduction in polar crystals. II. The conduction band and ultra-violet absorption of alkali-halide crystals," Trans. Faraday Soc. **34**, 500 (1938).

[119] V. Agranovich, H. Benisty, and C. Weisbuch, "Organic and inorganic quantum wells in a microcavity: Frenkel-Wannier-Mott excitons hybridization and energy transformation" Solid State Commun. **102**, 631 (1997).

[120] Ch. Kittel, "Einführung in die Festkörperphysik," 14$^{\text{th}}$ ed., Oldenbourg (2006).

[121] C. J. Hwang, "Lifetimes of Free and Bound Excitons in High-Purity GaAs," Phys. Rev. B **8**, 646 (1973).

[122] M. Shinada and S. Sugano, "Interband Optical Transitions in Extremely Anisotropic Semiconductors. I. Bound and Unbound Exciton Absorption," J. Phys. Soc. Jpn. **21**, 1936 (1966).

[123] G. Bastard, E. E. Mendez, L. L. Chang, and L. Esaki, "Exciton binding energy in quantum wells," Phys. Rev. B **26**, 1974 (1982).

[124] R. Loudon, "One-Dimensional Hydrogen Atom," Am. J. Phys. **27**, 649 (1959).

[125] H. Stolz, D. Schwarze, W. von der Osten, and G. Weimann, "Dephasing of excitons in quantum well structures studied by picosecond time-resolved resonant Rayleigh scattering," Superlattices and Microstructures, **9**, 511 (1991).

[126] S. Pau, J. Kuhl, F. Scholz, V. Haerle, M. A. Khan, and C. J. Sun, "Femtosecond degenerate four-wave mixing of GaN on sapphire: Measurement of intrinsic exciton dephasing time," Phys. Rev. B **56**, R12718(R) (1997).

[127] G. Khitrova, H. M. Gibbs, M. Kira, S. W. Koch, and A. Scherer, "Vacuum Rabi splitting in semiconductors," Nature Physics **2**, 81 (2006).

[128] G. Khitrova, H. M. Gibbs, F. Jahnke, M. Kira, and S. W. Koch, "Nonlinear optics of normal-mode coupling semiconductor microcavities," Rev. Mod. Phys. **71**, 1591 (1999).

[129] K. J. Vahala, "Optical microcavities," Nature **424**, 839 (2003).

[130] M. S. Skolnick, T. A. Fisher, and D. M. Whittaker, "Strong coupling phenomena in quantum microcavity structures," Semicond. Sci. Tech. **13**, 645 (1998).

[131] J. P. Reithmaier, G. Sęk, A. Löffler, C. Hofmann, S. Kuhn, S. Reitzenstein, L. V. Keldysh, V. D. Kulakovskii, T. L. Reinecke, and A. Forchel, "Strong coupling in a single quantum dot-semiconductor microcavity system," Nature **432**, 197 (2004).

[132] D. G. Lidzey, D. D. C. Bradley, M. S. Skolnick, T. Virgili, S. Walker, and D. M. Whittaker, "Strong exciton-photon coupling in an organic semiconductor microcavity," Nature **395**, 53 (1998).

[133] V. Savona, Z. Hradil, A. Quattropani, and P. Schwendimann, "Quantum theory of quantum-well polaritons in semiconductor microcavities," Phys. Rev. B **49**, 8774 (1994).

[134] R. Houdré, J. L. Gibernon, P. Pellandini, R. P. Stanley, U. Oesterle, C. Weisbuch, J. O'Gorman, B. Roycroft, and M. Ilegems, "Saturation of the strong-coupling regime in a semiconductor microcavity: Free-carrier bleaching of cavity polaritons," Phys. Rev. B **52**, 7810 (1995).

[135] S. Schmitt-Rink, D. S. Chemla, and D. A. B. Miller, "Theory of transient excitonic optical nonlinearities in semiconductor quantum-well structures," Phys. Rev. B **32**, 6601 (1985).

[136] H. M. Gibbs, G. Khitrova, and S. W. Koch, "Exciton-polariton light-semiconductor coupling effects," Nature Photonics **5**, 273 (2011).

[137] E. S. Lee, C. Ell, P. Brick, C. Spiegelberg, H. M. Gibbs, G. Khitrova, D. G. Deppe, and D. L. Huffaker "Saturation of normal-mode coupling in aluminum-oxide-aperture semiconductor nanocavities," J. Appl. Phys. **89**, 807 (2001).

[138] A. Verger, C. Ciuti, and I. Carusotto, "Polariton quantum blockade in a photonic dot," Phys. Rev. B **73**, 193306 (2006).

[139] R. J. Thompson, G. Rempe, and H. J. Kimble, "Observation of normal-mode splitting for an atom in an optical cavity," Phys. Rev. Lett. **68**, 1132 (1992).

[140] S. Pau, G. Björk, J. Jacobson, H. Cao, and Y. Yamamoto, "Microcavity exciton-polariton splitting in the linear regime," Phys. Rev. B **51**, 14437 (1995).

[141] C. Ciuti, V. Savona, C. Piermarocchi, and A. Quattropani, "Role of exchange of carriers in elastic exciton-exciton scattering in quantum wells," Phys. Rev. B **58**, 7926 (1998).

[142] P. Borri, W. Langbein, U. Woggon, A. Esser, J. R. Jensen, and J. M. Hvam, "Biexcitons in semiconductor microcavities," Semicond. Sci. Technol. **18**, S351 (2003).

[143] J. J. Hopfield, "Theory of the Contribution of Excitons to the Complex Dielectric Constant of Crystals," Phys. Rev. **112**, 1555 (1958).

[144] O. A. Egorov and F. Lederer, "Formation of hybrid parametric cavity solitons," Phys. Rev. B **87**, 115315 (2013).

[145] O. A. Egorov and F. Lederer, "Pseudospin-induced motion of cavity polariton soliton molecules," Opt. Lett. **39**, 4028 (2014).

[146] O. A. Egorov, D. V. Skryabin, and F. Lederer, "Polariton solitons due to saturation of the exciton-photon coupling," Phys. Rev. B **82**, 165326 (2010).

[147] I. G. Savenko, E. B. Magnusson, and I. A. Shelykh, "Density-matrix approach for an interacting polariton system," Phys. Rev. B **83**, 165316 (2011).

[148] M. Wouters, and I. Carusotto, "Parametric oscillation threshold of semiconductor microcavities in the strong coupling regime," Phys. Rev. B **75**, 75332 (2007).

[149] M. Vladimirova, S. Cronenberger, D. Scalbert, K. V. Kavokin, A. Minard, A. Lemaître, J. Bloch, D.Solnyshkov, G. Malpuech, and A. V. Kavokin, "Polariton-polariton interaction constants in microcavities," Phys. Rev. B **82**, 075301 (2010).

[150] I. A. Shelykh, A. V. Kavokin, and G. Malpuech, "Spin dynamics of exciton polaritons in microcavities," phys. stat. sol. (b) **242**, 2271 (2005).

[151] I. A. Shelykh, A. V. Kavokin, Y. G. Rubo, T. C. Liew, and G. Malpuech, "Polariton polarization-sensitive phenomena in planar semiconductor microcavities," Semicond. Sci. Technol. **25**, 13001 (2010).

[152] P. Renucci, T. Amand, and X. Marie, "Coherent spin dynamics of polaritons in semiconductor microcavities," Semicond. Sci. Technol. **18**, S361 (2003).

[153] P. Renucci, T. Amand, X. Marie, P. Senellart, J. Bloch, B. Sermage, and K. V. Kavokin, "Microcavity polariton spin quantum beats without a magnetic field: A manifestation of Coulomb exchange in dense and polarized polariton systems," Phys. Rev. B **72**, 075317 (2005).

[154] K. V. Kavokin, I. A. Shelykh, A. V. Kavokin, G. Malpuech, and P. Bigenwald, "Quantum Theory of Spin Dynamics of Exciton-Polaritons in Microcavities," Phys. Rev. Lett. **92**, 017401 (2004).

[155] M. Z. Maialle, E. A. de Andrada e Silva, and L. J. Sham, "Exciton spin dynamics in quantum wells," Phys. Rev. B **47**, 15776 (1993).

[156] G. Pikus and G. Bir, "Exchange interaction in excitons in semiconductors," Zh. Eksp. Teor. Fiz. **60**, 195 [Sov. Phys. JETP **33**, 108 (1971)].

[157] I. A. Shelykh, L. Viña, A. V. Kavokin, N. G. Galkin, G. Malpuech, and R. André, "Non-linear coupling of polariton and dark exciton states in semiconductor microcavities," Solid State Commun. **135**, 1 (2005).

[158] E. A. de Andrada e Silva and G. C. La Rocca, "Suppressed Electron-Hole Exchange Spin Flip in Cavity Polaritons," Phys. Stat. Sol.(a) **190**, 427 (2002).

[159] T. K. Paraïso, M. Wouters, Y. Léger, F. Morier-Genoud, and B. Deveaud-Plédran, "Multistability of a coherent spin ensemble in a semiconductor microcavity," Nat. Mater. **9**, 655 (2010).

[160] G. Panzarini, L. C. Andreani, A. Armitage, D. Baxter, M. S. Skolnick, V. N. Astratov, J. S. Roberts, A. V. Kavokin, M. V. Vladimirova, and M. A. Kaliteevski, "Exciton-light coupling in single and coupled semiconductor microcavities: Polariton dispersion and polarization splitting," Phys. Rev. B **59**, 5082 (1999).

[161] S. Schumacher, N. H. Kwong, and R. Binder, "Influence of exciton-exciton correlation on the polarization characteristics of polariton amplification in semiconductor microcavities," Phys. Rev. B **76**, 245324 (2007).

[162] T. C. H. Liew, A. V. Kavokin, and I. A. Shelykh, "Excitation of vortices in semiconductor microcavities," Phys. Rev. B **75**, 241301(R) (2007).

[163] A. Werner, O. A. Egorov, and F. Lederer, "Exciton-polariton patterns in coherently pumped semiconductor microcavities," Phys. Rev. B **89**, 245307 (2014).

[164] A. Werner, O. A. Egorov, and F. Lederer, "Pseudospin dynamics of exciton-polariton patterns in a coherently driven semiconductor microcavity," Phys. Rev. B **90**, 165308 (2014).

[165] A. Werner, O. A. Egorov, and F. Lederer, "Spin dynamics of dark polariton solitons," Phys. Rev. B **85**, 115315 (2012).

[166] O. A. Egorov, D. V. Skryabin, A. V. Yulin, and F. Lederer, "Bright Cavity Polariton Solitons," Phys. Rev. Lett. **102**, 153904 (2009).

[167] M. Sich, D. N. Krizhanovskii, M. S. Skolnick, A. V. Gorbach, R. Hartley, D. V. Skryabin, E. A. Cerda-Méndez, K. Biermann, R. Hey, and P. V. Santos, "Observation of bright polariton solitons in a semiconductor microcavity," Nature Photonics **6**, 50 (2011).

[168] M. Sich, F. Fras, J. K. Chana, M. S. Skolnick, D. N. Krizhanovskii, A. V. Gorbach, R. Hartley, D. V. Skryabin, S. S. Gavrilov, E. A. Cerda-Méndez, K. Biermann, R. Hey, and P. V. Santos, "Effects of Spin-Dependent Interactions on Polarization of Bright Polariton Solitons," Phys. Rev. Lett. **112**, 046403 (2014).

[169] R. Houdré, C. Weisbuch, R. P. Stanley, U. Oesterle, P. Pellandini, and M. Ilegems, "Measurement of Cavity-Polariton Dispersion Curve from Angle-Resolved Photoluminescence Experiments," Phys. Rev. Lett. **73**, 2043 (1994).

[170] A. V. Yulin, O. A. Egorov, F. Lederer, and D. V. Skryabin, "Dark polariton solitons in semiconductor microcavities," Phys. Rev. A **78**, 061801(R) (2008).

[171] A. Kavokin, P. G. Lagoudakis, G. Malpuech, and J. J. Baumberg, "Polarization rotation in parametric scattering of polaritons in semiconductor microcavities," Phys. Rev. B **67**, 195321 (2003).

[172] N. A. Gippius, I. A. Shelykh, D. D. Solnyshkow, S. S. Gavrilov, Yuri G. Rubo, A. V. Kavokin, S. G. Tikhodeev, and G. Malpuech, "Polarization Multistability of Cavity Polaritons," Phys. Rev. Lett. **98**, 236401 (2007).

[173] T. C. H. Liew and I. A. Shelykh, "Polarization phenomena in resonantly pumped disordered semiconductor microcavities," Phys. Rev. B **80**, 161303(R) (2009).

[174] S. S. Gavrilov, N. A. Gippius, S. G. Tikhodeev, and V. D. Kulakovskii, "Multistability of the Optical Response in a System of Quasi-Two-Dimensional Exciton Polaritons," JETP **110**(5), 825 (2010) [Zh. Eksper. Teor. Fiz. **137**, 943 (2010)].

[175] D. Sarkar, S. S. Gavrilov, M. Sich, J. H. Quilter, R. A. Bradley, N. A. Gippius, K. Guda, V. D. Kulakovskii, M. S. Skolnick, and D. N. Krizhanovskii, "Polarization Bistability and Resultant Spin Rings in Semiconductor Microcavities," Phys. Rev. Lett. **105**, 216402 (2010).

[176] Ö. Bozat, I. G. Savenko, and I. A. Shelykh, "Spin multistability in dissipative polariton channels," Phys. Rev. B **86**, 035413 (2012).

[177] A. M. Turing, "The Chemical Basis of Morphogenesis," Phil. Trans. R. Soc. **B237**, 37 (1952).

[178] S. Schumacher, "Spatial anisotropy of polariton amplification in planar semiconductor microcavities induced by polarization anisotropy," Phys. Rev. B **77**, 073302 (2008).

[179] O. A. Egorov, A. Werner, T. C. H. Liew, E. A. Ostrovskaya, and F. Lederer, "Motion of patterns in polariton quantum fluids with spin-orbit interaction," Phys. Rev. B **89**, 235302 (2014).

[180] F. Manni, K. G. Lagoudakis, T. K. Paraïso, R. Cerna, Y. Léger, T. C. H. Liew, I. A. Shelykh, A. V. Kavokin, F. Morier-Genoud, and B. Deveaud-Plédran, "Spin-to-orbital angular momentum conversion in semiconductor microcavities," Phys. Rev. B **83**, 241307(R) (2011).

[181] P. Coullet and K. Emilsson, "Strong resonances of spatially distributed oscillators: a laboratory to study patterns and defects," Physica D **61**, 119 (1992).

[182] M. H. Luk, Y. C. Tse, N. H. Kwong, P. T. Leung, P. Lewandowski, R. Binder, and S. Schumacher, "Transverse optical instability patterns in semiconductor microcavities: Polariton scattering and low-intensity all-optical switching," Phys. Rev. B **87**, 205307 (2013).

[183] F. Tassone, C. Piermarocchi, V. Savona, A. Quattropani, and P. Schwendimann, "Bottleneck effects in the relaxation and photoluminescence of microcavity polaritons," Phys. Rev. B **56**, 7554 (1997).

[184] M. Tlidi and P. Mandel, "Space-time localized structures in the degenerate optical parametric oscillator," Phys. Rev. A **59**, R2575 (1999).

[185] G. K. Harkness, W. J. Firth, G.-L. Oppo, and J. M. McSloy, "Computationally determined existence and stability of transverse structures. I. Periodic optical patterns," Phys. Rev. E **66**, 046605 (2002).

[186] J. M. McSloy, W. J. Firth, G. K. Harkness, and G.-L. Oppo, "Computationally determined existence and stability of transverse structures. II. Multipeaked cavity solitons," Phys. Rev. E **66**, 046606 (2002).

[187] H. Terças, D. D. Solnyshkov, and G. Malpuech, "Topological Wigner Crystal of Half-Solitons in a Spinor Bose-Einstein Condensate," Phys. Rev. Lett. **110**, 035303 (2013).

[188] V. B. Taranenko, K. Staliunas, and C. O. Weiss, "Pattern Formation and Localized Structures in Degenerate Optical Parametric Mixing," Phys. Rev. Lett. **81**, 2236 (1998).

[189] H. Flayac, D. D. Solnyshkov, and G. Malpuech, "Oblique half solitons and their generation in exciton-polariton condensates," Phys. Rev. B **83**, 193305 (2011).

[190] D. Gomila, P. Colet, G. L. Oppo, and M. San Miguel, "Stable Droplets and Growth Laws Close to the Modulational Instability of a Domain Wall," Phys. Rev. Lett. **87**, 194101 (2001).

[191] H. Flayac, D. D. Solnyshkov, I. A. Shelykh, and G. Malpuech, "Transmutation of Skyrmions to Half-Solitons Driven by the Nonlinear Optical Spin Hall Effect," Phys. Rev. Lett. **110**, 016404 (2013).

[192] A. Kavokin, G. Malpuech, and M. Glazov, "Optical Spin Hall Effect," Phys. Rev. Lett. **95**, 136601 (2005).

[193] C. Leyder, M. Romanelli, J. P. Karr, E. Giacobino, T. C. H. Liew, M. M. Glazov, A. V. Kavokin, G. Malpuech, and A. Bramati, "Observation of the optical spin Hall effect," Nat. Phys. **3**, 628 (2007).

[194] E. Kammann, T. C. H. Liew, H. Ohadi, P. Cilibrizzi, P. Tsotis, Z. Hatzopoulos, P. G. Savvidis, A. V. Kavokin, and P. G. Lagoudakis, "Nonlinear Spin Hall Effect and Long-Range Spin Transport in Polariton Lasers," Phys. Rev. Lett. **109**, 036404 (2012).

[195] W. Langbein, I. Shelykh, D. Solnyshkov, G. Malpuech, Yu. Rubo, and A. Kavokin, "Polarization beats in ballistic propagation of exciton-polaritons in microcavities," Phys. Rev. B **75**, 075323 (2007).

[196] A. Amo, T. C. H. Liew, C. Adrados, E. Giacobino, A. V. Kavokin, and A. Bramati, "Observation of the optical spin Hall effect," Phys. Rev. B **80**, 165325 (2009).

[197] K. Staliunas, "Vortices and Dark Solitons in the Two-dimensional Nonlinear Schrödinger Equation," Chaos, Solitons and Fractals **4**, 1783 (1994).

[198] V. E. Zakharov and A. B. Shabat, "Exact Theory of Two-dimensional Self-focusing and One-dimensional Self-modulation of Wave in Nonlinear Media," Sov. Phys. JETP **34**, 62 (1972).

[199] G. S. McDonald and W. J. Firth, "Spatial solitary-wave optical memory," J. Opt. Soc. Am. B **7**, 1328 (1990).

[200] W. J. Firth and A. J. Scroggie, "Optical Bullet Holes: Robust Controllable Localized States of a Nonlinear Cavity," Phys. Rev. Lett. **76**, 1623 (1996).

[201] C. Etrich, D. Michaelis, and F. Lederer, "Bifurcations, stability, and multistability of cavity solitons in parametric downconversion," J. Opt. Soc. Am. B **19**, 792 (2002).

[202] D. Michaelis, U. Peschel, and F. Lederer, "Oscillating dark cavity solitons," Opt. Lett. **23**, 1814 (1998).

[203] G. Rochat, C. Ciuti, V. Savona, C. Piermarocchi, A. Quattropani, and P. Schwendimann "Excitonic Bloch equations for a two-dimensional system of interacting excitons," Phys. Rev. B **61**, 13856 (2000).

[204] D. Bajoni, E. Semenova, A. Lemaître, S. Bouchoule, E. Wertz, P. Senellart, S. Barbay, R. Kuszelewicz, and J. Bloch, "Optical Bistability in a GaAs-Based Polariton Diode," Phys. Rev. Lett. **101**, 266402 (2008).

[205] Y. Larionova, W. Stolz, and C. O. Weiss, "Optical bistability and spatial resonator solitons based on exciton-polariton nonlinearity," Opt. Lett. **33**, 321 (2008).

[206] A. Amo, T. C. H. Liew, C. Adrados, R. Houdré, E. Giacobino, A. V. Kavokin, and A. Bramati, "Exciton-polariton spin switches," Nat. Photonics **4**, 361 (2010).

[207] W. J. Firth, G. K. Harkness, A. Lord, J. M. McSloy, D. Gomila, and P. Colet, "Dynamical properties of two-dimensional Kerr cavity solitons," J. Opt. Soc. Am. B **19**, 747 (2002).

[208] O. A. Egorov and F. Lederer, "Rotating cavity solitons in semiconductor microresonators," Phys. Rev. E **75**, 017601 (2007).

[209] W. L. Zhang and S. F. Yu, "Vectorial polariton solitons in semiconductor microcavities," Opt. Express **18**, 21219 (2010).

[210] H. Flayac, D. D. Solnyshkov, and G. Malpuech, "Separation and acceleration of magnetic monopole analogs in semiconductor microcavities," New Journal of Physics **14**, 085018 (2012).

[211] R. Hivet, H. Flayac, D. D. Solnyshkov, D. Tanese, T. Boulier, D. Andreoli, E. Giacobino, J. Bloch, A. Bramati, G. Malpuech, and A. Amo, "Half-solitons in a polariton quantum fluid behave like magnetic monopoles," Nature Physics **8**, 724 (2012).

[212] I. Pérez-Arjona, V. J. Sánchez-Morcillo, G. J. de Valcárcel, and E. Roldán, "Bright cavity solitons in anisotropic vectorial Kerr cavities," J. Opt. B: Quantum Semiclass. Opt. **3** S118 (2001).

[213] U. Peschel, D. Michaelis, C. Etrich, and F. Lederer, "Formation, motion, and decay of vectorial cavity solitons," Phys. Rev. E **58**, R2745 (1998).

[214] K. Staliunas and V. J. Sanchez-Morcillo, "Transverse Patterns in Nonlinear Optical Resonators," Springer-Verlag Berlin Heidelberg New York, (2003).

[215] P. Coullet, J. Lega, B. Houchmanzadeh, and J. Lajzerowicz, "Breaking Chirality in Nonequilibrium Systems," Phys. Rev. Lett. **65**, 1352 (1990).

[216] A. Hagberg, E. Meron, I. Rubinstein, and B. Zaltzman, "Controlling Domain Patterns Far from Equilibrium," Phys. Rev. Lett. **76**, 427 (1996).

[217] A. Hagberg, E. Meron, I. Rubinstein, and B. Zaltzman, "Order parameter equations for front transitions: Planar and circular fronts," Phys. Rev. E **55**, 4450 (1997).

[218] A. Hagberg and E. Meron, "The Dynamics of Curved Fronts: Beyond Geometry," Phys. Rev. Lett. **78**, 1166 (1997).

[219] T. Frisch, S. Rica, P. Coullet, and J. M. Gilli, "Spiral waves in liquid crystal," Phys. Rev. Lett. **72**, 1471 (1994).

[220] S. Nasuno, N. Yoshimo, and S. Kai, "Structural transition and motion of domain walls in liquid crystals under a rotating magnetic field," Phys. Rev. E **51**, 1598 (1995).

[221] P. Coullet, J. Lega, and Y. Pomeau, "Dynamics of Bloch Walls in a Rotating Magnetic Field a Model," Europhys. Lett. **15**, 221 (1991).

[222] Y. Rzhanov, H. Richardson, A. Hagberg, and J. Moloney, "Spatiotemporal oscillations in a semiconductor étalon," Phys. Rev. A **47**, 1480 (1993).

[223] G. Izús, M. San Miguel, and M. Santagiustina, "Bloch domain walls in type II optical parametric oscillators," Opt. Lett. **25**, 1454 (2000).

[224] D. Michaelis, U. Peschel, F. Lederer, D. V. Skryabin, and W. J. Firth, "Universal criterion and amplitude equation for a nonequilibrium Ising-Bloch transition," Phys. Rev. E **63**, 066602 (2001).

A. Bosonic operator algebra

According to Ref. [47], excitons (and likewise polaritons) exhibit a Bose-like statistic, as long as the excited density is much smaller than the typical exciton saturation density. Their bosonic nature is demonstrated experimentally with sufficient certainty in the framework of Bose-Einstein condensation [14–22].

Thus, excitons as well as photons can be described with bosonic creation $(\hat{a}_{\mathbf{k}}^{\dagger})$ and annihilation $(\hat{a}_{\mathbf{k}})$ operators. These bosonic operators obey the following commutation rules:

$$[\hat{a}_{\mathbf{k}}, \hat{a}_{\mathbf{k}'}] = 0, \tag{A.1}$$

$$\left[\hat{a}_{\mathbf{k}}^{\dagger}, \hat{a}_{\mathbf{k}'}^{\dagger}\right] = 0, \tag{A.2}$$

$$\left[\hat{a}_{\mathbf{k}}, \hat{a}_{\mathbf{k}'}^{\dagger}\right] = \delta\left(\mathbf{k} - \mathbf{k}'\right), \tag{A.3}$$

where

$$\left[\hat{a}, \hat{b}\right] := \hat{a}\hat{b} - \hat{b}\hat{a} \tag{A.4}$$

denotes the commutator of the operators $\hat{a}$ and $\hat{b}$. Operators denoting different excitations (namely exciton and photon operators) always commute. The commutator algebra is used to calculate the Heisenberg EOM (2.11)-(2.12) for the field operators of cavity photons and excitons. We show this procedure exemplarily for the excitons $\hat{b}_{\mathbf{k}}$. We start with the Heisenberg equation of motion:

$$i\partial_t \hat{b}_{\mathbf{p}} = \left[\hat{H}, \hat{b}_{\mathbf{p}}\right]. \tag{A.5}$$

Besides from rather simple contributions, this commutator contains the term $\left[\hat{H}_{\mathrm{XX}}, \hat{b}_{\mathbf{p}}\right]$ which will be computed using the linearity of the commutator and its properties (A.1)-(A.3):

$$\left[\hat{H}_{\mathrm{XX}}, \hat{b}_{\mathbf{p}}\right] = \left[\frac{1}{2}\sum_{\mathbf{k},\mathbf{k}',\mathbf{q}} V_{\mathrm{XX}}(\mathbf{q})\hat{b}_{\mathbf{k}+\mathbf{q}}^{\dagger}\hat{b}_{\mathbf{k}'-\mathbf{q}}^{\dagger}\hat{b}_{\mathbf{k}}\hat{b}_{\mathbf{k}'}, \hat{b}_{\mathbf{p}}\right] \tag{A.6}$$

$$= \sum_{\mathbf{k},\mathbf{k}',\mathbf{q}} \frac{V_{\mathrm{XX}}(\mathbf{q})}{2}\left\{\hat{b}_{\mathbf{k}+\mathbf{q}}^{\dagger}\hat{b}_{\mathbf{k}'-\mathbf{q}}^{\dagger}\underbrace{\left[\hat{b}_{\mathbf{k}}\hat{b}_{\mathbf{k}'}, \hat{b}_{\mathbf{p}}\right]}_{=0} + [\hat{b}_{\mathbf{k}+\mathbf{q}}^{\dagger}\hat{b}_{\mathbf{k}'-\mathbf{q}}^{\dagger}, \hat{b}_{\mathbf{p}}]\,\hat{b}_{\mathbf{k}}\hat{b}_{\mathbf{k}'}\right\} \tag{A.7}$$

$$= \sum_{\mathbf{k},\mathbf{k}',\mathbf{q}} \frac{V_{\mathrm{XX}}(\mathbf{q})}{2}\left\{\hat{b}_{\mathbf{k}+\mathbf{q}}^{\dagger}\left[\hat{b}_{\mathbf{k}'-\mathbf{q}}^{\dagger}, \hat{b}_{\mathbf{p}}\right] + \left[\hat{b}_{\mathbf{k}+\mathbf{q}}^{\dagger}, \hat{b}_{\mathbf{p}}\right]\hat{b}_{\mathbf{k}'-\mathbf{q}}^{\dagger}\right\}\hat{b}_{\mathbf{k}}\hat{b}_{\mathbf{k}'}. \tag{A.8}$$

If we now evaluate the two commutators and additionally assume that $V_{\mathrm{XX}}(\mathbf{q})$ can be approximated with $V_{\mathrm{XX}}(\mathbf{0})$, we end up with

$$
\begin{aligned}
\left[\hat{H}_{\mathrm{XX}}, \hat{b}_{\mathbf{p}}\right] &\approx -V(\mathbf{0}) \sum_{\mathbf{k},\,\mathbf{k}'} \hat{b}^{\dagger}_{\mathbf{k}+\mathbf{k}'-\mathbf{p}} \hat{b}_{\mathbf{k}} \hat{b}_{\mathbf{k}'} && \text{(A.9)} \\
&= -V(\mathbf{0}) \left(\hat{b}^{\dagger} \star \hat{b} \star \hat{b}\right)_{\mathbf{p}}, && \text{(A.10)}
\end{aligned}
$$

where the $\star$ symbol indicates the convolution of the fields.

List of Abbreviations and Symbols

The following table lists abbreviations, acronyms, and symbols used throughout the thesis.

α cross-phase modulation parameter between polaritons with pseudospin $+1$ and -1.

α_{crit} critical value of α where asymmetric HSs bifurcate from symmetric HSs; α_{crit} is given by Eq. (5.10).

β scaled TE-TM splitting parameter.

Δ detuning; joint denotation for Δ_c and Δ_0, in case that they are identical.

$\delta\Delta_{\mathrm{LPB}}$ TE-TM splitting of Δ_{LPB}.

$\delta\Delta_{\mathrm{UPB}}$ TE-TM splitting of Δ_{UPB}.

$\Delta\Omega_s$ frequency shift of a Fourier component.

Δ_0 detuning of the pump frequency from the resonance frequency of the excitons.

Δ_c detuning of the pump frequency from the resonance frequency of the cavity.

Δ_{LPB} lower branch of the (scalar) linear dispersion relation.

$\Delta_{\mathrm{LPB}}^{\pm}$ TE-TM split version of Δ_{LPB}.

$\Delta_{\mathrm{TE\text{-}TM}}$ frequency of the TE-TM splitting.

Δ_{UPB} upper branch of the (scalar) linear dispersion relation.

$\Delta_{\mathrm{UPB}}^{\pm}$ TE-TM split version of Δ_{UPB}.

ϵ dielectric constant of the semiconductor.

γ'	mean loss rate of the semiconductor microcavity; $\gamma' = (\gamma_0 + \gamma_c)/2$.
γ_0	exciton decay rate; $\gamma_0 = 1/T_2$.
γ_c	photon decay rate of the cavity.
$\hat{a}_{\mathbf{k}}$, $\hat{a}_{\mathbf{k}}^\dagger$	annihilation and creation operator for a cavity photon with wave vector $\mathbf{k}$.
$\hat{b}_{\mathbf{k}}$, $\hat{b}_{\mathbf{k}}^\dagger$	annihilation and creation operator for an exciton with wave vector $\mathbf{k}$.
$\hat{H}$	Hamiltonian for the semiclassical treatment of exciton-polaritons.
$\hat{H}_0$	linear part of the Hamiltonian.
$\hat{H}_{\mathrm{cav}}$	part of the Hamiltonian describing the dynamics of the cavity photons.
$\hat{H}_{\mathrm{exc}}$	part of the Hamiltonian describing the dynamics of excitons.
$\hat{H}_{\mathrm{lm}}$	part of the Hamiltonian describing the interaction between excitons and photons.
$\hat{H}_{\mathrm{XX,asym}}$	part of the spin-dependent Hamiltonian describing the Coulomb interaction between two excitons with opposite spin.
$\hat{H}_{\mathrm{XX,sym}}$	part of the spin-dependent Hamiltonian describing the Coulomb interaction between two excitons with equal spin.
$\hat{H}_{\mathrm{XX}}$	nonlinear part of the Hamiltonian describing the Coulomb interaction between two excitons.
$\hat{k}$	wave number in the medium.
$\hbar$	reduced Planck constant; $\hbar \approx 1.054 \cdot 10^{-34} Js$.
λ	general growth rate in the perturbation scheme.
λ_{exc}	exciton radius.
$\mathbf{k}$	transverse wave vector; $\mathbf{k} = (k_x, k_y)^t$.
$\mathbf{p}(k)$	vector containing the Hopfield coefficients e_k and ψ_k.

$\mathcal{A}$	abbreviation for $\gamma_0 + \gamma_c/(\gamma_c^2 + \Delta_c^2)$.
$\mathcal{B}$	abbreviation for $-\Delta_0 + \Delta_c/(\gamma_c^2 + \Delta_c^2)$.
$\mathcal{F}$	finesse of the Fabry-Pérot cavity; the Q factor can be derived by multiplying $\mathcal{F}$ with the resonance frequency divided by the free spectral range.
μ	reduced mass of an exciton.
$\nabla_\perp^2$	transverse Laplace operator; $\nabla_\perp^2 = -\partial_x^2 - \partial_y^2$.
ω_c	real eigenfrequency of the cavity.
$\omega_{\mathrm{cav}}(\mathbf{k})$	dispersion relation of cavity photons.
$\omega_{\mathrm{exc}}(\mathbf{k})$	dispersion relation of excitons.
Ω_R	Rabi splitting.
Φ	azimuthal angle in the transverse plane.
$\Psi(x, y)$	scaled excitonic field in real space.
ψ_1, ψ_2	respective perturbations of Ψ and $\overline{\Psi}$ in the scalar perturbation scheme.
$\psi_1^\pm, \psi_2^\pm$	respective perturbations of $\Psi^\pm$ and $\overline{\Psi^\pm}$ in the vectorial perturbation scheme.
$\Psi_\mathbf{k}$	macroscopic excitonic field in Fourier space; $\Psi_\mathbf{k} = \left\langle \hat{b}_\mathbf{k} \right\rangle$.
ρ_p	polarization degree of the pump; in the present work, the pump is always linearly polarized ($\rho_\mathrm{p} = 0$).
τ	transmissivity of a Fabry-Pérot cavity.
θ	angle of the Fourier component with respect to the distinguished Fourier component denoted with 1.
$\varepsilon_1, \varepsilon_2$	respective perturbations of E and $\overline{E}$ in the scalar perturbation scheme.

$\varepsilon_1^\pm,\ \varepsilon_2^\pm$	respective perturbations of $E^\pm$ and $\overline{E^\pm}$ in the vectorial perturbation scheme.
$\widetilde{\beta}$	TE-TM splitting parameter.
$\widetilde{\Delta}_c$	reduced cavity detuning; $\widetilde{\Delta}_c = \Delta_c - k_x^2 - k_y^2$.
$\widetilde{\omega}_c$	complex eigenfrequency of the cavity; $\widetilde{\omega}_c = \omega_c + i\gamma_c$.
A_j	components of the Fourier decomposition of a pattern.
e	elementary charge.
$E(x,y)$	scaled electric field in real space.
E_p	pump power.
$E_{\mathbf{k}}$	macroscopic electric field in Fourier space; $E_{\mathbf{k}} = \langle \hat{a}_{\mathbf{k}} \rangle$.
$I_{0,\mathrm{crit,as}}^\pm$	intensity at the upper $(+)$ and lower $(-)$ Turing instability point for antisymmetric perturbations.
$I_{0,\mathrm{crit,s}}^\pm$	intensity at the upper $(+)$ and lower $(-)$ Turing instability point for symmetric perturbations.
I_{inc}	total incident pump intensity.
J_z^e	projection of the total angular momentum of an electron on the z axis.
J_z^h	projection of the total angular momentum of a hole on the z axis.
k_0	modulus of the Fourier components of a hexagonal pattern.
k_z	z component of the wavevector.
$k_{\mathrm{as}}^\pm$	modulus of the wave vector at the upper $(+)$ and lower $(-)$ Turing instability point for antisymmetric perturbations
$k_{\mathrm{s}}^\pm$	modulus of the wave vector at the upper $(+)$ and lower $(-)$ Turing instability point for symmetric perturbations
L_c	length of the microcavity, typically in the range of $0.2 - 0.4\mu$m.

M_z^h projection of the mechanical angular momentum of a hole on the z axis.

m_0 mass of the free electron in vacuum.

m_e effective mass of the electron in a periodic crystal potential.

m_{ph} effective mass of a cavity photon in a periodic crystal potential.

m_{hh} effective mass of a heavy hole in a periodic crystal potential.

Q factor *quality factor*, a measure for the losses of the dielectric mirrors; the average lifetime of a cavity photon is proportional to the Q factor of the cavity; typical values lie in the range of 10^4 to 10^5 [111].

r radial coordinate in the transverse plane; $r^2 = x^2 + y^2$; introduced in Sec. 4.2.3 and used to simplify calculations using the Newton-Raphson method applied to cylindrically symmetric two-dimensional problems.

r reflection coefficient of the dielectric Bragg mirror; used in Subsec. 2.1.1.

S_z^e projection of the electron spin on the z axis.

S_z^h projection of the spin of a hole on the z axis.

T_1 time constant related to the population decay of the electron-hole pairs; in the range of $1ns$.

T_2 time constant elated to the damping due to dephasing processes of the exciton wave function; in the range of $1ps$.

$U(t)$ electromagnetic energy stored in the cavity.

v velocity of a moving pattern.

$V_{\mathrm{XX,asym}}(\mathbf{k})$ effective interaction potential determined by the Coulomb interaction between two excitons in singlet configuration.

$V_{\mathrm{XX,sym}}(\mathbf{k})$ effective interaction potential determined by the Coulomb interaction between two excitons in triplet configuration.

$V_{\mathrm{XX}}(\mathbf{k})$ effective interaction potential determined by the Coulomb interaction between two excitons.

amplitude domain   domain formed between two nonequivalent states.

Bloch wall   moving domain wall.

BM   *Bragg mirror*, a one-dimensional photonic crystal operating as a dielectric mirror.

bright soliton   nondiffracting localized intensity peak above a HS background.

dark soliton   nondiffracting localized intensity dip below a HS background.

EOM   equations of motion.

FFT   Fast Fourier transform.

GaAs   *gallium arsenide*, a III-V semiconductor with direct bandgap.

Hopf bifurcation   a local bifurcation characterized by a fixed point of a dynamical system losing its stability to a pair of complex conjugate solutions in linear stability analysis.

HS   *homogeneous solution*, a solution of the EOM that is independent on time and the transverse coordinates.

InGaAs   *indium gallium arsenide*, an alloy of gallium arsenide and indium arsenide.

Ising wall   stationary domain wall.

JCH   *Jaynes-Cummings Hamiltonian* modelling the interaction between a two-level system and cavity photons.

Kerr cavity   weakly coupled microcavity with a third-order nonlinearity; a prototypical example is given by the Lugiato-Lefever model [72].

Lugiato-Lefever model   prototypical model of an optical cavity with losses, pump, and Kerr nonlinearity.

MI   *modulation instability*; instability of a solution with respect to spatially periodic perturbations.

MWP   *Maxwell point*; pump power where lower and upper branch of the
                bistability loop can be linked by a stationary wall.

NIB   *nonequilibrium Ising-Bloch transition*; a transition from a stationary
                to a moving domain wall at a bifurcation point.

NLSE   *nonlinear Schrödinger equation*; a version of the Schrödinger equa-
                tion with additional Kerr nonlinearity.

PDE   partial differential euqation.

phase domain   domain formed between two equivalent states.

QW   semiconductor *quantum well.*

symmetric solution solution of the vectorial EOM with $\rho_E(x, y) \equiv 0$.

TE-TM splitting splitting between the dispersion relations of transverse electrically
                (TE) and transverse magnetically (TM) polarized cavity modes.

Turing instability synonym to modulation instability.

VCSEL   *vertical-cavity surface-emitting laser*, a type of laser whose setup is
                also used in the semiconductor microcavities studied in this work.

vectorial soliton elliptically polarized soliton.

List of Figures

List of Publications

Peer-reviewed journals

1. A. Werner, O. A. Egorov, and F. Lederer, *Spin dynamics of dark polariton solitons,* Phys. Rev. B **85**, 115315 (2012).

2. O. A. Egorov, A. Werner, T. C. H. Liew, E. A. Ostrovskaya, and F. Lederer, *Motion of patterns in polariton quantum fluids with spin-orbit interaction,* Phys. Rev. B **89**, 235302 (2014).

3. A. Werner, O. A. Egorov, and F. Lederer, *Exciton-polariton patterns in coherently pumped semiconductor microcavities,* Phys. Rev. B **89**, 245307 (2014).

4. A. Werner, O. A. Egorov, and F. Lederer, *Pseudospin dynamics of exciton-polariton patterns in a coherently driven semiconductor microcavity,* Phys. Rev. B **90**, 165308 (2014).

International conference contributions

1. A. Werner, O. A. Egorov, and F. Lederer, *Vector polariton solitons in semiconductor microcavities,* DoKDoK Naumburg (2011).

2. A. Werner, A. Eichhorn, and H. Gies, *Ghost-curvature couplings in Quantum Einstein Gravity,* Cold Quantum Coffee Heidelberg (2011).

3. A. Werner, O. A. Egorov, and F. Lederer, *Interaction of dark vector polariton solitons,* Nonlinear Photonics, Colorado Springs (2012).

4. A. Werner, O. A. Egorov, and F. Lederer, *Spontaneous symmetry breaking of cavity polariton solitons due to pseudospin dynamics,* CLEO Quantum Electronics and Laser Science Conference, San Jose, California (2012).

5. A. Werner, O. A. Egorov, and F. Lederer, *Polariton spin dynamics in a semiconductor microcavity,* 518. WE-Heraeus-Seminar on Quantum-Optical Analogies: a Bridge Between Classical and Quantum Physics, Bad Honnef (2012).

6. A. Werner, O. A. Egorov, and F. Lederer, *Spin-induced spontaneous symmetry breaking of exciton-polariton patterns,* CLEO Europe, München (2013).

Ehrenwörtliche Erklärung

Ich erkläre hiermit ehrenwörtlich, dass ich die vorliegende Arbeit selbständig, ohne unzulässige Hilfe Dritter und ohne Benutzung anderer als der angegebenen Hilfsmittel und Literatur angefertigt habe. Die aus anderen Quellen direkt oder indirekt übernommenen Daten und Konzepte sind unter Angabe der Quelle gekennzeichnet.

Weitere Personen waren an der inhaltlich-materiellen Erstellung der vorliegenden Arbeit nicht beteiligt. Insbesondere habe ich hierfür nicht die entgeltliche Hilfe von Vermittlungs- bzw. Beratungsdiensten (Promotionsberater oder andere Personen) in Anspruch genommen. Niemand hat von mir unmittelbar oder mittelbar geldwerte Leistungen für Arbeiten erhalten, die im Zusammenhang mit dem Inhalt der vorgelegten Dissertation stehen.

Die Arbeit wurde bisher weder im In- noch im Ausland in gleicher oder ähnlicher Form einer anderen Prüfungsbehörde vorgelegt.

Die geltende Promotionsordnung der Physikalisch-Astronomischen Fakultät ist mir bekannt.

Ich versichere ehrenwörtlich, dass ich nach bestem Wissen die reine Wahrheit gesagt und nichts verschwiegen habe.

Jena, 26. November 2015

Albrecht Werner